



The Alliance of Laboratories in Europe for  
Education, Research and Technology

# **ALERT Doctoral School 2022**

## *Advanced Experimental Geomechanics*

Editors:

Edward Andò

Benjy Marks

Ryan Hurley

Joshua A. Dijkstra





---

## Preface

---

From 29th September to 1st October 2022, the ALERT Doctoral School 2022 will take place in Aussois and will be dedicated to “Advanced Experimental Geomechanics”. The School has been organized by Edward Andò (EPFL Center for imaging), Benjy Marks (The University of Sydney), Ryan Hurley (Johns Hopkins University) and Joshua A. Dijksman (Wageningen University). I sincerely thank all the contributors to this book for their effort!

Experimentation is the pillar of the geomechanics, it is the root for further developments of constitutive modelling and numerical computations. Since pioneers works of Terzaghi, Casagrande and many others, experimental geomechanics is continuously evolving to provide a deeper understanding of the geomaterial’s complexity. The last Doctoral School on this topics traces back to 2012 and it is thus the time organizing the school on this topic. In ten years, the techniques have of course evolved, but the objective of our network is above all to contribute to the education of the PhD students. It is worth mentioning that two of the School Editors were PhD students in 2012! I am therefore convinced that this school will be beneficial to the ALERT community.

The school will run over 3 days with the first day starting with the definition of advanced experimental geomechanics and introducing the methods in 2D. The second day will focus on specific features to extend these techniques to 3D exploration. The half-day will go towards 4D with deformation quantification.

As usual, the pdf file of the book can be downloaded for free from the website of ALERT Geomaterials (<http://alertgeomaterials.eu/publications/>) after the school. On behalf of the ALERT Board of Directors I wish all participants a successful ALERT Doctoral School 2022!

Frédéric Collin  
Director of ALERT Geomaterials  
University of Liege



## Contents

Foreword	
Andò, Marks, Hurley & Dijksman .....	1
Advanced Experimental Geomechanics	
Andò, Marks & Hurley .....	3
2D Image Analysis To Find Particles	
Marks .....	39
Photoelasticity: Stresses and Forces in 2D	
Hurley .....	65
Introduction to 3D Imaging for Experimental Geomechanics	
Andò .....	77
Refractive Index Matched Scanning	
Dijksmann .....	83
3D imaging of opaque materials	
Andò .....	113
3D Analysis	
Andò .....	131
Stress and Force Measurements in 3D	
Hurley .....	157



---

## Foreword

---

In 2012, the ALERT Doctoral School was organised by Gioacchino Viggiani, Stephen A. Hall and Enrique Romero on the topic of *Advanced experimental techniques in geomechanics*. Two of the Editors of the 2022 Doctoral School attended as PhD students in 2012, and it is no understatement to say that their interest, understanding, and passion for experimental geomechanics were significantly impacted by this formative experience. In 2022, we will revisit this topic, highlighting the advances made in the last ten years, the state of the art, and re-evaluate our evolving understanding of the practical use of experimental data.

In the Lecture Notes for the 2012 Doctoral School, it was stated that

*One of the main drawbacks of traditional experimental approaches is that they provide information relating to macro-scale, “averaged” responses and no details on internal structural evolution and deformation mechanisms, e.g., shear band development.*

The Doctoral School in 2012 presented several new, cutting-edge techniques for probing geomaterials at a variety of spatial and temporal scales, and in particular, focused on techniques that could recover spatially distributed measures of material properties. These techniques could observe both the heterogeneity of the material itself and the heterogeneity of any material response. In the intervening decade between that statement and now, our ability to acquire, process and interrogate such data has matured, and what was then difficult and laborious is now relatively routine, with well developed software and hardware solutions that can be purchased off the shelf or downloaded for free. This School will introduce students to the state of the art in these measurement techniques, their applications to geomechanics, and give hands-on experience with their implementation.

Edward Andò  
Benjy Marks  
Ryan Hurley  
Joshua A. Dijksman



---

# Advanced Experimental Geomechanics

**Edward Andò<sup>1</sup>, Benjy Marks<sup>2</sup> and Ryan Hurley<sup>3</sup>**

<sup>1</sup>*EPFL Center for Imaging, Switzerland*

<sup>2</sup>*The University of Sydney, Australia*

<sup>3</sup>*Johns Hopkins University, United States of America*

---

## 1 Introduction

Ten years ago, the ALERT doctoral school was dedicated to describing the growing trend of full-field measurements in experimental geomechanics [VHRM<sup>+</sup>12]. Already at that time, the use of contact-only measurements for displacements, strains, stresses, and forces at sample boundaries was considered “conventional”. Full-field measurements of kinematics using optical and x-ray methods were becoming increasingly common and promised to advance our understanding of the quintessentially heterogeneous mechanical behaviour of geomaterials including sands, clays, rocks (sandstones, limestones), and more. Intra-granular measurements of grain strains were also underway [HWP<sup>+</sup>11] and offered the opportunity to use individual grains in a granular material or rock as a stress or force sensor, as was already common in the metals community [OSP<sup>+</sup>10].

Ten years on, full-field *in-situ* optical and x-ray measurements have now become common for measuring the fully heterogeneous kinematics of geomaterials. The affordability of laboratory x-ray scanners has also aided in the adoption of full-field measurements. Tremendous advances have been made through the miniaturisation of complex sample environments (e.g., [BFCTF20]), mechanical loading equipment such as tri-axial compression devices [And13], and advanced image processing algorithms (e.g., [SAR<sup>+</sup>20a]). The tracking of tens of thousands of individual grains, or the application of strain measurements resolved to the grain-scale in sands and rocks, is now possible and increasingly commonplace [AHV<sup>+</sup>12b, SFBA22, BSM20].

New and exciting methods for going beyond kinematics have also emerged. Multi-modal measurements that harness the power of x-ray or neutron imaging and scattering are now being used to measure stresses and forces in geomaterials [HWP<sup>+</sup>11, HW15, HHAW16, CAKL14, SAR<sup>+</sup>20b], and to push our understanding of their mechanics to smaller, more fundamental length scales [HHWH20, BMV<sup>+</sup>22].

## 4 Advanced Experimental Geomechanics

The purpose of this doctoral school is to empower researchers and practitioners to make use of some of the latest technologies in experimental geomechanics. By the end of the school, students will be able to:

- Identify and use the appropriate advanced tools (imaging, RIMS, photo-elasticity, x-ray imaging/scattering, neutron imaging/scattering) available to access multiple scales of geomaterial response throughout stress space.
- Manipulate data acquired from advanced tools to develop datasets describing material response across length scales throughout stress space.

This chapter provides a high-level overview of some advanced techniques in experimental geomechanics. It can serve as a companion to the introductory lecture of the school. It is not exhaustive and is purposefully written to relate to granular materials, rather than geomaterials more broadly, due mostly to the specialities of the authors and partially to the very broad scope implied by “geomaterials”. Nevertheless, many of the tools and main ideas described in this chapter are applicable to a broad variety of geomaterials including sands, soils, clays, rocks as well as cementitious materials.

## 2 Major goal of advanced experimental geomechanics

Granular materials exist in a variety of forms, both natural and industrial. As bulk materials, they are transported, stored, packed and deformed for agriculture, pharmaceuticals, and geotechnical or civil engineering. Most engineering applications involve considering the bulk or field scale. Experiments and theoretical developments used to explain them, such as critical state soil mechanics [Woo90], therefore focus on the REV scale or longer length scales. At these length scales, stress and strain are the natural elements of a mathematical theory of deformation. Experiments used to develop and validate these theories traditionally employ measurements of stress and strain at sample boundaries without explicit consideration of the lower length scales. Excellent experimental work has been and continues to be performed at this length scale and our understanding of a granular material’s behavior for engineering-scale applications continues to evolve and improve. However, examining the scales smaller than the REV scale has become increasingly important as the effects of the particle scale are shown to play critical roles in engineering, powder processing, and dynamic processes. This theme, which is reflected throughout this chapter, was summarized by Terzaghi over one hundred years ago [Ter20]:

*... Coulomb... purposely ignored the fact that sand consists of individual grains. Coulomb’s idea proved very useful as a working hypothesis... but it developed into an obstacle against further progress as soon as its hypothetical character came to be forgotten by Coulomb’s successors. The way out of the difficulty lies in dropping the old fundamental principles and starting again from the elementary fact that sand consists of individual grains.*



A perfect and early example of grain-scale analysis is the Calvetti-Combe-Lanier paper of 1997 [CCL97] in which the authors used the so-called “ $1\gamma 2\epsilon$ ” strain-controlled loading frame to study the links between the applied loading and the particle-scale dynamics. In the introduction to their paper, they state:

*The full description of micro-mechanical behaviour may be divided into three points:*

1. *Description of the structure, that is to say, position of grains and contacts between them.*
2. *Description of the kinematics evolution: displacements, rotations, evolution of contacts.*
3. *Description of intergranular forces.*

*Experimentally, 2D materials (Schneebeli rods) are generally used for simplicity. The first two points need the ability to digitize the position of grains at each step of the macroscopic deformation. The third point is more difficult because measurement of forces needs sophisticated techniques such as photoelasticity.*

This extremely clear and simple statement of the ingredients for a micro-mechanical description serves perfectly as a guide for this entire chapter since a significant part of advanced experimental work on granular media in recent years has been at this scale. The first section will describe current experimental techniques that allow access to the grain scale, after which progress in the characterisation of structure, kinematics and intergranular forces will be discussed in a section each. A final section will summarize the uses of grain-scale information for a broad range of applications.

### 3 The experimental (granular mechanics) toolbox

Conventional mechanical testing involves placing a sensor on part of a sample, applying some load or deformation to a part or all of the sample, and observing the response of the sensor. Often this sensor is a strain gauge, a load cell or a pressure transducer. What the operator ‘sees’ are the local conditions surrounding this sensor. This method of experimental observation is reliable when the material of interest deforms homogeneously when the movement of the sensor to a different location on the sample does not change the outcome of the observation.

Unfortunately, for a granular material, this reliability is not typical. The study of these materials has been revolutionised over the past 50 years by the application and maturation of an alternative observational technique, that of ‘full-field’ imaging. The common thread through this family of experimental methods is that there is an attempt to measure the fields of interest ‘everywhere’ within a particular field of view. While this is not always practical, possible or necessary, the aim of full-field imaging is to acquire *fields* of information, rather than values at specific points. These fields may

include for example the displacement field, the stress field or the density field. Because a field is acquired, the result of a single observation is not a single data point, as would be attained from a conventional sensor, but rather an entire *image*, which is typically recovered as a regular grid of data in space. There are very many imaging *modalities*, each of which uses a portion of the electromagnetic spectrum to create an image of a particular quantity. We will discuss some of the more common imaging modalities for granular media, their historical development and the current state of the art.

The history of imaging technology is one of ever increasing spatial and temporal resolution with greater sensitivity. Originally, it was typically only possible to perform coarser-than-grain imaging, and we will therefore briefly introduce and discuss these developments, offering some historical perspective as well as current perspectives for larger sample sizes. With increasing technological development, grain-scale imaging has become possible and relatively routine. In 2022, modern ‘advanced’ experiments in granular mechanics now look similar to classical mechanical experiments, with the main distinction that they are strongly augmented with advanced measurements and often performed at shorter length scales. This section will therefore focus on detailing the different modern measurements that provide significantly more information about traditional experiments, in the context of the three points of granular micro-scale description quoted from [CCL97] in Sec. 1.

### 3.1 Photography and image analysis

The most common and natural form of “imaging” is photography, which captures the radiated visible light in a given field of view, thus recording a field. Historically the capturing of light has been chemical, generally requiring chemical development, but for the past two decades, digital cameras have been available, directly saving the measured luminosity as a numerical value in a discretised array of (generally square) pixels. For a colour photograph, each pixel contains three values, one each for the intensity of the red, green and blue light. If one were to convert this image to contain just a single scalar value at each pixel, *e.g.* the brightness, we would refer to the magnitude of that scalar as the *greylevel*.

The Calvetti-Combe-Lanier paper [CCL97] uses a remarkable experimental device, the “ $1\gamma 2\epsilon$ ” frame, for studying the mechanical behaviour of the so-called “Schneebeli” materials [Sch56, Gou93] — shapes extruded in one direction and stacked so that their deformation mechanisms are confined to the plane and are essentially two-dimensional. Commonly, the face of the particles is left free, so that technically speaking these are 3D materials being tested in-plane stress conditions. This allows photographs to be easily made of the face of the particles, and particles can be made large enough to be easily identified.

The Calvetti-Combe-Lanier paper [CCL97] uses photography, and both granular structure and kinematics can be extracted from photographs. Regarding a discrete granular structure, the *minimum requirements* from the photograph — interpreted as a field measurement of a surface — is that it is capable of *resolving* (*i.e.*, has high

enough spatial “resolution”) individual particles, and that there is sufficient *contrast* to distinguish pixels that make up particles from other background pixels. It is generally possible to identify circular particles in an image if its diameter spans about 6 pixels of the image. In the ideal case of sufficiently high contrast — signal-to-noise ratio of the *greylevel* of particles to the background of 10 or above — all the pixels corresponding to particles can be identified with a simple thresholding operation on the value in the image. The result of applying a threshold is a *binary image* where pixels are marked as belonging, or not belonging, to the particle “phase”. Such an image can easily be used for the computation of porosity, given some reasonably large averaging volume, which is reduced to a pixel-counting exercise.

To fully exploit a field measurement in which particles can be seen, they need to be individually identified in the picture. This involves subdividing the pixels flagged as being inside the particles into individual particles. A common way to represent individual particles is to “label” pixels so that the group of pixels that represent a single particle all have the same unique (typically integer) value. More advanced strategies that represent particles with quantities other than with only an integer label, such as level sets [VAVA14], are also popular. Starting from any such particular definition of particles, their morphological properties in the category of granular structure can be obtained by performing digital measurements on virtual shapes; centres, equivalent radii, caliper lengths (“feret diameters”) are all popular morphological properties.

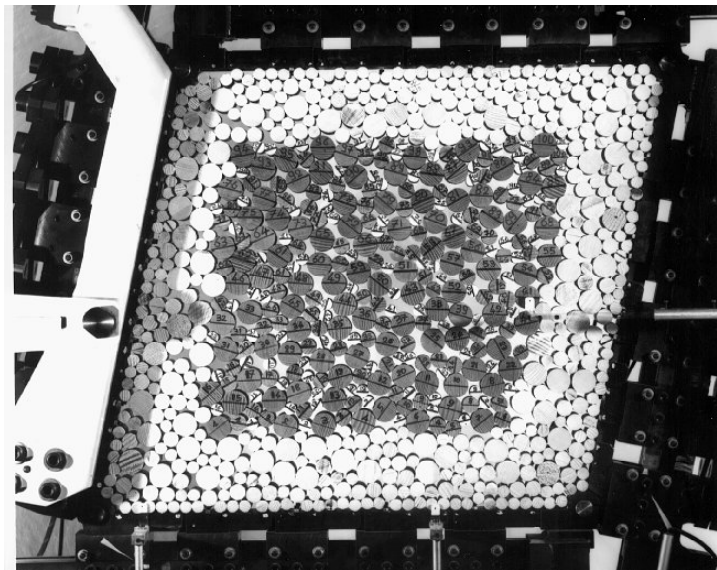


Figure 1: Raw photograph cropped from [CCL97], with clearly identifiable 2D particles in the form of Schneeblis rods

### 3.2 Repeated photographs

A time series of photographs acquired during some process that causes particles to move is an immediate invitation to measure particle kinematics. Here there are three convenient methodologies that allow kinematics to be measured:

1. Particle-tracking approaches in which individual particles are tracked as discrete objects using the invariance of their shape to recognise them. This is closely related to PTV (“particle tracking velocimetry”).
2. Digital Image Correlation (DIC) based approaches, in which texture matching is used to align greylevels in a region of one image with the closest matching greylevels in a subsequent image. By finding the best match for a large number of patches, a dense field of displacement vectors can be found from which a strain field can be constructed.
3. When individual particles can be identified in an image, image correlation can also be used to attempt to track the particles between images. In this case, only one labelled image, typically from a reference state, is needed as a “mask” to select the greylevels in the image to match in the subsequent time step. This is more closely related to PIV (“particle image velocimetry”) and is also known as PIT (“particle image tracking”) or DDIC (“Discrete Digital Image Correlation”). Experience shows that the edge of a particle is an excellent source of texture for this sort of matching. Therefore, if the mask is slightly larger than the particle this will tend to work in the cases where particle tracking works. The added advantage is that internal texture in the particles can be exploited to make measurements more accurate.

In all three above methodologies, displacement accuracy below  $\frac{1}{10}$  of a pixel can be obtained. In the history of advanced experimental mechanics, DIC, and its analog counterparts, were the sort of technique that was used to measure strain fields in plane-strain (or “biaxial”) load apparatuses with transparent boundaries, applying texture or a grid onto the membranes holding sand samples. There are well-known examples in the literature of such devices, such as the plane-strain device created in Grenoble in the 1980s by Jacques Desrues [DV04], as well as those created by Ioannis Vardoulakis [HV91]. In these devices, prismatic membranes holding the prepared specimens were painted in order to be able to track the displacement of boundary points. Figure 2 reveals the richness of information that such experiments can provide, showing incremental fields computed by comparing pairs of images: a vectorial representation of the displacement field, the material rotation field, as well as the first and second invariant of strain. Such fields are important in the framework of critical state soil mechanics, which is formulated in terms of rates of strain and stress invariants. Later works used digital videos, and manual tracking of a grid painted on the membrane [AS00]. The work of Amy Rechenmacher [Rec06] is a good example of recent work using this technique without membranes and using the natural sand texture for tracking.

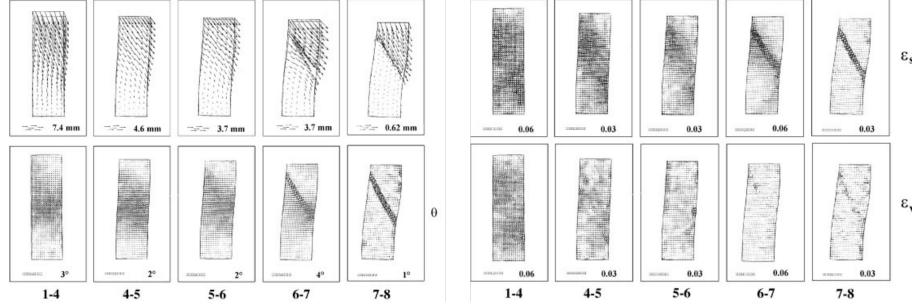


Figure 2: Incremental kinematic quantities computed between photographs acquired during a plane-strain test on very loose sand. Top left series: Displacement field, bottom left: material rotation, top right: second invariant of the strain tensor (deviatoric strain) bottom right: first invariant of the strain tensor (volumetric strain), adapted from [DV04]

These works have enabled the precise measurement of evolving strain fields accompanying strain localisation, allowing the quantification of the effects of particle size, packing fraction, as well as granulometry on shear band patterns and shapes. However, point-tracking using photographs is clearly limited to measuring surface displacements, which may not be representative of strain fields within the material. Although individual particles may be visible on detailed photographs and indeed even tracked, there is an irredeemable disconnection between the 2D images acquired and the 3D nature of the particles that may be out of view.

### 3.3 Photo-elastic techniques

Photo-elasticity is an imaging technique for measuring and visualizing stress within materials based on changes to their refractive characteristics when under strain [RKNS11, Fro41]. The photo-elastic method typically involves placing a material — such as a cylinder or a disc for granular mechanics studies — between a left and a right circular polarizer prior to exposing it to strain as shown in Fig. 3(a). Upon straining, an observer or camera viewing the material through both polarizers while it is illuminated by a far-field light source will see fringe patterns develop whose intensities are determined by the local principal stress differences. While both RGB and monochromatic light can be used in photo-elasticity experiments, the use of monochromatic light leads to the simpler case of isochromatic fringes with intensity

$$I(x, y) = I_0 \sin^2 \frac{\pi(\sigma_1 - \sigma_2)}{F_\sigma}, \quad (1)$$

where  $I_0$  is the incident light intensity,  $\sigma_1$  and  $\sigma_2$  are in-plane principal stresses and  $F_\sigma$  is the stress-optic coefficient which is a bulk material property. Figure 3 shows three fringes developed within a diametrically-compressed disc. The numbers 1, 2,

and 3 correspond to fringes in which  $\pi(\sigma_1 - \sigma_2)/F_\sigma$  equals  $\pi/2, 5\pi/2$ , and  $9\pi/2$ , respectively [DKP17].

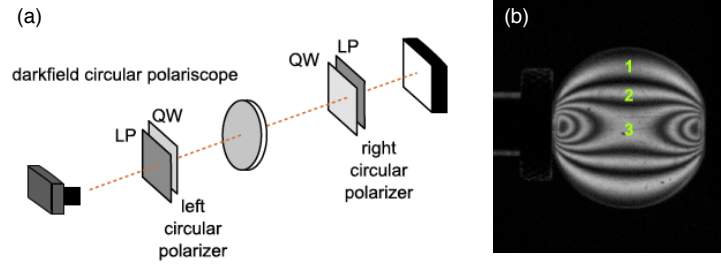


Figure 3: (a) Example of a darkfield circular polariscope setup used in photoelasticity experiments. (b) A typical birefringence pattern observed in a diametrically-compressed disc, showing three fringes corresponding to specific principal stress ratios, as described in the text. Figures are adopted from [DKP17] with permission.

### 3.4 Radiographic imaging

The first Nobel prize in Physics was awarded to Röntgen for the discovery of x-rays, whose remarkable ability to penetrate matter but also to be detected by scintillation allowed Röntgen to produce a radiograph of his wife's hand, shown in Figure 4. The interaction of x-rays with matter can result in quite complex physics; however, at first order, the intensity of a single-energy (monochromatic) x-ray beam travelling through matter exponentially decays with distance, as captured in the well-known Beer-Lambert law. The x-ray attenuation coefficient representing this reduction in intensity is approximately proportional to the material density and atomic number. This can be seen in Figure 4 of the hand, where the calcium-heavy bones and the metallic ring attenuate more than the surrounding flesh.



Figure 4: A print of one of the first x-ray radiographs by Wilhelm Röntgen (1845–1923) of the left hand of his wife.

Figure 4 shows an x-ray *radiograph*, an image obtained by placing an object to be measured — the hand — between an x-ray source and a detector. In this case, the x-ray detector is a photographic plate in contact with a scintillator that converts x-ray photons into visible light photons. What is measured at every point in the photographic plate is the intensity of the *transmitted* beam. This is the attenuation of the object being imaged, *integrated* over the path between the x-ray source and the x-ray detector. This basic x-ray imaging technology is in essence the same setup today: source-object-detector.

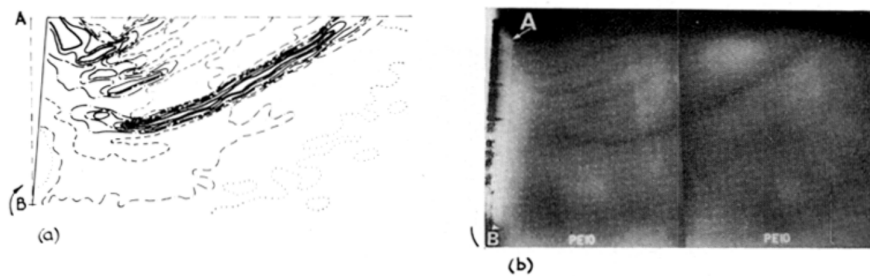


Figure 5: Figure from [Ros70]. Left) contour plot of  $\gamma$  as obtained by tracking displacement of lead shot seeded in the experiment. Right) Radiograph showing corresponding zones of higher transmission (darker zones)

Since what is measured is an integration along a beam path, an object that attenuates significantly more than its environment will appear clearly in a radiograph; however, determining the object's position *along* an x-ray beam path is more challenging. This property of *contrast* was leveraged early in the history of soil mechanics — see



[Ros63] for an early example. The same author’s Rankine lecture [Ros70] exploits the very high attenuation coefficient of lead spheres to serve as *tracers* expected to follow material deformations. Figure 5 presents two fields measured during the rotation of a rigid wall (A-B) around B into dense sand. The left image presents the spatial distribution of  $\gamma$ , the maximum shear strain, computed from a displacement field obtained by tracking the lead shot placed in the “central plane of shear” between subsequent radiographs. The right image is the raw radiograph in which lead shot is barely visible as white dots and with black zones signifying *more* transmission through the whole experiment. There is an excellent correspondence between the deviatoric strain field as computed by the lead shot, and the radiograph whose darker zones indicate less matter along the beam, a consequence of material dilation. This correspondence is all the more important because it confirms — in this case — that the strains measured in the plane of the lead shot seem to represent the strains throughout the depth, since they correspond to the left image which is integrated through the depth of the experiment. A key point, and a difference from previous work, is that this use of x-ray imaging allows strains *within* the experiment to be revealed, freeing the experimentalist from boundary effects that are inherent with the observation of the surface of the material through a transparent wall.

As with photography, digital x-ray detectors are now routinely and almost exclusively used, meaning that digital images can be acquired, even at high frequency. It is key to remember that the result of this imaging modality is a 2D image in which each pixel represents the line-integration of a 3D field of attenuation.

### 3.5 Radiography of dynamic processes

Granular media exhibit a broad range of behaviors over widely varying time scales. In the example above, the motion of the slowly moving wall caused quasi-static deformation inside the granular medium. Alternatively, when impacted by a high speed projectile, a body of particles can move significantly in nanoseconds [GCZ<sup>+</sup>21]. This type of *extrinsic* loading typically causes the grains to move at or near the applied velocity, or alternatively to fail in some way. The granular system, however, has time scales of its own, and when applied loads or displacements are slower than these time scales, the medium can behave intermittently [EG18]; periods of slow or no motion may be followed by the rapid onset of motion that evolves at a rate determined by the material itself. For example, when loaded quasi-statically, particles can crack, with the crack tip moving at speeds often too fast for imaging and causing rapid particle rearrangements. When particles are placed in a slowly rotating drum, such as a clothes dryer at the end of its cycle, intermittent avalanches may occur at the free surface, with grains far from the moving surface in time or space rotating much more slowly with the drum.



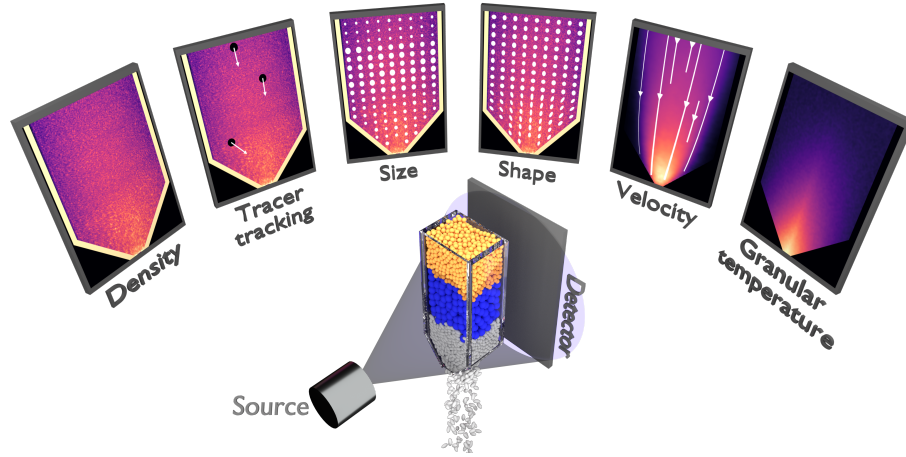


Figure 6: Schematic representation of various measurements that can be made using radiography of granular materials that are non-stationary. *Bottom:* Experimental configuration of three materials being sequentially discharged out of a hopper while exposed to x-ray emission from a source that is recorded on a detector panel. *Top, left to right:* The raw radiograph, which can be used to infer material density. Tracking of dense and/or large tracer particles. Size measurement for polydisperse materials. Shape measurement for elongated materials. Velocity measurement for moving materials. Granular temperature measurement for jiggling materials.

To measure the dynamics of these systems with imaging, one must resolve this motion at appropriate time scales and length scales. To record the dynamics, we therefore have to satisfy the following criteria for our object of interest:

1. We need sufficient spatial resolution to resolve the features of interest.
2. We need sufficient temporal resolution to resolve the motion of the features of interest.
3. We need a sufficient number of sequential images to identify the behavior of interest.
4. We need to consider the errors that arise due to imperfections or uncertainties in our experimental setup and algorithms.

**Spatial resolution** To be able to *resolve* a feature of interest, we recommend imaging at a scale where there is at least one pixel per feature. This would be sufficient if there were no other features nearby and no sources of noise. In general, this is not nearly enough pixels. A good rule of thumb is to have at least 6 pixels across a given feature. This will enable reasonable detection of the feature, while still giving the ability to image quite a few features simultaneously with a finite number of pixels.

**Frame rates** The number of frames recorded per second is referred to as the *frame rate* and is measured in Hz. Typical TV shows arrive on your TV screen at 30 Hz. A computer game, which requires rapid feedback between the display and the user, is rendered at 120 Hz on the latest hardware. These frame rates have been increasing over time as the recording hardware, display equipment and storage media allow. At the time of writing, it is reasonable to expect that in your pocket or hand right now there is most likely a phone capable of recording high resolution videos at more than 240 Hz. X-ray flat panel detectors, however, feature frame rates around 10 Hz to 30 Hz. Higher frame rates can be achieved with scintillator panels and optical cameras, but with reduced brightness. For a summary of the current approximate length and temporal scales available for imaging, see Figure 7.

It is important to note that it is not necessary to record all of the x-rays that arrive at the detector panel between frames. The amount of time that you expose the detector panel to the beam during each frame is known as the *exposure time* and it cannot be larger than the period between frames.

An important consideration when picking an exposure time is ensuring that enough x-rays will hit the detector panel during this period for a reasonable image to be resolved. If the source is not bright enough (*i.e.*, the flux of photons is too low), an image will appear to be *speckled* with significantly varying greylevel values in regions even where the material is not varying. Such a problem can be solved by increasing the brightness of the x-ray source or the efficiency of the detector panel.

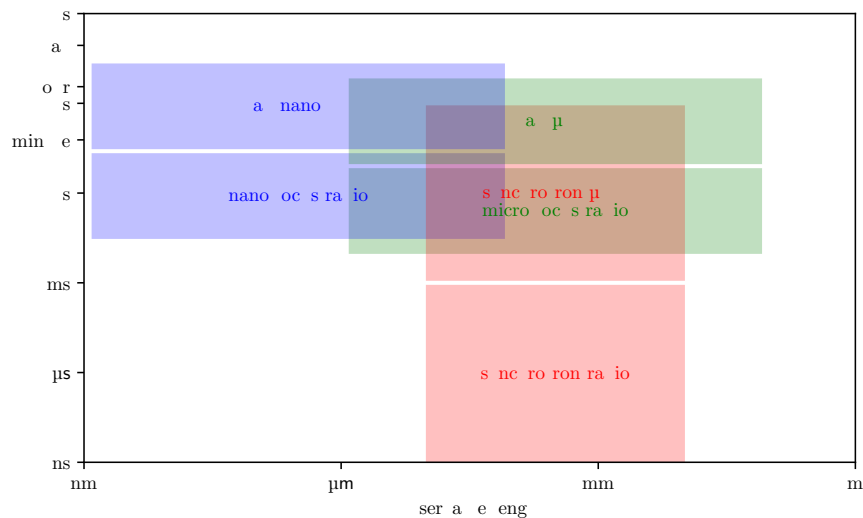


Figure 7: Indicative time and length scales that can be captured with laboratory and synchrotron x-ray radiation sources. This information is extremely general and there are many caveats which alter this behaviour. Additionally, over time these indicative windows move and enlarge due to advances in x-ray source and detector technology.

**Bandwidth** You will notice that as the frame rate increases, your phone or camera will not allow you to record at the highest spatial resolutions. This is because of the technical limitation of bandwidth. There is only so much information that can be passed through a communications system in a finite time. Therefore, for any system, there is inherently a trade off between spatial and temporal resolution.

Given enough brightness and bandwidth, it is possible to record frames at exceptionally high rates [GCZ<sup>+</sup>21], capturing incredibly fast dynamics. However, because of the range of temporal scales observed in granular media, the data storage requirements can be prohibitive to record at such a fast rate for such a long duration. In practice, it is typical that by recording at a frame rate that is reasonable to study the main mechanism of interest, we do not capture either the mechanisms happening much faster or slower than our frame rate. Whether or not this is a problem is a matter of perspective.

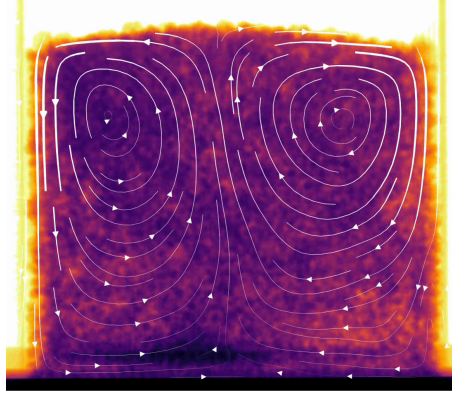


Figure 8: Vibration induced flow in a granular material. The system is vibrated vertically which induces flow with two convection cells. Particles flow downwards at the system boundaries, and upwards at the centre of the box. The white lines represent streamlines of the velocity field as measured using digital image correlation (DIC) on the radiographs. Thicker lines represent higher speeds.

**Uncertainty** Inherently, the measurement of particle locations with finite resolution at finite times results in measurement uncertainty. Due to the finite times, we necessarily miss some of the dynamics. Due to the finite spatial resolution, we never recover the precise locations of bodies, and the velocities measured with this imprecision are therefore also imprecise to a degree. Depending on the quantity of interest, such uncertainties may introduce systematic biases into measurements derived from these observations, and these should be accounted for explicitly [MGB<sup>+</sup>21].

### 3.6 High-speed radiography

High-speed x-ray imaging of dynamic events has benefited from recent technological advances at synchrotron facilities and in laboratory-based x-ray systems. Existing third generation synchrotron facilities including the Advanced Photon Source (APS) and the European Synchrotron Radiation Facility (ESRF) have the x-ray brilliance, x-ray characteristics, fast detectors or scintillators, and dynamic drivers needed for time-resolved imaging of dynamic compaction events in granular materials. Laboratory x-ray sources and detectors have also matured to the extent that 2D imaging may be performed at repetition rates of tens to hundreds per second. It is often desirable to use highly-coherent x-rays in time-resolved imaging experiments on granular media because such configurations enhance phase contrast, which highlight grain boundaries and internal fractures that emerge during rapid compaction [JMI<sup>+</sup>19]. Coherent x-rays are a feature of many synchrotron beamlines used for high-speed imaging studies; laboratory x-ray sources usually produce less coherent x-rays. It is also necessary to use fast detectors or scintillators with short decay times coupled with high-speed cameras for imaging dynamic compaction or penetration events [JMI<sup>+</sup>19]. Scintillators

and high-speed cameras present at synchrotron facilities can enable this; laboratory studies usually employ slower repetition rates similar to medical imaging detectors [BGME18], or use detector plates and flash x-ray sources [PBTJ19]. Finally, a device that drives a dynamic event is also needed. These have included split Hopkinson bar devices [HCD<sup>+</sup>13, LRF<sup>+</sup>18], gas guns [JRI<sup>+</sup>14, RCD<sup>+</sup>17], and exploding foil initiators [WCH<sup>+</sup>16].

### 3.7 Tomography

The next technological step beyond x-ray radiography is x-ray *tomography*, whose creation also yielded a Nobel Prize in Physiology and Medicine in 1979 to Cormack and Hounsfield. Where radiography presents an x-ray attenuation value integrated over the path between source and detector, which can be measured directly, tomography aims to reconstruct the underlying attenuation *field* from a number of different radiographs [Cor73]. Concurrently with the necessary mathematical developments by Cormack in the 1960s and 1970s, Hounsfield invented the first x-ray computed tomography (CT) machine enabling rotation of an x-ray source around a sample, or patient, for medical purposes [Hou73]. The original x-ray tomography machine was large and expensive but provided one of the first methods for reconstructing the internal structure of a material in 3D. Within a little over a decade, researchers were placing geologic materials such as sandstones in medical CT scanners [CKB84] to image internal structure and fluid flow. Specialized loading frames were developed in the 1980s and 1990s for *in-situ* studies of rocks and geologic materials under conditions similar to those experienced in nature while inside medical CT scanners.

Desrues and colleagues pioneered the use of x-ray tomography for studying the internal structure of sands in the 1990s [DCMM96]. These early studies employed technology optimized for medical applications and were incapable of focusing on particle-scale features of granular materials. As a result, early studies examined void ratios and the formation of porosity on length scales larger than individual particles, such as in shear bands [DCMM96, ASC<sup>+</sup>00], revealing the rich non-symmetric spatial patterns of void formation that accompany strain localization in sands without actually resolving individual grains. Research in the late 1990s and early 2000s, primarily in the United States [FMW95], France [VLB<sup>+</sup>04] and Japan [TLHY02, OTT04] continuously pushed pixel sizes of x-ray tomography images in geomaterials down from 200  $\mu\text{m}$  toward 10  $\mu\text{m}$  and introduced the term “microtomography” to the field of geomechanics. An important parallel effort underway at this time was the development of specialized loading frames that enabled standard experimental geometries, such as traditional triaxial tests, to be performed simultaneously with *in-situ* x-ray tomography measurements (e.g., [VLB<sup>+</sup>04]).

Beginning in the late 2000s, grain-scale microtomography, *i.e.*, microfocus tomographic imaging with pixel sizes of 5 – 15 microns/pixel became feasible because of advances at synchrotron radiation facilities such as the European Synchrotron Radiation Facility (ESRF), the Advanced Photon Source (APS), and SPring-8. Almost in parallel, the advent of microfocus x-ray sources also brought x-ray microtomography

into lab-based scanners, albeit with longer scanning times. For researchers studying sand with particle sizes of hundreds of microns, the micro-scale x-ray tomography volumes produced by these scanners allow individual particles to be identified as can be seen in the inset of Figure 9. With both lab and synchrotron x-ray sources, there is generally a direct trade-off between the field of view and spatial resolution, meaning that small zones are generally scanned at this small pixel size. Also at this small scale, Figure 9 clearly shows how the reconstructed images from x-ray tomography show a clear distinction between air or water filled pores, which appear darker in the image, and silica particles, which appear lighter in the image. This strong contrast between the phases that are of interest to separate and identify for researchers working on natural sands is extremely convenient: the air/water/silica granular system provides excellent contrast and is ideal for tomography studies.

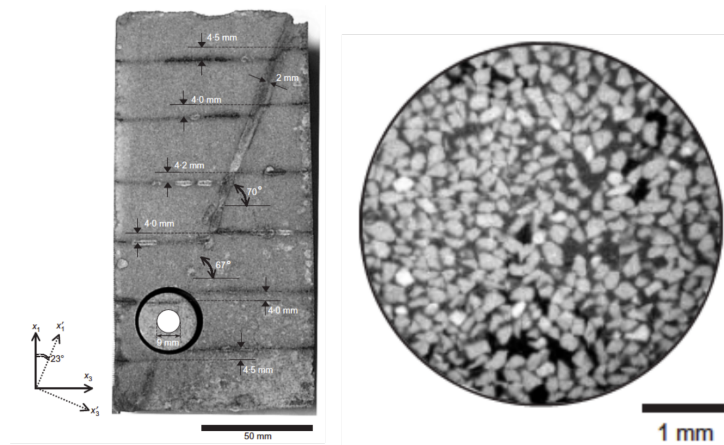


Figure 9: Microfocus x-ray tomography image (9 microns/pixel) from [OTT04] showing a shear band (left) and a focused image region (right) in which individual grains and voids can be visualized. Reproduced from [OTT04] with permission.

### 3.8 RIMS

A direct approach to full-field grain-scale imaging that is simpler than x-ray tomography and amenable to simpler laboratory operation is refractive index-matched scanning (RIMS) [DRL<sup>+</sup>12, DBB17]. RIMS involves illuminating a single planar cross-section of a 3D granular medium with a laser sheet. The granular medium must be immersed in an index-matched fluid to avoid the refraction of light at particle-void boundaries. This can usually be accomplished with a range of material and fluid types [DRL<sup>+</sup>12]. The illuminated 2D planar cross-sections are recorded with a standard charged coupled device (CCD) camera as the laser sheet is moved incrementally through the entire 3D medium. A 3D reconstruction can be produced by stacking the resulting 2D images. In contrast to x-ray tomography, RIMS does not require a ra-

diation source or back-projection algorithms. RIMS may also be used to reconstruct full-field images with repetition rates as fast as 1 Hz [DRL<sup>+</sup>12].

### 3.9 Multi-modal measurements: x-rays tomography and scattering

Multi-modal measurements employ more than one simultaneous or directly sequential measurement modality to study materials. Examples of multi-modal measurement currently used in granular mechanics are; x-ray CT and x-ray diffraction; x-ray CT and neutron radiography or CT. The goal of multi-modal measurements is to exploit the complementary features of each method to yield deeper insights into material behavior. For instance, x-ray CT can readily be employed to reconstruct material density but x-ray diffraction can more easily be used to determine a material's crystal structure or crystalline strain. Similarly, x-ray CT is most sensitive to the atomic number of a material while neutron CT is sensitive to hydrogen content (*e.g.* fluids and water in particular).

3D x-ray diffraction (3DXRD) has enabled quantifying the lattice strains and stresses in individual grains comprising a polycrystalline metallic or geologic material [Pou04, OSP<sup>+</sup>10]. 3DXRD makes use of Bragg's law,

$$n\lambda = 2d \sin \theta, \quad (2)$$

where  $n$  is the diffraction order,  $\lambda$  is the wavelength,  $d$  is the distance between diffracting planes of atoms, and  $\theta$  is the glancing or diffraction angle. Figure 10(a) illustrates the geometry associated with Bragg's law. Figure 10(b) illustrates a typical geometry currently used for 3DXRD studies in which a diffraction detector is located far from a sample that is housed within a mechanical loading device on a rotation stage. 3DXRD requires 180° and ideally 360° rotation of a sample with diffraction detector images obtained every 0.1° increment of rotation so that Bragg spots from many crystalline planes are collected. The “spotty” diffraction detector image shown in Fig. 10(b) illustrates the Bragg spots generated from a single angle.

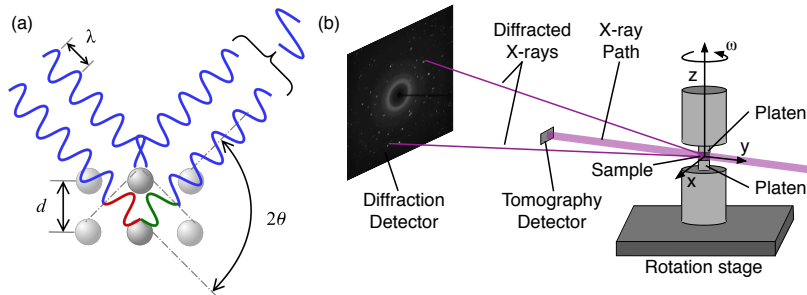


Figure 10: (a) Schematic of Bragg's law. (b) General geometry of an experiment combining x-ray CT and 3DXRD.

Multi-modal measurements combining x-ray CT and x-ray or neutron scattering were first made in the early 2010s [HWP<sup>+</sup>11, ACKL13]. Initially, multi-modal measurements were motivated by an interest in quantifying particle stresses and inter-particle forces in real sands [HWP<sup>+</sup>11]. Early measurements were made in simple uniaxial strain geometries with tens or fewer particles [HWP<sup>+</sup>11, ACKL13, HW15] and focused on using coherent x-ray scattering to quantify strain tensors within individual grains.

## 4 Granular Structure

The first ingredient of the micro-mechanical behavior of granular materials described in Sec. 1 and [CCL97] is structure. In this section, we discuss some of the latest applications of the tools described in Sec. 3 to study granular structure.

The advent of 3D imaging techniques with sufficient spatial resolution to allow individual grains to be distinguished precipitated a new era of quantitative description of granular materials at their natural scale. The most disruptive technology in this field has been x-ray *micro* CT, although a number of other methods can also produce 3D data volumes at sufficient resolution to be able to distinguish individual particles.

Oda's experiments were some of the first to image particle-scale microstructures within larger deformation structures (shear bands) developed during the deformation of soil samples [OTT04]. These studies established the possibility that large void formation within shear bands in sand develops because of the formation and lateral buckling of columns of sand particles, motivating further studies and micromechanical models. Subsequent work in which sand samples were cored-drilled from large epoxied samples [HA10] was able to confirm some features of the granular structure of mature shear bands. Grain-scale images from this work (*e.g.* Fig. 9) combined with different quantitative image-processing algorithms enable particle identification and per-particle microstructural analysis; see also, for example, the work of [ASS05].

Given sufficient contrast in the 3D images acquired from CT, images can be *thresholded* to yield a binary image of voxels belonging to particles and all others, rendering the computation of porosity a simple voxel-counting exercise in a given REV. Advanced 3D image analysis then enables the quasi-automatic detection and identification of particles — in particular efficient implementations of the (markers based-) watershed algorithm — allowing high quality and automatic quantification of these granular systems.

### 4.1 Inter-particle contacts

Consider again the three requirements for a full description of micro-mechanical behavior described in [CCL97]: structure, kinematics, and forces. Figure 11 illustrates a measurement of particle positions as well as their kinematics, covering the first two requirements. However, the tracking of inter-particle contacts in time is more complex and challenging to do in an unbiased way. In the case of spheres, a deconvolution



approach gives excellent results [ASS06]. Nevertheless, [WAHV17] highlighted that trusting the standard image analysis approach for detecting contacts between particles on the binarised image may be fraught, requiring instead careful treatment of contact detection as well as the measurement of orientation between particles. The authors of [WAHV17] proposed such techniques, which have now become standard [SAR<sup>+</sup>20a]. This implies that structure, the first requirement for a full-description of micro-mechanical behavior in [CCL97], can be fully measured in a 3D assembly.

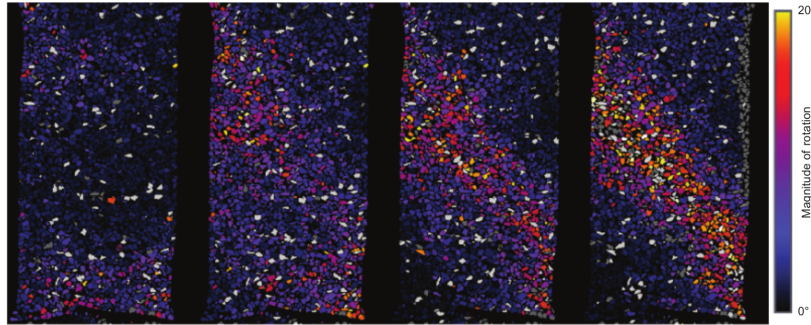


Figure 11: Incremental 3D grain rotation angles during triaxial compression from [HBD<sup>+</sup>10]. This data and analysis contains the ingredients “structure” and “kinematics” ingredients of a full micro-mechanical description.

Tracking the kinematics and lifetime of contacts, which are routinely obtained from discrete element method (DEM) simulations, is another step in complexity requiring not only an appropriate identification of contacts but essentially faultless particle tracking over numerous increments of material motion. A first hint of this possibility on a very simplified granular system has recently appeared [WPAV22].

## 5 Granular Kinematics

The second ingredient of the micro-mechanical behavior of granular materials described in Sec. 1 is kinematics. In this section, we discuss the tools used to study full-field granular kinematics and highlight some of the latest results.

### 5.1 Quasi-static granular kinematics

The development of low x-ray attenuation, miniature loading frames for classical experimental testing geometries, such as triaxial compression, for specimens measuring only several millimetres in dimension, enables loading to be applied to specimens inside the scanner. Matushima *et al.*, [MUNT06] offers a very early example of a miniature triaxial test with *in-operando* x-ray microtomography, vertical slices through the

acquired 3D volumes are reproduced in Figure 12. Particles were manually tracked, allowing a strain field to be computed in a similar way to the radiographic lead-tracking from the 1970s [Ros70].

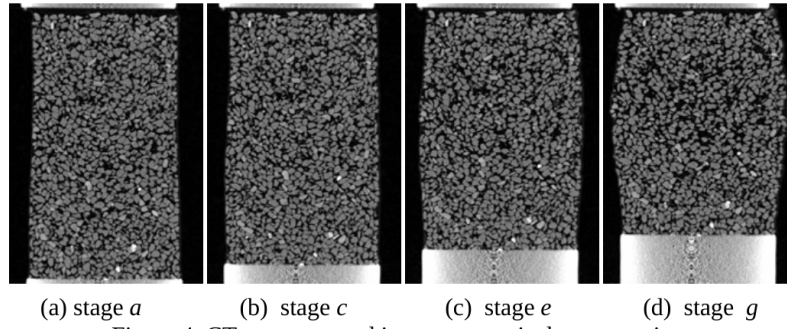


Figure 4. CT reconstructed images: a vertical cross section

Figure 12: A series of vertical slices acquired during a triaxial test performed with microtomography on Spring-8 from [MUNT06]

Experimental studies with more automated grain kinematics calculations were conducted by groups in France beginning in the late 2000s [HLV<sup>+</sup>09, HBD<sup>+</sup>10]. These studies provided profound insight into the mechanics of individual particle rearrangements in sands within and outside of shear bands, as illustrated in Figure 11, with the incremental 3D rotation of tens of thousands of particles concentrating into a shear band in a sample of 10 mm diameter! This impressive result heralded a new era of both experiments and micromechanical modeling focusing on such microscopic deformation mechanisms. On the experimental side, follow-up experiments explored varying particle shape [AHV<sup>+</sup>12b, And13, AHV<sup>+</sup>12a, HA10] and partial saturation [RAS<sup>+</sup>12, CKLF08, KRA<sup>+</sup>18, KPH12, HOK<sup>+</sup>11]. In general, these studies present a quantitative analysis of local void ratios, degrees of saturation, and grain-scale quantities such as particle kinematics [HBD<sup>+</sup>10, VAVA14].

## 5.2 Kinematics of particle breakage

Another key mechanism studied after the advent of grain-kinematics studies is grain breakage, a behaviour typical of granular systems experiencing high mean stress. Experiments examining grain breakage require strong confining cells, as demonstrated in an early example [CDDF88]. Unlike low-stress experiments in which the number and size of particles are not expected to evolve during the experiment, during tests at high mean pressure particles are expected to break and thus become more numerous and smaller. Such an evolution of particle number and size justifies the use of different sample sizes, from single- or few-particle assemblies [ZWC<sup>+</sup>15, CA12], to sample sizes resembling the original experiments [CA14, AAGK<sup>+</sup>15, KAP<sup>+</sup>18, KAP<sup>+</sup>19].

Remarkably, techniques have emerged to track particle fragments after particle breakage occurs [SSCB21], meaning that a very complete kinematic description is also possible, despite the complexity of such kinematics.

### 5.3 Beyond quasi-statics

Experimentally, theoretically and computationally, much of geomechanics research has been in the ‘quasi-static’ regime described above, where it is believed that rate effects do not play a significant role. However, there are many applications in which the rate of loading or more accurately rate of deformation of the material is strongly rate dependent. Examples of these problems are snow avalanches [Sal93], debris flows [Ive97] and liquefaction [DH17]. Studying the rate dependence of these materials implies that we need to be measuring these effects dynamically. A large number of studies have approached this problem using conventional optical imagery through transparent sidewalls [SL88], via refractive index matched grains and fluids [ACDB11, IBO15, YXZ<sup>+</sup>19, ZGZ<sup>+</sup>20], with MRI [Sta17] or x-ray radiography [GME17, DGB<sup>+</sup>20].

Alternatively, it is possible to track a small number of individual particles in steady-state flows (i.e. where the field of interest is not changing over time) and use these ‘tracer’ particles to build a map of the field over time, as has been done with Positron Emission Particle Tracking (PEPT) ([BCLvH18]) and x-ray radiography [MGB<sup>+</sup>21].

### 5.4 High-speed kinematics in 2D and 3D

At higher rates again lies ‘high-speed’ or ‘dynamic’ experiments, which image at kilo- or mega- Hertz. Prior high-speed 2D x-ray imaging studies in granular materials have examined the fragmentation of individual particles or small particle arrangements [JMI<sup>+</sup>19, PCH<sup>+</sup>14, PGH<sup>+</sup>17], through-thickness porosity reduction [CHP<sup>+</sup>19], and heterogeneous compaction fronts [CHP<sup>+</sup>19, RCD<sup>+</sup>17]. Most of these studies have been performed in the past ten years. Although these studies have provided insight into dynamic deformation mechanisms and important data for validating numerical models [JMI<sup>+</sup>19], flow and dynamic compaction processes in granular materials are 3D and their characterization, therefore, requires 3D techniques.

Recent combinations of novel algorithms with 2D x-ray imaging have enabled full-field reconstruction of 3D granular dynamics. Inspired by “discrete digital projections correlation” [KBB<sup>+</sup>17], experiments combining x-ray phase contrast imaging (XPCI) and novel algorithms have recently enabled reconstructing 3D particle dynamics with 153 ns frame spacing during the impact of granular materials at 1 km/s [GCZ<sup>+</sup>21].

Full-field reconstruction of 3D dynamics from 2D x-ray images enables one to quantify very rapid processes, such as pore collapse and fragmentation, that dictate stresses, temperatures, and resulting properties in powdered materials in planetary impact, industrial processing, and defense applications [Nes13, GCZ<sup>+</sup>21]. Full-field reconstruction of 3D dynamics of slower processes may help reveal the local particle rearrange-

ments and pore dynamics featured in theories of granular flow, including those relevant to non-local fluidity theory, elasto-plastic theories, and shear transformation zone theories [FL98, KK12, BCA09, HZ22].

## 6 Inter-particle forces

The third ingredient of the micro-mechanical behavior of granular materials described in Sec. 1 is forces. In this section, we discuss the application of tools used to study forces.

Photo-elasticity methods provided some of the first full-field measurements of inter-particle forces in compressed and sheared disk packings (albeit in 2D), revealing the anisotropy and heterogeneity of force chains [MB05]. The pioneering work of Dantu, De Jong, Drescher, and colleagues in the late 1950s through the early 1970s introduced the use of 2D photo-elastic discs and photo-elastic imaging to the granular mechanics community [Dan57, DDJ72]. Although performed in 2D, their experiments were the first to directly quantify inter-particle forces, to identify particle clusters bearing significant load and referred to as “force chains”, and to support the possibility of stress-strain non-coaxiality in granular materials using independent particle-scale measurements of stress and strain fields (e.g., Fig. 13(a)) [DDJ72]. Following these developments, Oda, Nemat-Nasser, and others used photo-elastic techniques extensively to study the mechanics of granular media in the 1970s and 1980s. Among the important concepts put forward by these researchers and their colleagues using photo-elasticity experiments were: the concept of inter-particle fabric (as captured by “fabric ellipsoids”) as a second-order measure of granular structure (with porosity as a first-order measure) [OK74, ONNK85]; the idea that the relative contributions of inter-particle frictional sliding and rolling during deformation of granular materials differs depending on inter-particle friction [OKNN82, OKNN83]; and the idea that stress-induced anisotropy, or fabric, depends on contact normals, particle shape, and void shapes [ONNK85]. Furthermore, the experimental data generated by these researchers using photo-elasticity experiments became important for other discussions and developments related to particle-scale behavior, dilatancy, and stress-strain co-axiality in geomechanics throughout the 1970s and 1980s (e.g., see [OKNN82, OKNN80, NNT82] and others by these authors).

In parallel to the developments in granular mechanics discussed in the previous paragraph, researchers in the 1980s began employing photo-elastic discs in dynamic loading experiments on granular materials (e.g., [RS82]). The ensuing decade saw important advances in understanding wave propagation through granular media, including in identifying contact density and orientation as primary constraints on wave velocities and directional stability of waves [RS82, SD87, SZS88, SSM90] (e.g., Fig. 13(b)). This body of research motivated later studies on the nature of wave propagation along force chains [OD11, LCKD14, ZHH20].

After extensive research by Oda and colleagues in the 1970s and 1980s using photo-elastic discs, the use of photo-elasticity became a new and dominant tool in gran-

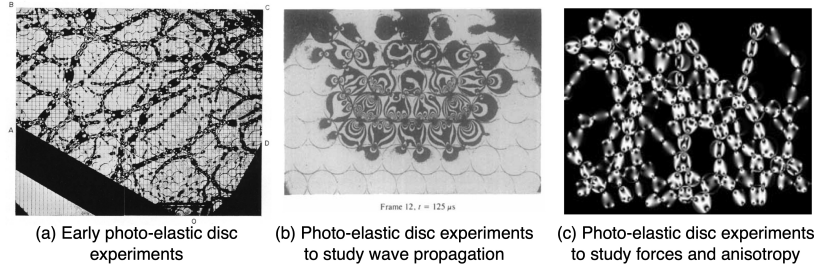


Figure 13: (a) Early photo-elastic disc experiments by Drescher and de Jong in which load-bearing particles exhibit black fringe patterns (reproduced from [DDJ72] with permission). (b) Photo-elastic studies of wave propagation through granular media by Shukla and colleagues (reproduced from [SZS88] with permission). (c) Photo-elastic studies of force statistics and stress-induced anisotropy by Behringer and colleagues (reproduced from [MB05] with permission).

ular physics in the 1990s and 2000s. Experiments in the late 1990s by Howell, Behringer, and colleagues introduced the use of photo-elastic discs in biaxial or annular shear-cell geometries to the field of granular physics and employed these experiments to study stress fluctuations [HBV99b, HBV99a] and inter-particle force statistics and anisotropy [LNS<sup>+</sup>95, VHB99, MB05] during compression and shear (e.g., Fig. 13(c)). These contributions led to significant growth in the use of photo-elasticity in the study of force networks, collective dynamics, and the relationship between forces and transport (see [DKP17] and the references therein). Extensive research with photo-elastic disks has since been used to study forces near jamming, during dynamic penetration, and in relation to bulk properties like conductivity [MSLB07, CKB12, OD11]. Several recent review articles provide an excellent overview of photoelasticity experiments and their use for studying inter-particle forces in granular materials [DKP17, AZBB<sup>+</sup>19].

Photo-elasticity has clearly played a critical role in our understanding of inter-particle forces in granular mechanics, granular physics, geomechanics, and wave propagation throughout the past 50 years. The method of employing photo-elastic discs in simple 2D geometries remains an important and powerful tool for researchers today [DKP17]. The 2D nature of photo-elastic materials and their significant compliance as compared to natural granular materials (e.g. sands) limits the applicability of some prior studies to 3D granular materials and to natural sands and soils. Nevertheless, photo-elastic studies remain critical to future developments in granular mechanics and physics due to their ease of implementation and interpretation.

Several experiments performed after 2015 leveraged multi-modal measurements to examine the behavior of tens to thousands of 3D grains. These experiments were performed in quartz, ruby, sapphire, and sand grains with diameters ranging from 100  $\mu\text{m}$  to 300  $\mu\text{m}$  (e.g. [HHAW16, HLP<sup>+</sup>17, HHW17, HHP18, CAK17]). When com-

bined with appropriate algorithms that quantitatively combined information from x-ray CT (*i.e.*, particle centers and contact locations) and 3DXRD (*i.e.*, particle stresses), these experiments yielded new insight into inter-particle forces and force chains in 3D opaque materials [HHAW16], an insight that was sought by researchers since the first photo-elasticity experiments on discs in the 1950s [Dan57]. The miniaturization of popular testing techniques for granular materials – such as the triaxial test and wave transmission tests – has enabled new experiments to quantitatively link force chains to wave speeds [ZHH20].

## 7 Conclusions

The preceding sections highlight the tremendous progress in *in-situ* full-field imaging in experimental granular mechanics throughout the past few decades. Photography, photo-elasticity, radiography, x-ray tomography and diffraction, and RIMS, among other techniques, have become standard tools for studying the structure, kinematics, and inter-particle forces, the fundamental ingredients of a micro-mechanical description of granular materials. Sections 4 through 6 provided an overview of insights gained during development of the tools within the granular mechanics toolbox described in 3.

In this closing section, we now ask “how are the full-field imaging tools in the granular mechanics toolbox being systematically applied to advance our understanding of granular materials”? Applications of full-field imaging in granular mechanics have become increasingly broad in the past few decades. Researchers are currently applying tools in the toolbox to a very wide variety of phenomena including, but not limited to, rapid flows and compaction, slow flows and non-local constitutive laws, suspension rheology, local rearrangements, and mechanism-based constitutive laws such as continuum breakage mechanics. The promise of full-field tools lies in their ability to furnish the evolution of key variables, such as breakage, porosity, or tensorial quantities like fabric, or in their ability to furnish both stress and strain and thus directly provide a constitutive relation. As a result, full-field tools are increasingly employed to aid in identifying and tracking key variables or fields directly employed in constitutive relations. New tools are also being explored for addition to the toolbox, such as magnetic resonance imaging (MRI or NMR) [Kaw10, HYC<sup>+</sup>04] and light- or x-ray-based holography [ASXW21].

## References

- [AAGK<sup>+</sup>15] R Alikarami, E Andò, M Gkiousas-Kapnisis, A Torabi, and G Viggiani. Strain localisation and grain breakage in sand under shearing at high mean stress: insights from in situ x-ray tomography. *Acta Geotechnica*, 10(1):15–30, 2015.
- [ACDB11] Govind Acharya, Tom Cochrane, Tim Davies, and Elisabeth Bowman. Quantifying and modeling post-failure sediment yields from laboratory-scale soil erosion and shallow landslide experiments with silty loess. *Geomorphology*, 129(1):49–58, 2011.
- [ACKL13] Khalid Alshibli, Mehmet B Cil, Peter Kenesei, and Ulrich Lienert. Strain tensor determination of compressed individual silica sand particles using high-energy synchrotron diffraction. *Granular matter*, 15(5):517–530, 2013.
- [AHV<sup>+</sup>12a] Edward Andò, SA Hall, Gioacchino Viggiani, Jacques Desrues, and Pierre Bésuelle. Experimental micromechanics: grain-scale observation of sand deformation. *Géotechnique Letters*, 2(3):107–112, 2012.
- [AHV<sup>+</sup>12b] Edward Andò, Stephen A Hall, Gioacchino Viggiani, Jacques Desrues, and Pierre Bésuelle. Grain-scale experimental investigation of localised deformation in sand: a discrete particle tracking approach. *Acta Geotechnica*, 7(1):1–13, 2012.
- [And13] Edward Ando. *Experimental investigation of microstructural changes in deforming granular media using x-ray tomography*. PhD thesis, Université de Grenoble, 2013.
- [AS00] Khalid A Alshibli and Stein Sture. Shear band formation in plane strain experiments of sand. *Journal of geotechnical and geoenvironmental engineering*, 126(6):495–503, 2000.
- [ASC<sup>+</sup>00] Khalid Ahmed Alshibli, Stein Sture, Nicholas C Costes, Melissa L Frank, Mark R Lankton, Susan N Batiste, and Roy A Swanson. Assessment of localized deformations in sand using x-ray computed tomography. *Geotechnical Testing Journal*, 23(3):274–299, 2000.
- [ASS05] Tomaso Aste, Mohammad Saadatfar, and TJ Senden. Geometrical structure of disordered sphere packings. *Physical Review E*, 71(6):061302, 2005.
- [ASS06] Tomaso Aste, Mohammad Saadatfar, and Tim J Senden. Local and global relations between the number of contacts and density in monodisperse sphere packs. *Journal of statistical mechanics: theory and experiment*, 2006(07):P07010, 2006.



- [ASXW21] S Aime, M Sabato, L Xiao, and DA Weitz. Dynamic speckle holography. *Physical Review Letters*, 127(8):088003, 2021.
- [AZBB<sup>+</sup>19] Aghil Abed Zadeh, Jonathan Barés, Theodore A Brzinski, Karen E Daniels, Joshua Dijksman, Nicolas Docquier, Henry O Everitt, Jonathan E Kollmer, Olivier Lantsoght, Dong Wang, et al. Enlightening force chains: a review of photoelasticimetry in granular matter. *Granular Matter*, 21(4):1–12, 2019.
- [BCA09] Lydéric Bocquet, Annie Colin, and Armand Ajdari. Kinetic theory of plastic flow in soft glassy materials. *Physical review letters*, 103(3):036001, 2009.
- [BCLvH18] A. Buffler, K. Cole, T.W. Leadbeater, and M.R. van Heerden. Positron emission particle tracking: A powerful technique for flow studies. *International Journal of Modern Physics: Conference Series*, 48:1860113, 2018.
- [BFCTF20] Ian Butler, Florian Fuisseis, Alexis Cartwright-Taylor, and Michael Flynn. Mjölnir: a miniature triaxial rock deformation apparatus for 4d synchrotron x-ray microtomography. *Journal of synchrotron radiation*, 27(6):1681–1687, 2020.
- [BGME18] James Baker, François Guillard, Benjy Marks, and Itai Einav. X-ray rheography uncovers planar granular flows despite non-planar walls. *Nature communications*, 9(1):1–9, 2018.
- [BMV<sup>+</sup>22] Georgios Birmipilis, Amir Saeid Mohammadi, Julie Villanova, Elodie Boller, Edward Ando, and Jelke Dijkstra. Fabric investigation of natural sensitive clay from 3d nano-and microtomography data. *J. Eng. Mech*, 148(2):04021151, 2022.
- [BSM20] Sébastien Brisard, Marijana Serdar, and Paulo JM Monteiro. Multiscale x-ray tomography of cementitious materials: A review. *Cement and Concrete Research*, 128:105824, 2020.
- [CA12] MB Cil and KA Alshibli. 3d assessment of fracture of sand particles using discrete element method. *Géotechnique Letters*, 2(3):161–166, 2012.
- [CA14] MB Cil and KA Alshibli. 3d evolution of sand fracture under 1d compression. *Géotechnique*, 64(5):351–364, 2014.
- [CAK17] Mehmet B Cil, Khalid A Alshibli, and Peter Kenesei. 3d experimental measurement of lattice strain and fracture behavior of sand particles using synchrotron x-ray diffraction and tomography. *Journal of Geotechnical and Geoenvironmental Engineering*, 143(9), 2017.
- [CAKL14] Mehmet B Cil, Khalid Alshibli, Peter Kenesei, and Ulrich Lienert. Combined high-energy synchrotron x-ray diffraction and computed to-



- mography to characterize constitutive behavior of silica sand. *Nuclear Instruments and Methods in Physics Research Section B: Beam Interactions with Materials and Atoms*, 324:11–16, 2014.
- [CCL97] Francesco Calvetti, G Combe, and Jack Lanier. Experimental micromechanical analysis of a 2d granular material: relation between structure evolution and loading path. *Mechanics of Cohesive-frictional Materials: An International Journal on Experiments, Modelling and Computation of Materials and Structures*, 2(2):121–163, 1997.
- [CDDF88] Jean Louis Colliat-Dangus, Jacques Desrues, and Pierre Foray. Triaxial testing of granular soil under elevated cell pressure. In *Advanced triaxial testing of soil and rock*. ASTM International, 1988.
- [CHP<sup>+</sup>19] RS Crum, MA Homel, DC Pagan, EB Herbold, D Miller, J Lind, BJ Jensen, AJ Iverson, and MC Akin. In situ x-ray imaging of heterogeneity in dynamic compaction of granular media. *Journal of Applied Physics*, 125(2):025902, 2019.
- [CKB84] V Cromwell, DJ Kortum, and DJ Bradley. The use of a medical computer tomography (ct) system to observe multiphase flow in porous media. In *SPE Annual Technical Conference and Exhibition*. OnePetro, 1984.
- [CKB12] Abram H Clark, Lou Kondic, and Robert P Behringer. Particle scale dynamics in granular impact. *Physical review letters*, 109(23):238302, 2012.
- [CKLF08] A. Carminati, A. Kaestner, P. Lehmann, and H. Flühler. Unsaturated water flow across soil aggregate contacts. *Advances in Water Resources*, 31(9):1221–1232, 2008. Quantitative links between porous media structures and flow behavior across scales.
- [Cor73] AM Cormack. Reconstruction of densities from their projections, with applications in radiological physics. *Physics in Medicine & Biology*, 18(2):195, 1973.
- [Dan57] P Dantu. A contribution to the mechanical and geometrical study of non-cohesive masses. In *Pros. 4th Int. Conf. Soil Mech. and Found. Eng.*, pages 144–148, 1957.
- [DBB17] Joshua A Dijkstra, Nicolas Brodu, and Robert P Behringer. Refractive index matched scanning and detection of soft particles. *Review of Scientific Instruments*, 88(5):051807, 2017.
- [DCMM96] Jacques Desrues, René Chambon, Moncef Mokni, and Frédéric Mazeur. Void ratio evolution inside shear bands in triaxial sand specimens studied by computed tomography. *Géotechnique*, 46(3):529–546, 1996.

- [DDJ72] A Drescher and G De Josselin De Jong. Photoelastic verification of a mechanical model for the flow of a granular material. *Journal of the Mechanics and Physics of Solids*, 20(5):337–340, 1972.
- [DGB<sup>+</sup>20] Eranga Dulanjalee, François Guillard, James Baker, Itai Einav, and Benjy Marks. Measuring grain size fractions of bidisperse granular materials using x-ray radiography. *Opt. Express*, 28(20):29202–29211, 2020.
- [DH17] Nicolas Denies and Alain Holeyman. Shear strength degradation of vibrated dry sand. *Soil Dynamics and Earthquake Engineering*, 95:106–117, 2017.
- [DKP17] Karen E Daniels, Jonathan E Kollmer, and James G Puckett. Photoelastic force measurements in granular materials. *Review of Scientific Instruments*, 88(5):051808, 2017.
- [DRL<sup>+</sup>12] Joshua A Dijksman, Frank Rietz, Kinga A Lőrincz, Martin van Hecke, and Wolfgang Losert. Invited article: Refractive index matched scanning of dense granular materials. *Review of Scientific Instruments*, 83(1):011301, 2012.
- [DV04] Jacques Desrues and Gioacchino Viggiani. Strain localization in sand: an overview of the experimental results obtained in grenoble using stereophotogrammetry. *International Journal for Numerical and Analytical Methods in Geomechanics*, 28(4):279–321, 2004.
- [EG18] Itai Einav and François Guillard. Tracking time with ricequakes in partially soaked brittle porous media. *Science advances*, 4(10):eaat6961, 2018.
- [FL98] Michael L Falk and James S Langer. Dynamics of viscoplastic deformation in amorphous solids. *Physical Review E*, 57(6):7192, 1998.
- [FMW95] JT Fredrich, Beatriz Menéndez, and T-F Wong. Imaging the pore structure of geomaterials. *Science*, 268(5208):276–279, 1995.
- [Fro41] Max Mark Frocht. *Photoelasticity*, volume 2. J. Wiley, 1941.
- [GCZ<sup>+</sup>21] A Gupta, RS Crum, C Zhai, KT Ramesh, and RC Hurley. Quantifying particle-scale 3d granular dynamics during rapid compaction from time-resolved in situ 2d x-ray images. *Journal of Applied Physics*, 129(22):225902, 2021.
- [GME17] François Guillard, Benjy Marks, and Itai Einav. Dynamic X-ray radiography reveals particle size and shape orientation fields during granular flow. *Scientific Reports*, 7(8155):61–65, 2017.
- [Gou93] R. Gourvès. Application of the schneebli model in the study of micromechanics of granular media. *Mechanics of Materials*, 16(1):125–131, 1993. Special Issue on Mechanics of Granular Materials.

- [HA10] A Hasan and KA Alshibli. Experimental assessment of 3d particle-to-particle interaction within sheared sand using synchrotron microtomography. *Géotechnique*, 60(5):369–379, 2010.
- [HBD<sup>+</sup>10] Stephen A Hall, Michel Bornert, Jacques Desrues, Yannick Pannier, Nicolas Lenoir, Gioacchino Viggiani, and Pierre Bésuelle. Discrete and continuum analysis of localised deformation in sand using x-ray  $\mu$ ct and volumetric digital image correlation. *Géotechnique*, 60(5):315–322, 2010.
- [HBV99a] Daniel Howell, Robert P Behringer, and Christian Veje. Stress fluctuations in a 2d granular couette experiment: a continuous transition. *Physical Review Letters*, 82(26):5241, 1999.
- [HBV99b] Daniel W Howell, RP Behringer, and CT Veje. Fluctuations in granular media. *Chaos: An Interdisciplinary Journal of Nonlinear Science*, 9(3):559–572, 1999.
- [HCD<sup>+</sup>13] M Hudspeth, B Claus, S Dubelman, J Black, A Mondal, N Parab, C Funnell, F Hai, ML Qi, K Fezzaa, et al. High speed synchrotron x-ray phase contrast imaging of dynamic material response to split hopkinson bar loading. *Review of Scientific Instruments*, 84(2):025102, 2013.
- [HHAW16] RC Hurley, SA Hall, JE Andrade, and J Wright. Quantifying interparticle forces and heterogeneity in 3d granular materials. *Phys. Rev. Lett.*, 117(9):098005, 2016.
- [HHP18] Ryan C Hurley, Eric B Herbold, and Darren C Pagan. Characterization of the crystal structure, kinematics, stresses and rotations in angular granular quartz during compaction. *J. Appl. Crystallogr.*, 51(4):1021–1034, 2018.
- [HHW17] RC Hurley, SA Hall, and JP Wright. Multi-scale mechanics of granular solids from grain-resolved x-ray measurements. *Proc. R. Soc. A*, 473(2207):20170491, 2017.
- [HHWH20] N Axel Henningsson, Stephen A Hall, Jonathan P Wright, and Johan Hektor. Reconstructing intragranular strain fields in polycrystalline materials from scanning 3dxrd data. *Journal of applied crystallography*, 53(2):314–325, 2020.
- [HLP<sup>+</sup>17] RC Hurley, J Lind, DC Pagan, MA Homel, MC Akin, and EB Herbold. Linking initial microstructure and local response during quasi-static granular compaction. *Phys. Rev. E*, 96(1):012905, 2017.
- [HLV<sup>+</sup>09] SA Hall, N Lenoir, G Viggiani, J Desrues, and P Bésuelle. Strain localisation in sand under triaxial loading: characterisation by x-ray microtomography and 3d digital image correlation. In *Proceedings of the 1st Int. Symp. On Computational Geomechanics (ComGeo 1)*, pages 239–247, 2009.

- [HOK<sup>+</sup>11] Yosuke Higo, Fusao Oka, Sayuri Kimoto, Taisuke Sanagawa, and Yoshiki Matsushima. Study of strain localization and microstructural changes in partially saturated sand during triaxial tests using microfocus x-ray ct. *Soils and foundations*, 51(1):95–111, 2011.
- [Hou73] Godfrey N Hounsfield. Computerized transverse axial scanning (tomography): Part 1. description of system. *The British journal of radiology*, 46(552):1016–1022, 1973.
- [HV91] C Han and IG Vardoulakis. Plane-strain compression experiments on water-saturated fine-grained sand. *Geotechnique*, 41(1):49–78, 1991.
- [HW15] SA Hall and J Wright. Three-dimensional experimental granular mechanics. *Géotechnique Letters*, 5(4):236–242, 2015.
- [HWP<sup>+</sup>11] Stephen A Hall, Jonathan Wright, Thilo Pirling, Edward Andò, Darren J Hughes, and Gioacchino Viggiani. Can intergranular force transmission be identified in sand? *Granular Matter*, 13(3):251–254, 2011.
- [HYC<sup>+</sup>04] Chao Huan, Xiaoyu Yang, Donald Candela, RW Mair, and RL Walsworth. Nmr experiments on a three-dimensional vibrofluidized granular medium. *Physical Review E*, 69(4):041302, 2004.
- [HZ22] Ryan Hurley and Chongpu Zhai. Challenges and opportunities in measuring time-resolved force chain evolution in 3d granular materials. *Papers in Physics*, 14:140003–140003, 2022.
- [IBO15] M. Iskander, R. Bathurst, and M. Omidvar. Past, present, and future of transparent soils. *Geotechnical Testing Journal*, 38(5):557–573, 2015.
- [Ive97] Richard M Iverson. The physics of debris flows. *Reviews of geophysics*, 35(3):245–296, 1997.
- [JMI<sup>+</sup>19] BJ Jensen, DS Montgomery, AJ Iverson, CA Carlson, B Clements, M Short, and DA Fredenburg. X-ray phase contrast imaging of granular systems. In *Shock Phenomena in Granular and Porous Materials*, pages 195–230. Springer, 2019.
- [JRI<sup>+</sup>14] Brian J Jensen, KJ Ramos, AJ Iverson, J Bernier, CA Carlson, JD Yeager, K Fezzaa, and DE Hooks. Dynamic experiment using impulse at the advanced photon source. In *Journal of Physics: Conference Series*, volume 500, page 042001. IOP Publishing, 2014.
- [KAP<sup>+</sup>18] Zeynep Karatza, Edward Ando, S-A Papanicolopoulos, JY Ooi, and G Viggiani. Evolution of deformation and breakage in sand studied using x-ray tomography. *Géotechnique*, 68(2):107–117, 2018.
- [KAP<sup>+</sup>19] Zeynep Karatza, Edward Andò, Stefanos-Aldo Papanicolopoulos, Gioacchino Viggiani, and Jin Y Ooi. Effect of particle morphology and contacts on particle breakage in a granular assembly studied using x-ray tomography. *Granular Matter*, 21(3):1–13, 2019.

- [Kaw10] Toshihiro Kawaguchi. Mri measurement of granular flows and fluid-particle flows. *Advanced Powder Technology*, 21(3):235–241, 2010.
- [KBB<sup>+</sup>17] MH Khalili, Sébastien Brisard, Michel Bornert, Patrick Aimedieu, J-M Pereira, and J-N Roux. Discrete digital projections correlation: a reconstruction-free method to quantify local kinematics in granular media by x-ray tomography. *Experimental Mechanics*, 57(6):819–830, 2017.
- [KK12] Ken Kamrin and Georg Koval. Nonlocal constitutive relation for steady granular flow. *Physical Review Letters*, 108(17):178301, 2012.
- [KPH12] Felix H Kim, Dayakar Penumadu, and Daniel S Hussey. Water distribution variation in partially saturated granular materials using neutron imaging. *Journal of geotechnical and geoenvironmental engineering*, 138(2):147–154, 2012.
- [KRA<sup>+</sup>18] Ghonwa Khaddour, Ismael Riedel, Edward Andò, Pascal Charrier, Pierre Bésuelle, Jacques Desrues, Gioacchino Viggiani, and Simon Salager. Grain-scale characterization of water retention behaviour of sand using x-ray ct. *Acta Geotechnica*, 13(3):497–512, 2018.
- [LCKD14] Andrea Leonard, Christopher Chong, Panagiotis G Kevrekidis, and Chiara Daraio. Traveling waves in 2d hexagonal granular crystal lattices. *Granular Matter*, 16(4):531–542, 2014.
- [LNS<sup>+</sup>95] C-h Liu, Sydney R Nagel, DA Schecter, SN Coppersmith, Satya Majumdar, Onuttom Narayan, and TA Witten. Force fluctuations in bead packs. *Science*, 269(5223):513–515, 1995.
- [LRF<sup>+</sup>18] Andrew FT Leong, Andrew K Robinson, K Fezzaa, T Sun, N Sinclair, DT Casem, PK Lambert, CJ Hustedt, Nitin P Daphalapurkar, KT Ramesh, et al. Quantitative in situ studies of dynamic fracture in brittle solids using dynamic x-ray phase contrast imaging. *Experimental Mechanics*, 58(9):1423–1437, 2018.
- [MB05] Trushant S Majmudar and Robert P Behringer. Contact force measurements and stress-induced anisotropy in granular materials. *Nature*, 435(7045):1079–1082, 2005.
- [MGB<sup>+</sup>21] Zvonimir Maranic, François Guillard, James Baker, Itai Einav, and Benjy Marks. A granular thermometer. *Granular Matter*, 23(2):1–15, 2021.
- [MSLB07] TS Majmudar, M Sperl, Stefan Luding, and Robert P Behringer. Jamming transition in granular systems. *Physical review letters*, 98(5):058001, 2007.
- [MUNT06] Takashi Matsushima, Kentaro Uesugi, Tsukasa Nakano, and Akira Tsuchiyama. Visualization of grain motion inside a triaxial specimen

- by micro x-ray ct at spring-8. *Advances in X-ray Tomography for Geomaterials*, pages 35–52, 2006.
- [Nes13] Vitali Nesterenko. *Dynamics of heterogeneous materials*. Springer Science & Business Media, 2013.
- [NNT82] S Nemat-Nasser and Y Tobita. Influence of fabric on liquefaction and densification potential of cohesionless sand. *Mechanics of Materials*, 1(1):43–62, 1982.
- [OD11] Eli T Owens and Karen E Daniels. Sound propagation and force chains in granular materials. *EPL (Europhysics Letters)*, 94(5):54005, 2011.
- [OK74] Masanobu Oda and Junichi Konishi. Microscopic deformation mechanism of granular material in simple shear. *Soils and foundations*, 14(4):25–38, 1974.
- [OKNN80] M Oda, J Konishi, and S Nemat-Nasser. Some experimentally based fundamental results on the mechanical behaviour of granular materials. *Geotechnique*, 30(4):479–495, 1980.
- [OKNN82] Masanobu Oda, Junichi Konishi, and Siavouche Nemat-Nasser. Experimental micromechanical evaluation of strength of granular materials: effects of particle rolling. *Mechanics of materials*, 1(4):269–283, 1982.
- [OKNN83] MASANOBU ODA, JUNICHI KONISHI, and SIAVOUCHE NEMAT-NASSER. Experimental micromechanical evaluation of the strength of granular materials: effects of particle rolling. In *Studies in Applied Mechanics*, volume 7, pages 21–30. Elsevier, 1983.
- [ONNK85] Masanobu Oda, Siavouche Nemat-Nasser, and Junichi Konishi. Stress-induced anisotropy in granular masses. *Soils and foundations*, 25(3):85–97, 1985.
- [OSP<sup>+</sup>10] Jette Oddershede, Søren Schmidt, Henning Friis Poulsen, Henning Osholm Sørensen, Jonathan Wright, and Walter Reimers. Determining grain resolved stresses in polycrystalline materials using three-dimensional x-ray diffraction. *Journal of Applied Crystallography*, 43(3):539–549, 2010.
- [OTT04] M Oda, T Takemura, and M Takahashi. Microstructure in shear band observed by microfocus x-ray computed tomography. *Géotechnique*, 54(8):539–542, 2004.
- [PBTJ19] JI Perry, CH Braithwaite, NE Taylor, and AP Jardine. The significance of grain morphology and moisture content on the response of silica sand to ballistic penetration. *Applied Physics Letters*, 115(8):084102, 2019.
- [PCH<sup>+</sup>14] Niranjana D Parab, Benjamin Claus, Matthew C Hudspeth, John T Black, Alex Mondal, Jianzhuo Sun, Kemal Fezzaa, Xianghui Xiao,

- SN Luo, and Wayne Chen. Experimental assessment of fracture of individual sand particles at different loading rates. *International Journal of Impact Engineering*, 68:8–14, 2014.
- [PGH<sup>+</sup>17] Niranjan D Parab, Zherui Guo, Matthew C Hudspeth, Benjamin J Claus, Kamel Fezzaa, Tao Sun, and Weinong W Chen. Fracture mechanisms of glass particles under dynamic compression. *International Journal of Impact Engineering*, 106:146–154, 2017.
- [Pou04] Henning Friis Poulsen. *Three-dimensional X-ray diffraction microscopy: mapping polycrystals and their dynamics*, volume 205. Springer Science & Business Media, 2004.
- [RAS<sup>+</sup>12] Ismael Riedel, Edward Andò, Simon Salager, Pierre Bésuelle, and Gioacchino Viggiani. Water retention behaviour explored by x-ray ct analysis. In *Unsaturated Soils: Research and Applications*, pages 81–88. Springer, 2012.
- [RCD<sup>+</sup>17] Michael E Rutherford, David J Chapman, James G Derrick, Jack RW Patten, Philip A Bland, Alexander Rack, Gareth S Collins, and Daniel E Eakins. Probing the early stages of shock-induced chondritic meteorite formation at the mesoscale. *Scientific reports*, 7(1):1–10, 2017.
- [Rec06] Amy L. Rechenmacher. Grain-scale processes governing shear band initiation and evolution in sands. *Journal of the Mechanics and Physics of Solids*, 54(1):22–45, 2006.
- [RKNS11] K Ramesh, T Kasimayan, and B Neethi Simon. Digital photoelasticity—a comprehensive review. *The Journal of Strain Analysis for Engineering Design*, 46(4):245–266, 2011.
- [Ros63] KH Roscoe. The determination of strains in soils by an x-ray method. *Civ. Engng Publ. Wks Rev.*, 58:873–876, 1963.
- [Ros70] K\_ H\_ Roscoe. The influence of strains in soil mechanics. *Geotechnique*, 20(2):129–170, 1970.
- [RS82] HP Rossmannith and A Shukla. Photoelastic investigation of dynamic load transfer in granular media. *Acta Mechanica*, 42(3):211–225, 1982.
- [Sal93] B. Salm. Flow, flow transition and runout distances of flowing avalanches. *Annals of Glaciology*, 18:221–226, 1993.
- [SAR<sup>+</sup>20a] Olga Stamati, Edward Andò, Emmanuel Roubin, Rémi Cailletaud, Max Wiebicke, Gustavo Pinzon, Cyrille Couture, Ryan Hurley, Robert Caulk, Denis Caillerie, et al. Spam: software for practical analysis of materials. *Journal of Open Source Software*, 5(51):2286, 2020.
- [SAR<sup>+</sup>20b] Eleni Stavropoulou, Edward Andò, Emmanuel Roubin, Nicolas Lenoir, Alessandro Tengattini, Matthieu Briffaut, and Pierre Bésuelle. Dynamics of water absorption in callovo-oxfordian claystone revealed with

- multimodal x-ray and neutron tomography. *Frontiers in Earth Science*, 8:6, 2020.
- [Sch56] G Schneebei. Une analogie mécanique pour les terres sans cohésion, compte rendu. *l'Académie des Sciences, Paris*, 1956.
- [SD87] A Shukla and C Damania. Experimental investigation of wave velocity and dynamic contact stresses in an assembly of disks. *Experimental mechanics*, 27(3):268–281, 1987.
- [SFBA22] Berit Schwichtenberg, Florian Füsseis, Ian B Butler, and Edward Andò. Biotite supports long-range diffusive transport in dissolution–precipitation creep in halite through small porosity fluctuations. *Solid Earth*, 13(1):41–64, 2022.
- [SL88] S. B. Savage and C. K. K. Lun. Particle size segregation in inclined chute flow of dry cohesionless granular solids. *Journal of Fluid Mechanics*, 189:311–335, 1988.
- [SSCB21] Dawa Seo, Changbum Sohn, Mehmet B Cil, and Giuseppe Buscarnera. Evolution of particle morphology and mode of fracture during the oedometric compression of sand. *Géotechnique*, 71(10):853–865, 2021.
- [SSM90] A Shukla, MH Sadd, and H Mei. Experimental and computational modeling of wave propagation in granular materials. *Experimental mechanics*, 30(4):377–381, 1990.
- [Sta17] Ralf Stannarius. Magnetic resonance imaging of granular materials. *Review of Scientific Instruments*, 88(5):051806, 2017.
- [SZS88] A Shukla, CY Zhu, and M Sadd. Angular dependence of dynamic load transfer due to explosive loading in granular aggregate chains. *The Journal of Strain Analysis for Engineering Design*, 23(3):121–127, 1988.
- [Ter20] K von Terzaghi. Old earth pressure theories and new test results. *Engineering News Record*, 85(14):632–637, 1920.
- [TLHY02] Manabu TAKAHASHI, Weiren LIN, Tetsuro HIRONO, and Yuzuru YAMAMOTO. On visualization of inner microstructure in rocks by micro focus x ray ct. *Journal of the Japan Society of Engineering Geology*, 43(4):235–238, 2002.
- [VAVA14] Ivan Vlahinić, Edward Andò, Gioacchino Viggiani, and José E Andrade. Towards a more accurate characterization of granular media: extracting quantitative descriptors from tomographic images. *Granular Matter*, 16(1):9–21, 2014.
- [VHB99] CT Veje, Daniel W Howell, and RP Behringer. Kinematics of a two-dimensional granular couette experiment at the transition to shearing. *Physical Review E*, 59(1):739, 1999.



- [VHRM<sup>+</sup>12] Gioacchino Viggiani, Stephen A Hall, Enrique Edgar Romero Morales, E Tudisco, G Musso, C Jommi, and J Carlos Santamarina. *ALERT Doctoral School 2012: advanced experimental techniques in geomechanics*. ALERT Geomaterials, 2012.
- [VLB<sup>+</sup>04] Gioacchino Viggiani, Nicolas Lenoir, Pierre Bésuelle, Marco Di Michiel, Stefania Marello, Jacques Desrues, and Mogens Kretzschmer. X-ray microtomography for studying localized deformation in fine-grained geomaterials under triaxial compression. *Comptes Rendus Mécanique*, 332(10):819–826, 2004.
- [WAHV17] Max Wiebicke, Edward Andò, Ivo Herle, and Gioacchino Viggiani. On the metrology of interparticle contacts in sand from x-ray tomography images. *Measurement Science and Technology*, 28(12):124007, 2017.
- [WCH<sup>+</sup>16] TM Willey, K Champley, R Hodgins, L Lauderbach, M Bagge-Hansen, C May, N Sanchez, BJ Jensen, A Iverson, and T Van Buuren. X-ray imaging and 3d reconstruction of in-flight exploding foil initiator flyers. *Journal of Applied Physics*, 119(23):235901, 2016.
- [Woo90] David Muir Wood. *Soil behaviour and critical state soil mechanics*. Cambridge university press, 1990.
- [WPAV22] Rui Wang, Gustavo Pinzón, Edward Andò, and Gioacchino Viggiani. Modeling combined fabric evolution in an anisometric granular material driven by particle-scale x-ray measurements. *Journal of Engineering Mechanics*, 148(1):04021120, 2022.
- [YXZ<sup>+</sup>19] Bingxiang Yuan, Lei Xiong, Lihua Zhai, Yuefeng Zhou, Gongfa Chen, Xing Gong, and Wei Zhang. Transparent synthetic soil and its application in modeling of soil-structure interaction using optical system. *Frontiers in Earth Science*, 7:276, 2019.
- [ZGZ<sup>+</sup>20] Wengang Zhang, Xin Gu, Wenhan Zhong, Zhitao Ma, and Xuanming Ding. Review of transparent soil model testing technique for underground construction: Ground visualization and result digitalization. *Underground Space*, 2020.
- [ZHH20] Chongpu Zhai, Eric B Herbold, and Ryan C Hurley. The influence of packing structure and interparticle forces on ultrasound transmission in granular media. *Proceedings of the National Academy of Sciences*, 117(28):16234–16242, 2020.
- [ZWC<sup>+</sup>15] B Zhao, J Wang, MR Coop, Gioacchino Viggiani, and M Jiang. An investigation of single sand particle fracture using x-ray microtomography. *Géotechnique*, 65(8):625–641, 2015.



---

## 2D Image Analysis To Find Particles

**Benjy Marks**

*The University of Sydney*

---

### 1 Introduction

Imaging is a direct method for observing nature, primarily based on spatial and geometrical relationships. It typically involves some kind of wave probing a medium, and the recording of the spatial distribution of that wave after that interaction. The most common day-to-day method of imaging is the use of the human eye to observe nature. When the same process is performed instead by a machine, this is known as photography. This imaging *modality* uses optical light, often coming from the sun, and its reflection from surfaces, as captured by a camera.

For a scientist or engineer, it is important to understand that this image contains data. As with all data, the scope, nature and interpretation of that data is dependent on the observer. In this Chapter, we will begin with a brief discourse on how an image is defined, what it is made of, and some basic operations of dealing with colour and greyscale images. We will then go into two specific use cases for granular materials. One involves finding individual particles inside an image and tracking them over time and is commonly referred to as Particle Tracking Velocimetry (PTV). The second technique, Digital Image Correlation (DIC, also known as Particle Image Velocimetry, or PIV), compares two similar images and tries to estimate the relative displacement between them by texture matching.

### 2 What is an image?

An image is typically a regular 2D array with scalar or vectorial data stored at each point on the array. Each point is referred to as a *pixel*. If the data at each pixel is scalar, then the image is said to be *greyscale*, and the value at each point would be the *greylevel*. A value of zero would correspond to no greyness, and would therefore be black. The maximum possible value would correspond to completely white. (Note that in tomography (discussed elsewhere) this convention is actually inverted for historical reasons).

For a variety of reasons (primarily historical context, data storage and interoperability requirements), images are typically stored as *unsigned integers*, rather than floating point values. The *unsigned* part means that there is no sign to the value, and it, therefore, must be greater than or equal to zero. The fact that it is an *unsigned integer* therefore means that there are a discrete number of values between zero and some maximum greylevel. An 8-bit image would use 8 bits of data storage, each of which could be a 0 or a 1, and would therefore have  $2^8 = 256$  possible greylevel values, with zero corresponding to black and 255 corresponding to white. This *bit depth* is very common in optical imaging. With increasing bit depth, say for a 16-bit image (common in radiography), there are more discrete values available between zero and the maximum (here  $2^{16} = 65,536$ ), and finer changes in greylevel can be stored at the cost of increased file size and computational time.

## 2.1 Getting started with Python

For the code examples below, we will use the programming language Python, which is the most common language for this type of analysis. Many open source packages are available to perform imaging using this language. To follow the worked examples below you will need the following packages installed: `numpy`, `matplotlib` and `imageio`. You can install them at the command line with:

```
pip install numpy matplotlib imageio
```

Once installed, you can load these packages as

```
import numpy as np
import matplotlib.pyplot as plt
import imageio
```

Let's investigate an image we prepared earlier. It is called `rainbow.jpg` and it is a photograph of a rainbow cake. We can load the image in Python using the command `plt.imread()`, which is part of the `matplotlib` package.

```
im = plt.imread('../im/rainbow.jpg') # Load an image of a
↳rainbow cake that we prepared earlier
plt.imshow(im) # show us the image
plt.show() # tell matplotlib to display the image
```



A typical camera records three values at each pixel, one each for the redness, greenness and blueness. We refer to this type of image as red-green-blue (RGB). These values are each recorded by separate sensors, that are sensitive to a range of wavelengths centred around red, green and blue, that are chosen to mimic the behaviour of the (non-colour blind) human eye. Cameras that record more than three values at each pixel are referred to as *multispectral* and are used in a variety of scientific and engineering applications. Cameras that record only a single value at each pixel are referred to as *monochrome* or *black and white*.

If we look a bit closer at the image of the cake, we can investigate what exactly this image is made up of. As stated above, the image is in fact an array of values. We can see what is going on by inspecting the shape of the array `im`.

```
im.shape
```

```
(450, 800, 3)
```

The image is made up of individual pixels. There are 450 rows, 800 columns, and every pixel contains three values, one each for the intensity of red, green and blue. Let's separate the colours into individual two dimensional arrays, each 450 x 800 pixels.

```
# get all of the red pixel values
red = im[:, :, 0]
# get all of the green pixel values
green = im[:, :, 1]
# get all of the blue pixel values
blue = im[:, :, 2]
```

```
print(blue.shape)
```

```
(450, 800)
```

Now we can have a look at each of the colours separately.

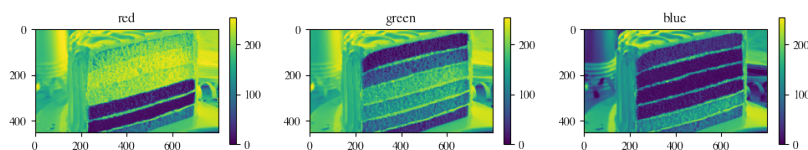
```
# make a new figure, 12 inches wide and 2 inches tall
plt.figure(figsize=[12,2])

# make a plot in the left third of the figure
plt.subplot(131)
# make a title so we don't forget what this subplot is showing
plt.title('red')
# show us just the red data
plt.imshow(red)
# add a colorbar
plt.colorbar()

# now one in the middle third of the figure
plt.subplot(132)
plt.title('green')
plt.imshow(green)
plt.colorbar()

# now the right third of the figure
plt.subplot(133)
plt.title('blue')
plt.imshow(blue)
plt.colorbar()

plt.show()
```



Next to each plot is a *colour bar*. The values in the array have been rendered as a colour that is pulled from a *colour map*. The name of this map is *viridis* and it is the default choice when using *matplotlib*. This particular colour map is *sequential*, in that the colours change systematically from the minimum value to the maximum value. There are other types of colour scales available, such as *diverging* or *qualitative* scales. It is important to note that just because these images are drawn with a set of colours, it does not imply that the underlying data is vectorial. (i.e. RGB). The

ambiguity here necessitates that a colour bar is shown next to all images that are not greyscale. Additionally, not all colour scales are made equal, and [significant research](#) has gone into creating and promoting those that represent data without bias (referred to as *perceptually uniform*), can be printed without significant data loss in greyscale, and are friendly to those with colour blindness.

The values of each of the red, green and blue *channels* above lies somewhere in the range [0-255], and are most likely therefore 8-bit integers. We can check the data type in python via

```
print(im.dtype)
```

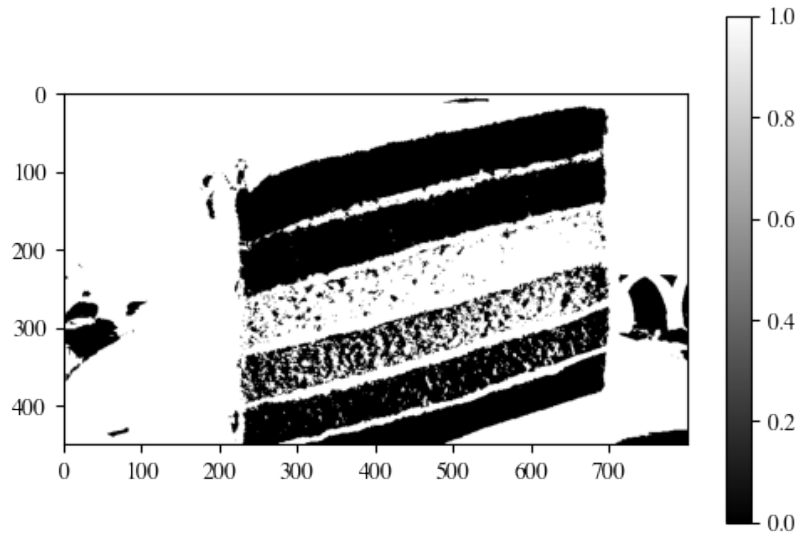
uint8

This tells us that the *data type* is an *unsigned 8 bit integer*, as expected. Now let's try to isolate just the green slice of the cake. One way to do that is by picking a *threshold* value of green, and converting the green subset of the image into a *binary* (or *boolean*) image. This kind of image can only have one of two values at each pixel: True or False.

```
just_green = green > 140
print(just_green.dtype)
```

bool

```
plt.imshow(just_green, cmap='gray') # show the green channel,
    ↳and use the 'gray' colormap so that it is rendered in
    ↳greyscale
plt.colorbar()
plt.show()
```



This has done a reasonable job of isolating the single slice, but it has also selected all of the white areas since whiter colours contain lots of red, green and blue at the same time. In fact, the slice it has selected isn't even the green slice, it is the yellow one. Even though the green slice is 'greener' than the yellow slice, the yellow slice is brighter and therefore has more green in it.

## 2.2 Colour spaces

Whilst an RGB colour image may make sense to be displayed on a computer screen (which these days is typically composed of a large number of tiny lights that glow, unsurprisingly, red, green and blue), it is actually quite inconvenient to find items according to their colour. For this reason, we often change our *colour space* from RGB to another, more convenient space. One such space is the hue-saturation-value (HSV) space.



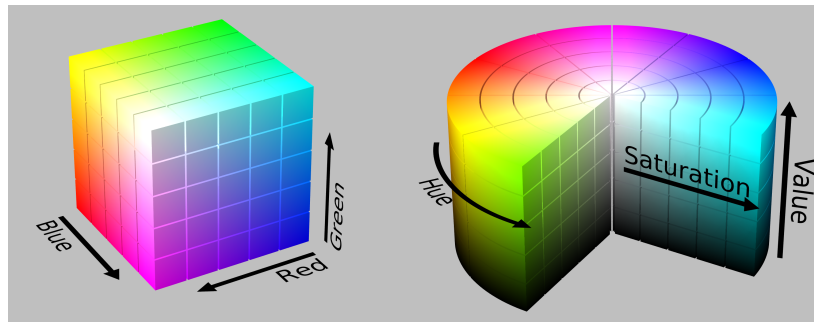


Figure 1: RGB and HSV colour spaces. (wikimedia)

```
from matplotlib.colors import rgb_to_hsv # get the function we need from matplotlib
im_hsv = rgb_to_hsv(im) # Convert to hsv
print(im_hsv.shape)
```

```
(450, 800, 3)
```

We still have an array of the same size, but now instead of being in RGB space, it is in HSV. We can decompose this into three separate arrays with

```
hue = im_hsv[:, :, 0]
saturation = im_hsv[:, :, 1]
value = im_hsv[:, :, 2]
print(hue.shape)
```

```
(450, 800)
```

Let's have a look at what each of these arrays looks like

```
plt.figure(figsize=[12,2])

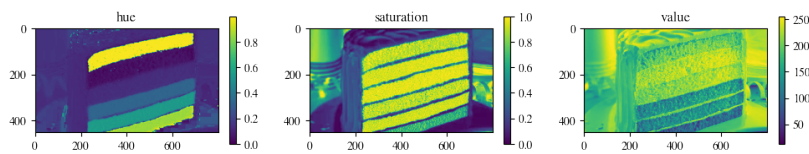
plt.subplot(131)
plt.title('hue')
plt.imshow(hue)
plt.colorbar()

plt.subplot(132)
plt.title('saturation')
plt.imshow(saturation)
```

```
plt.colorbar()

plt.subplot(133)
plt.title('value')
plt.imshow(value)
plt.colorbar()

plt.show()
```



In the *hue* image, we can see that each slice of the cake contains a reasonably uniform hue. Each of those slices has a reasonably high *saturation* because there is a lot of colour there. The *value* image shows us a map of the brightness of the image everywhere. We can look at how frequent each of the values are in these channels with a *histogram*, to get a better idea of exactly what colours we have in the image.

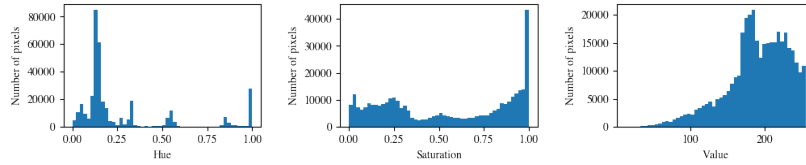
```
plt.figure(figsize=[12,2])

plt.subplot(131)
# we need to flatten the hue array first so that we just get
# one histogram over the whole image
plt.hist(hue.flatten(),bins=50)
plt.xlabel('Hue')
plt.ylabel('Number of pixels')

plt.subplot(132)
plt.hist(saturation.flatten(),bins=50)
plt.xlabel('Saturation')
plt.ylabel('Number of pixels')

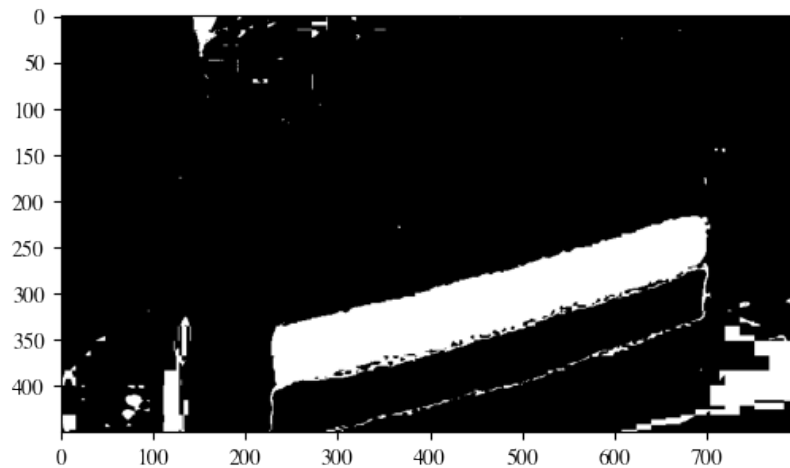
plt.subplot(133)
plt.hist(value.flatten(),bins=50)
plt.xlabel('Value')
plt.ylabel('Number of pixels')

# make a bit more space between the subplots so that we can
# see the labels
plt.subplots_adjust(wspace=0.4)
plt.show()
```



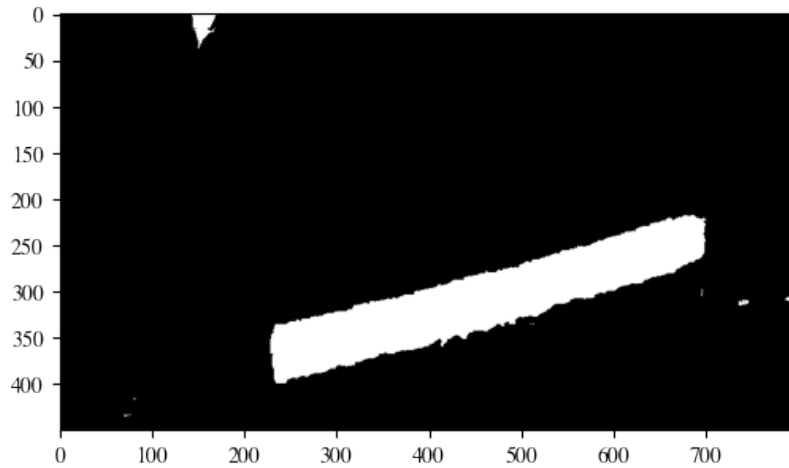
There is a small peak in the hue around 0.3. This must correspond to our green slice. Let's try to extract just these values into a binary image.

```
just_green = (im_hsv[:, :, 0] > 0.2) & (im_hsv[:, :, 0] < 0.4)
plt.imshow(just_green, cmap='gray')
plt.show()
```



Now we're making progress! We have mostly isolated the green slice, but we still have lots of areas of slightly off-coloured white, which we could remove by also including a threshold for our *saturation* value.

```
just_green = (im_hsv[:, :, 0] > 0.2) & (im_hsv[:, :, 0] < 0.4) &
    (im_hsv[:, :, 1] > 0.3)
plt.imshow(just_green, cmap='gray')
plt.show()
```



We are now left with our green slice, and some small parts of the background that are in fact quite a bit green. We will have to do something else to remove those parts.

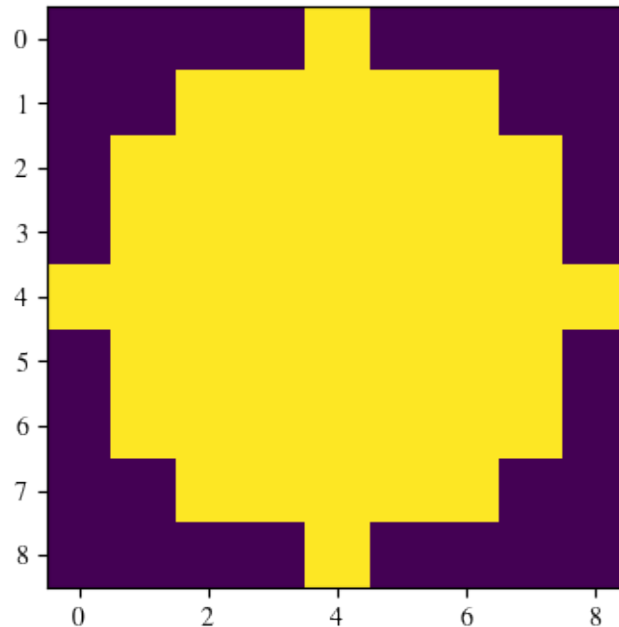
### 3 Morphological operations

There is a family of *morphological operators* which can be applied to binary (or with some extension greyscale) images to remove small areas of data, fill in holes, or other simple tasks. Each of these methods relies on an object referred to as a *structuring element*, or *kernel*. A structuring element is no more than yet another binary image. For example, below is the structuring element that represents a disk of radius 3 pixels.

```
structuring_element = np.array([[0,0,0,0,1,0,0,0,0],
                               [0,0,1,1,1,1,1,0,0],
                               [0,1,1,1,1,1,1,1,0],
                               [0,1,1,1,1,1,1,1,0],
                               [1,1,1,1,1,1,1,1,1],
                               [0,1,1,1,1,1,1,1,0],
                               [0,1,1,1,1,1,1,1,0],
                               [0,0,1,1,1,1,1,0,0],
                               [0,0,0,0,1,0,0,0,0]],
                               dtype=bool)

plt.imshow(structuring_element)
```

<matplotlib.image.AxesImage at 0x165cf7880>



A morphological operation occurs by going past every individual pixel in our image, and placing our structuring element over that pixel, and looking at all of the neighbouring pixels that lie under a True value in the structuring element. In a morphological *dilation*, the value of the pixel of interest is set to True if **any** of the pixels within the structuring element are also True. For a morphological *erosion*, the opposite is the case, and the value of the pixel will be set to False if any of the pixels within the structuring element are False. In this way a dilation will cause areas of True pixels to expand (or dilate), and an erosion will cause areas of Falses to grow, shrinking (or eroding) the True values.

Let us see how this works on our cake slice.

```
from scipy.ndimage import binary_erosion, binary_dilation
eroded = binary_erosion(just_green, structuring_element)
dilated = binary_dilation(just_green, structuring_element)

plt.figure(figsize=[12,2])

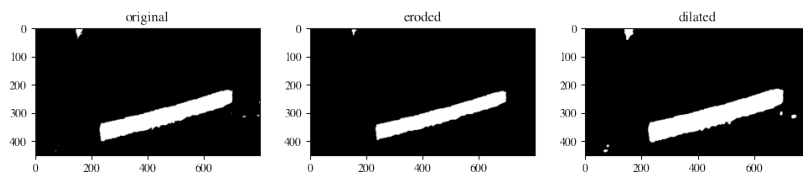
plt.subplot(131)
plt.title('original')
plt.imshow(just_green, cmap='gray')

plt.subplot(132)
```

```
plt.title('eroded')
plt.imshow(eroded, cmap='gray')

plt.subplot(133)
plt.title('dilated')
plt.imshow(dilated, cmap='gray')

plt.show()
```



In the dilated image on the right above, we have managed to grow some of the spurious spots outside of the slice. In the eroded image in the middle, these spots are now gone, but we have also managed to erode away some of the inside of the slice where some small holes existed.

If we now apply the opposite processes, (e.g. first an erosion, and then a dilation), we can try to undo the damage we have caused and get back to almost where we started. These operations are referred to as *opening* and *closing*.

```
opened = binary_dilation(eroded, structuring_element)
closed = binary_erosion(dilated, structuring_element)

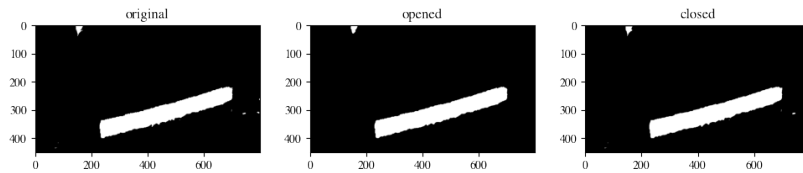
plt.figure(figsize=[12,2])

plt.subplot(131)
plt.title('original')
plt.imshow(just_green, cmap='gray')

plt.subplot(132)
plt.title('opened')
plt.imshow(opened, cmap='gray')

plt.subplot(133)
plt.title('closed')
plt.imshow(closed, cmap='gray')

plt.show()
```



Our closed image looks remarkably similar to our original image. Most of the existing speckle remains, as it is larger than the structuring element. Our opened image, however, is looking rather improved. The smaller speckle has disappeared and the cake slice is back to almost its original shape. Our only remaining issue is the large area at the top of the image, but we can deal with that. The next step is to find the connected region that defines this cake slice and measure its properties.

## 4 Image segmentation

We have now a binary image that closely represents what we want to find. There are large *connected* regions of True values, and we would like to *segment* the image and give different *labels* to each of these connected regions. The largest region, hopefully, will be our cake slice.

```
from scipy.ndimage import label

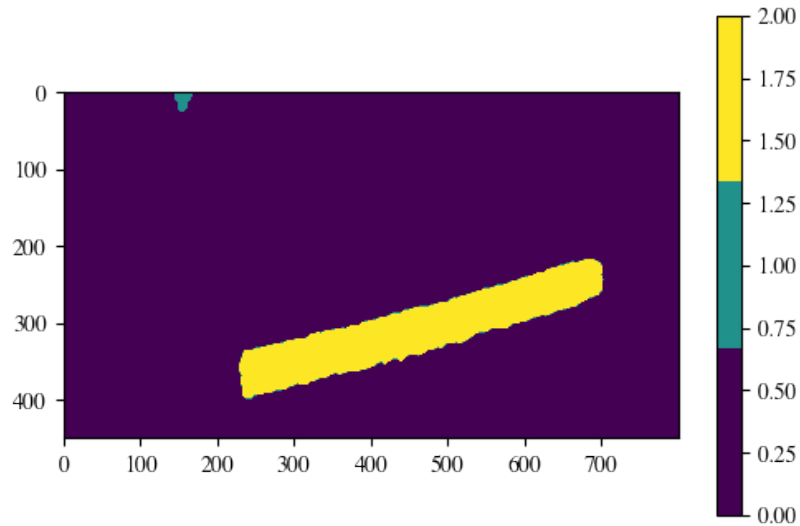
labelled_image, num_features = label(opened)

print(f'Found {num_features} features')

# lets make our own colour map so that we can visualise this properly
from matplotlib import cm
# one colour for each feature and the background
viridis_qualitative = cm.get_cmap('viridis', num_features+1)

plt.imshow(labelled_image, cmap=viridis_qualitative)
plt.colorbar()
plt.show()
```

Found 2 features



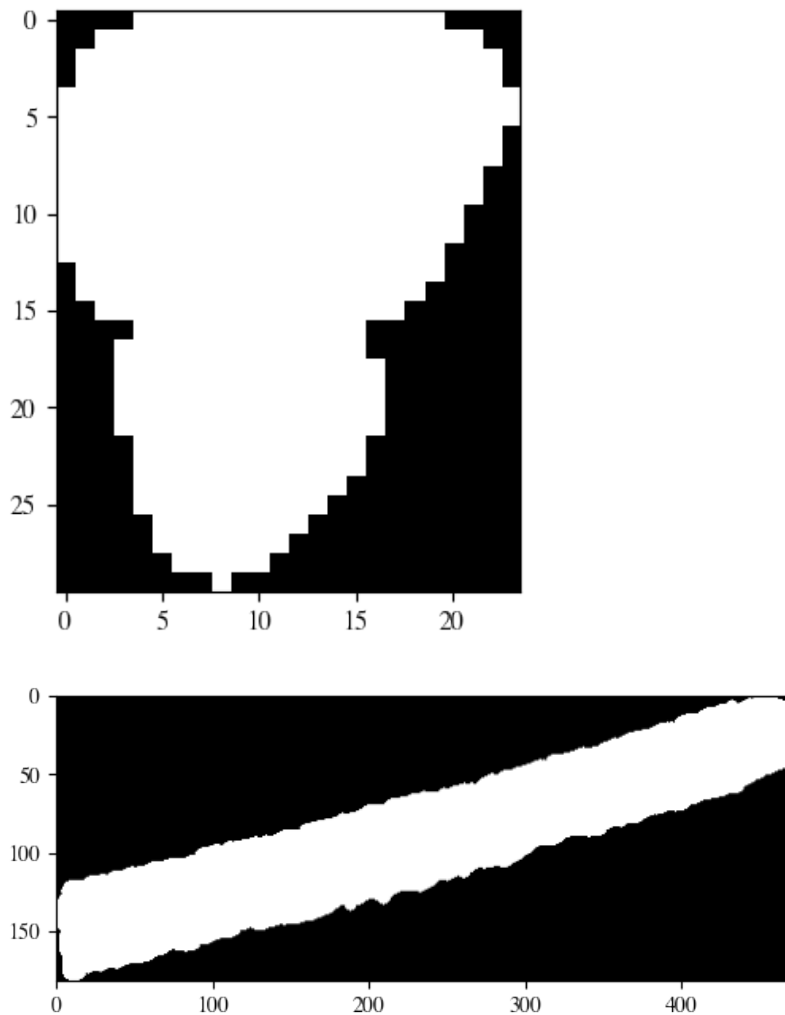
You can see that we have found more than one *feature* in our image (we found two!), and that each connected region of pixels, or feature, has been labelled with an integer value corresponding to its feature number, with the background having a value of zero. The last step is to calculate some properties of each of these labelled regions, which can be achieved by

```
from scipy.ndimage import find_objects

# this is a list of 'slices', or references to where in the
# array the original data is stored
objects = find_objects(labelled_image)

for i in range(len(objects)):
    plt.imshow(labelled_image[objects[i]], cmap='gray')
    plt.show()
```





We can find out the area and location of our objects quite easily.

```
from scipy.ndimage import center_of_mass

# Lets draw some black crosses over the location of the
# regions we found
plt.imshow(im)
for i in range(len(objects)):
    # the 0th label is the background, need to skip it
    c = center_of_mass(opened, labelled_image, [i+1])[0]
    # the area is just the number of pixels in the binary image
```

```

    print(f'Area of object {i+1} is {(labelled_image[objects[i]]).sum()} pixels')
    # annoyingly scipy flips the order of the horizontal and
    # vertical locations
    plt.plot(c[1],c[0], 'kx', markersize=20)

```

Area of object 1 is 480 pixels

Area of object 2 is 55092 pixels



The last remaining step in this instance is just to store only the largest object, but since we have already calculated their areas, this should be relatively straightforward.

## 5 Particle Tracking Velocimetry

### 5.1 Technical digression: loading a video

You will probably at some stage need to load a video with Python. One of the ways to do this is by using the `imageio.get_reader` function. When instantiating this object you are telling Python that you will use a certain video file as a variable. When calling `get_reader()` you still haven't read the frames from the video. See what you can find out about your video file by using the `video.get_meta_data()` method.

```
video = imageio.get_reader('filename.mp4', 'ffmpeg') # change the
filename to whatever your file is called
```

After loading the video, you can now start reading the frames of the video that you will modify. Each frame in the video will be available as a single image.

```
for image in video.iter_data():
```

```
print(image.shape)
```

## 5.2 Exercise 1

Shoot a video of ball flying/bouncing/rolling with your phone or laptop. Then: 1. Load each frame in a loop and do the same procedure as above for each frame. 2. Save the coordinates of the ball's centre into an array. 3. Calculate the horizontal and vertical components of the ball's velocity. 4. Plot the trajectory of the ball on top of the first image of the video. 5. Calculate the initial force applied to the ball and the drag coefficient

## 6 Digital Image Correlation (for beginners)

Depending on the resolution of your image, it may not be possible (or even preferable) to track individual particles in each image. An alternative method, that is used widely across many branches of physics, biology and engineering is *Digital Image Correlation*. This same methodology is also termed *Particle Image Velocimetry*. This technique involves comparing *patches* of each image between frames in a time series, and attempting to find the best possible match so that we can identify where the material has moved between frames.

Necessarily then we must do the following: 1. Record a time series of images 2. Load each image sequentially 3. Split each image into a set of patches 4. For each patch, identify where in the subsequent image we can find that patch

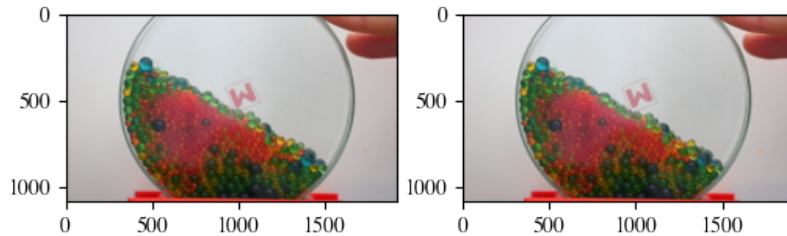
There are many variations of this technique, with varying levels of refinement, accuracy, robustness and reliability. Here, we will detail the simplest, least robust and computationally least efficient method. In a later lecture, further information will be provided on how to do this process better.

Here, we will consider the two following images. As is conventional, we will consider the original, undeformed image to be  $F$ , and the deformed image, where we are trying to find our patches, to be  $G$ :

```
F = plt.imread('../im/DIC/before.png')
G = plt.imread('../im/DIC/after.png')

plt.subplot(121)
plt.imshow(F)
plt.subplot(122)
plt.imshow(G)
plt.show()
```

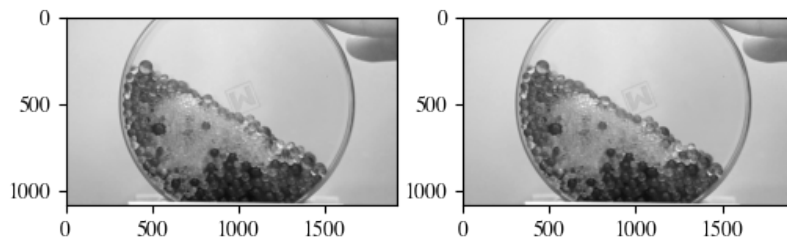
## 56 2D Image Analysis To Find Particles



To process these images, we will need to convert the vectorial RGB images to greyscale. One potential way could be to take the image brightness by converting to HSV and then taking the value channel only.

```
# the third channel is the value
F_gray = rgb_to_hsv(F)[:,:2]
G_gray = rgb_to_hsv(G)[:,:2]

plt.subplot(121)
# use a grayscale colormap so that it looks gray
plt.imshow(F_gray, cmap='gray')
plt.subplot(122)
plt.imshow(G_gray, cmap='gray')
plt.show()
```

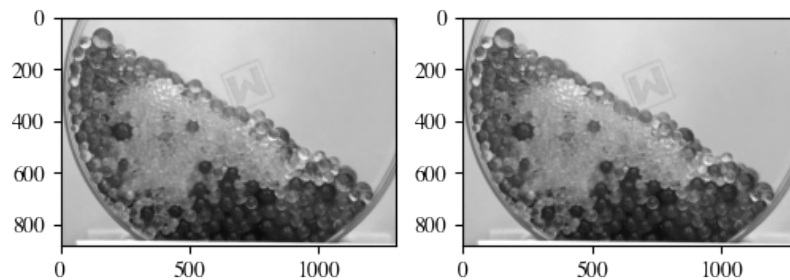


We could tidy up these images by looking for saturated areas, or even more simply by cropping to a region of interest

```
# select from 200 pixels from the top, all the way to the
# bottom, and from 300 pixels from the left to 1600 pixels
# across
F_gray_cropped = F_gray[200:,:300:1600]
G_gray_cropped = G_gray[200:,:300:1600]

plt.subplot(121)
plt.imshow(F_gray_cropped, cmap='gray')
plt.subplot(122)
```

```
plt.imshow(G_gray_cropped, cmap='gray')
plt.show()
```



## 6.1 Patches

Now that we have two nice images ready to process, the next step is to split our image into patches. This necessitates defining

1. What size patches we want
2. Where those patches should be in the image

The choice of patch size should be determined by considering the size of the features of interest in the image. We wish to track these patches between frames, so the patch should be large enough so that features should be persistent between frames. There are in general no formal requirements for the patch size, except that the result of your measurement should be insensitive to small changes in the patch size itself. This could be checked by running your analysis for a variety of patch sizes and examining the result.

For simplicity, patches are typically generated over a grid. The patches themselves, however, can *overlap*, so that the grid spacing is not necessarily the same as the patch size. The more patches used, the finer the resolution of the final data that is produced.

## 6.2 Pixel Searching

Let us pull out a 128 x 128 pixel patch from somewhere inside both images

```
from matplotlib.patches import Rectangle

patch_width = 64
top = 300
left = 500

F_patch = F_gray_cropped[top:top+patch_width,left:
    ↪left+patch_width]
```

```

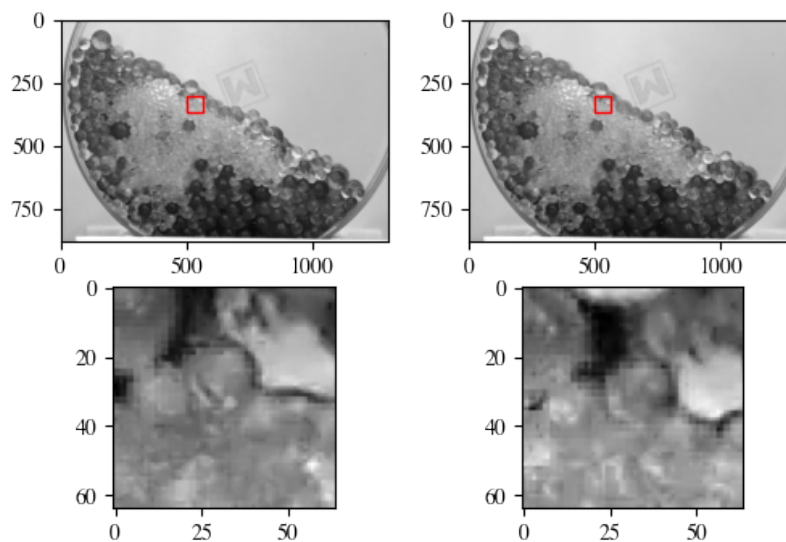
G_patch = G_gray_cropped[top:top+patch_width,left:
    ↪left+patch_width]

ax = plt.subplot(221)
# show the source image
plt.imshow(F_gray_cropped, cmap='gray')
# draw a rectangle to show where our patch came from
ax.add_patch(Rectangle([left,top],
                        patch_width,
                        patch_width,
                        edgecolor='red',
                        facecolor='None'
                        ))

ax = plt.subplot(222)
plt.imshow(G_gray_cropped, cmap='gray')
ax.add_patch(Rectangle([left,top],
                        patch_width,
                        patch_width,
                        edgecolor='red',
                        facecolor='None'
                        ))

plt.subplot(223)
plt.imshow(F_patch,cmap='gray')
plt.subplot(224)
plt.imshow(G_patch,cmap='gray')
plt.show()

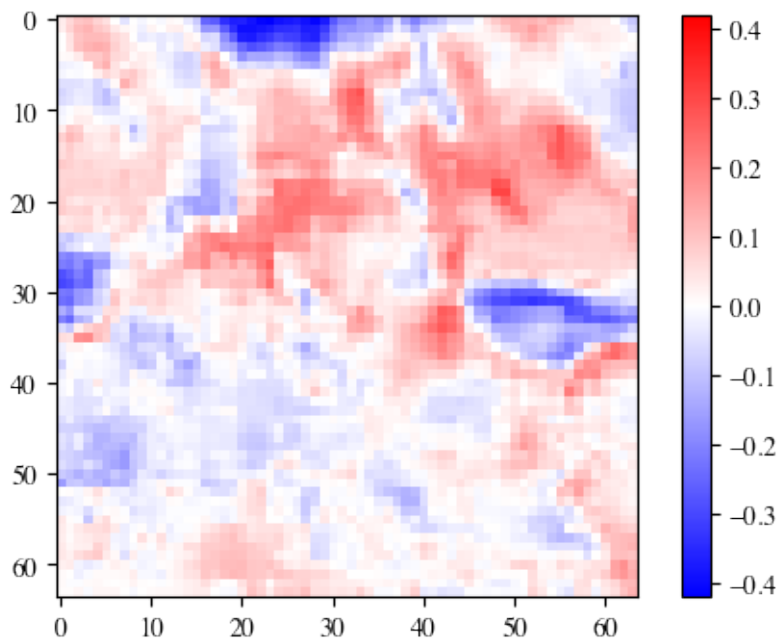
```



We can see if there is any change between the images directly by calculating the difference between the two images

```
err = F_patch-G_patch

plt.imshow(err,
            # set the limits of the colorbar so that the image
            → is symmetrical about zero
            vmin=-np.max(np.abs(err)),
            vmax= np.max(np.abs(err)),
            # render it so that blue is negative and red is
            → positive. This is a diverging colour map.
            cmap='bwr')
plt.colorbar()
plt.show()
```



We can see directly that near the free surface (top right of the image) it is changing a lot, and lower down it is changing less. One way to measure the entire difference between the images would be to calculate the *sum of squared differences* as

$$\eta = \sum_x ((F(x) - G(x))^2$$

where  $x$  are all of the pixels in the two cropped images. This can be done as

```
eta = np.sum(np.square(F_patch - G_patch))
print(eta)
```

38.400955

So there is a measurable difference between these patches. Presumably, that is because the particles have moved between images. Let's see if we can find them by looking not just at this current patch in G, but also in nearby patches

```
# width of the patch
patch_width = 64
# coordinate of the top of the patch
top = 300
# coordinate of the left of the patch
left = 500
# search this many pixels left/right/up/down from the centre
max_search_range = 20

# just use one reference patch
F_patch = F_gray_cropped[top:top+patch_width,left:
    ↳left+patch_width]
# an array to store all of our eta values in
eta = np.zeros([2*max_search_range+1,2*max_search_range+1])
# counter for which dx we are up to
i = 0
# counter for which dy we are up to
j = 0

# list of pixels we want to search over
search_horizontal = np.
    ↳arange(-max_search_range,max_search_range+1)
search_vertical = np.
    ↳arange(-max_search_range,max_search_range+1)

for dx in search_horizontal:
    # reset i for each row
    i = 0
    for dy in search_vertical:
        # move the patch up/down by a distance dy, note that
        ↳positive is down
        this_top = top - dy
        # move the patch left/right by a distance dx
        this_left = left + dx
```

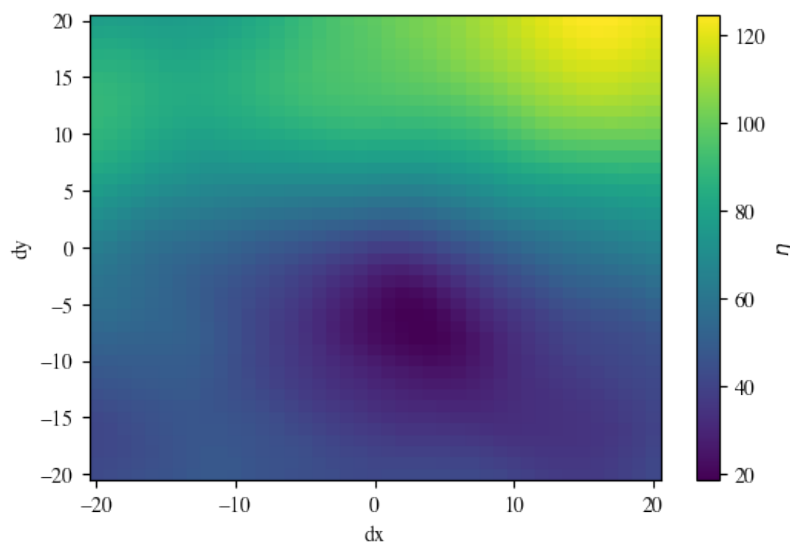


```

        # get this patch
        G_patch = G_gray_cropped[this_top:
    ↪ this_top+patch_width,this_left:this_left+patch_width]
        # calculate the sum of squared differences
        eta[i,j] = np.sum(np.square(F_patch - G_patch))
        # increment i by 1
        i += 1
    # increment j by 1
    j += 1

plt.
    ↪ pcolormesh(search_horizontal,search_vertical,eta,shading='auto')
plt.xlabel('dx')
plt.ylabel('dy')
plt.colorbar(label='$\eta$')
plt.show()

```



As we can see, the total error varies when we move the patch around. The minimum error will give us the best match between the two patches, and we therefore can identify that the material has moved to the right and down. We can calculate the displacement as

```

# get the indices of the minima from eta
j,i = np.unravel_index(eta.argmin(), eta.shape)
# find the corresponding dx and dy
displacement_x = search_horizontal[i]

```

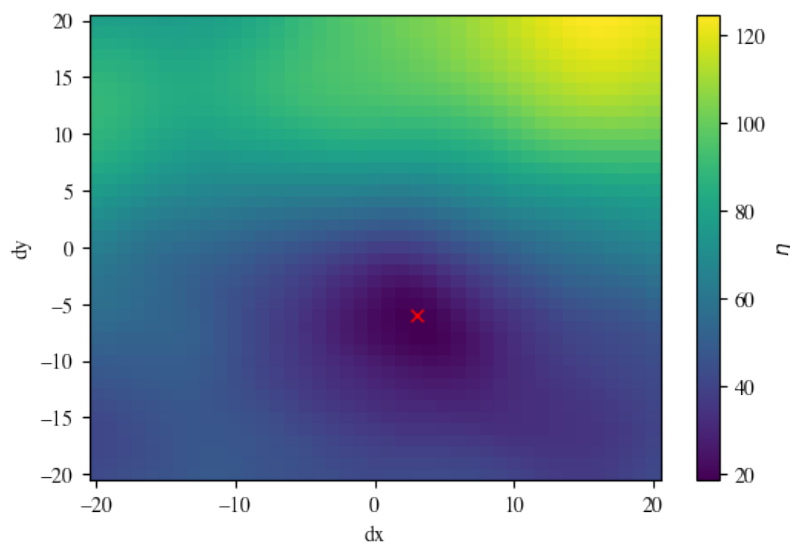
```

displacement_y = search_vertical[j]
print(displacement_x, displacement_y)

plt.
    ↳ pcolormesh(search_horizontal,search_vertical,eta,shading='auto')
plt.plot(displacement_x,displacement_y,'rx')
plt.xlabel('dx')
plt.ylabel('dy')
plt.colorbar(label='$\eta$')
plt.show()

```

3 -6



After applying this technique to a large number of patches, it is possible to recover the following velocity field.



Figure 2: Velocity field as calculated by Digital Image Correlation.

This patch of material appears to flow down and to the right, and moved approximately 3 pixels to the right while moving 6 pixels downwards. We can repeat this process for many different patches to create a full field of measurements of the displacement.

### 6.3 What to do with all of this data?

In many geotechnical applications, we typically want to relate the strain with the stress. We don't have much of an idea (yet!) about the stress field, but we can calculate the strain field quite easily since the velocity field is calculated on a regular grid. If we have two 2-dimensional arrays  $u$  and  $v$  that represent the horizontal and vertical velocity, with grid spacings  $dx$  and  $dy$ , we can calculate the volumetric and shear strain rates as

```
du_dx, du_dy = np.gradient(u,dx,dy)
dv_dx, dv_dy = np.gradient(v,dx,dy)
```

```
volumetric_strain_rate = (du_dx + dv_dy)/2.
shear_strain_rate = (du_dy + dv_dx)/2.
```

### 6.4 Software options

There are many free, open source alternatives for performing digital image correlation. A non-exhaustive list of common options as of 2022 are:

- MATLAB based:
  - [PIVLab](#)

- [GeoPIV-RG](#)
- Python based:
  - [OpenPIV](#)
  - [spam](#)
- Smartphone based:
  - [SmartPIV for Android](#)
  - [SmartPIV for iPhone](#)

## 6.5 Exercise 2

Using the same video as in Exercise 1 above, measure the velocity field for each frame on a regular grid. Create a graph of the volumetric strain rate of the centre of the ball as a function of its acceleration.

---

# Photoelasticity: Stresses and Forces in 2D

**Ryan Hurley**

*Johns Hopkins University  
Department of Mechanical Engineering*

---

Here we provide a brief introduction to the use of photoelasticity for full-field stress measurements in 2D. A brief history, an overview of the fundamental concepts, and some examples are provided. Techniques for calculating stresses from fringe patterns and the more common technique in the granular mechanics community for calculating forces from light intensity are described. A sample dataset and set of analysis codes will be provided during the doctoral school.

## 1 Introduction

Photoelasticity provides a means of obtaining full-field stresses in 2D granular materials. While 2D granular materials are not natural geomaterials, they serve as excellent model systems in which to study phenomena that appear in 3D granular materials found in geomechanics applications and nature. For instance, as described in the introduction chapter to the ALERT school, 2D photoelasticity studies have shed light on force chains [DDJ72], stress-strain coaxiality [DDJ72], fabric [OK74, ONNK85], wave propagation [SZS88, OD11], shear-induced anisotropy [MB05], impact response [CKB12], and granular fault gouge [DH08]. Although these concepts and processes were necessarily studied in 2D with photoelasticity, they have analogies and important implications in 3D. The 2D photoelasticity studies often motivate or support 3D studies, which are typically more challenging or even impossible to perform with the same full-field resolution.

The principle of birefringence was discovered in the 1800s by Brewster and first employed systematically in stress analysis of solids in the 1930s by Coker and Filon [Sha08]. A variety of methods exist for photoelastic stress analysis of solids, involving the use of photoelastic films, linear and circular polariscopes, full-spectrum (RGB) and monochromatic light [DKP17, Sha08, HYK98]. Excellent review articles have recently been written on photoelasticity for analysis of stresses and forces in granular materials [DH08, AZBB<sup>+</sup>19]. These articles include both scientific results and practical details on implementation.

In this chapter, we focus narrowly on the fundamental equation for fringe patterns obtained from a typical darkfield polariscope and the commonly-used  $G^2$  technique for inferring forces based directly on light intensity.

## 2 Experimental setup

### 2.1 Material Basics

Many transparent materials, including glass and polymers, demonstrate the photoelastic effects – these materials are called *birefringent*. However, many objects of modern-day life, like glasses worn to improve vision, require significant stresses to induce observable birefringence or photoelastic effects. Studies of 2D granular materials therefore typically rely on more compliant materials such as urethane, gels, and off-the-shelf PhotoStress materials (e.g., those from Vishay [DKP17]). An online resource (<https://git-xen.lmgc.univ-montp2.fr/PhotoElasticity/Main/-/wikis/home>) provides information on a material preparation for photoelasticity experiments. Many off-the-shelf products are now available that can be cast or cut into desired shapes for photoelastic studies. Figure 1, borrowed from [AZBB<sup>+</sup>19], illustrates several examples of particle types and materials that can be used in photoelasticity experiments.

### 2.2 Experimental Configurations and Basic Theory

There are a variety of experimental configurations that one may use in photoelasticity studies. These configurations vary in their use, orientation, and ordering of linear polarizers, quarter-wave plates, cameras, and light sources [DKP17, Sha08]. Two common configurations include the darkfield linear polariscope and the darkfield circular polariscope. Because of issues in decoupling relative polarizer angles and principal stresses in a darkfield linear polariscope, it is most common to use a darkfield circular polariscope in quantitative and semi-quantitative photoelasticity studies of granular materials [DKP17].

Typical darkfield circular polariscopes used to study 2D granular materials include those based on light propagation through two sets of polarizers and quarter-wave plates which sandwich a photoelastic material, and those based on light transmission and reflection through polarizers located above a granular material positioned on a mirror. These two configurations of polariscopes are shown in Fig. 2 and Fig. 3, respectively.

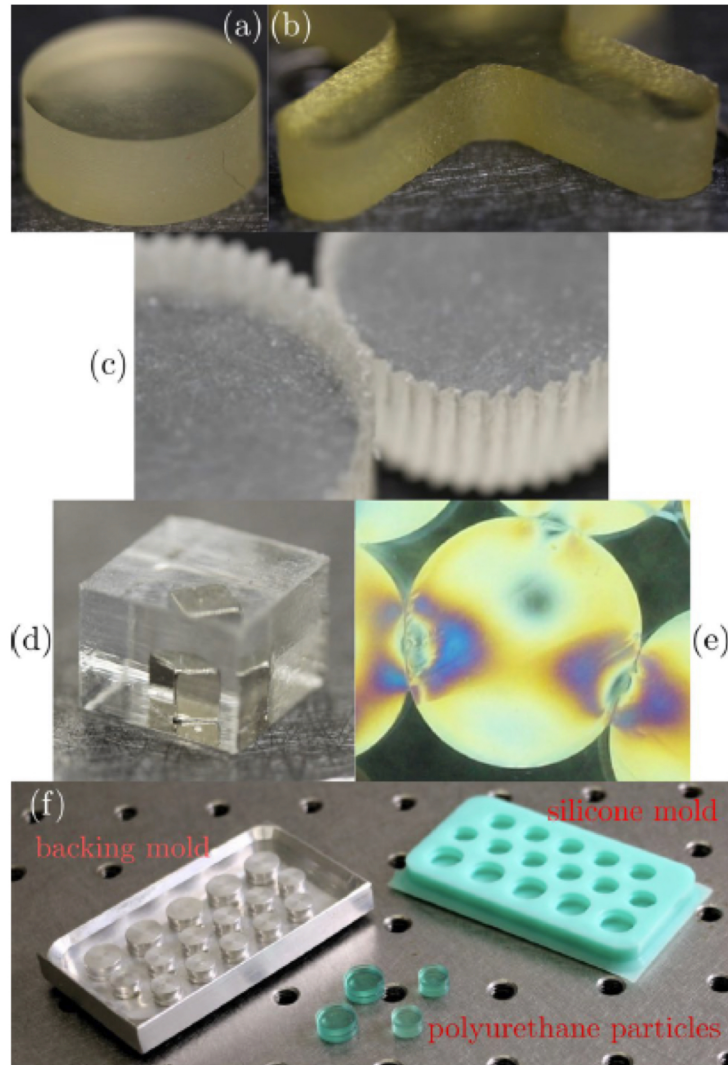


Figure 1: Photoelastic particles and preparation techniques. Borrowed from [AZBB<sup>+</sup>19]. (a) and (b) show a disc and cross-shaped particle cut out of a photoelastic sheet from Precision Urethane (<https://www.precisionurethane.com/polyurethane-pads.html>) using a rotating cookie-cutter and milling machine, respectively. (c) Gear-shaped particles cut out of same sheet using a waterjet. (d) Cast urethane embedded with a magnetic inclusion. (e) Molded gelatin observed through crossed polarizers. (f) Molds used to to cast polyurethane particles.

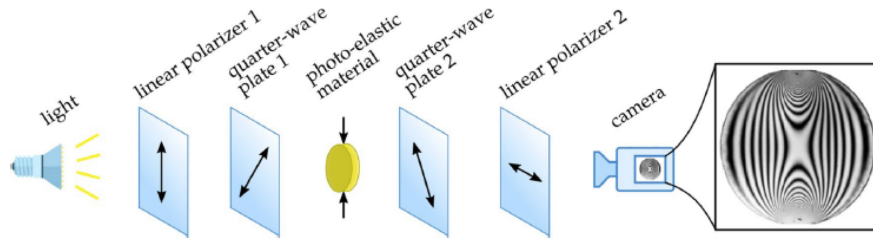


Figure 2: Transmission-based darkfield circular polarizer. A photoelastic material is sandwiched between two sets of quarter-wave plates and linear polarizers, the latter featuring a  $90^\circ$  relative rotation of their polarization direction. A monochromatic light illuminates the sample and a camera captures an image of the resulting fringe patterns, which develops due to principal stress differences as described in the text. Figure borrowed from [AZBB<sup>+</sup>19].

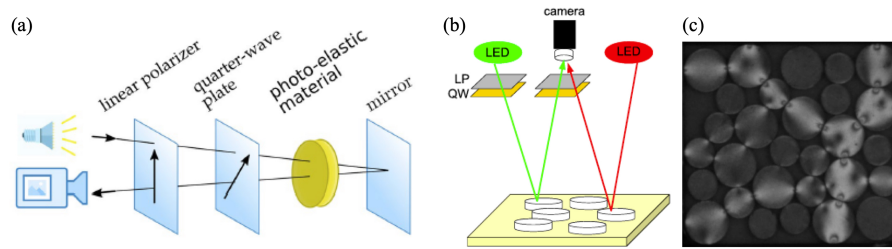


Figure 3: Reflection-based darkfield circular polarizer. (a) A photoelastic material is located between a single linear polarizer and quarter-wave plate and a mirror. Light is transmitted through the system, reflected back from the mirror, and imaged from a camera in a similar location as the light. (b) A schematic of a typical experiment in which particles are placed horizontally on a low-friction plate which sits on a mirror. (c) An image of compressed photoelastic discs from an experiment employing the setup shown in (a) and (b). Images borrowed from [AZBB<sup>+</sup>19, DKP17].

The fundamental optical elements upon which darkfield polariscopes are based are linear polarizers and quarter-wave plates. When a linear polarizer and quarter-wave plate are combined, the resulting unit is referred to as a circular polarizer. This unit works by converting unpolarized, omni-directional light first into linearly polarized and finally circularly polarized light, as shown in Fig. 4. After passing through a circular polarizer, the light then transits through a stressed quasi-2D photoelastic material, such as a disc in a 2D granular material, before transiting through another circular polarizer.



When light emerges, there is a phase shift of orthogonal wave components given by

$$\delta = \frac{2\pi C d}{\lambda} (\sigma_1 - \sigma_2), \quad (1)$$

where  $C$  is the stress-optical coefficient,  $d$  is the thickness of the granular material,  $\lambda$  is the wavelength of light, and  $\sigma_1$  and  $\sigma_2$  are orthogonal principal stresses in the plane perpendicular to the direction of light propagation (where  $\sigma_1 > \sigma_2$ ). This equation is known as the stress-optic (or Brewster's) law. Through further mathematical analysis, one can show that the intensity of transmitted light through the entire system,  $I$ , can be written as [Sha08]

$$I = I_0 \sin^2 \frac{\delta}{2} = I_0 \sin^2 \left( \frac{2\pi C d}{\lambda} (\sigma_1 - \sigma_2) \right), \quad (2)$$

where  $I_0$  is the intensity of incident light.

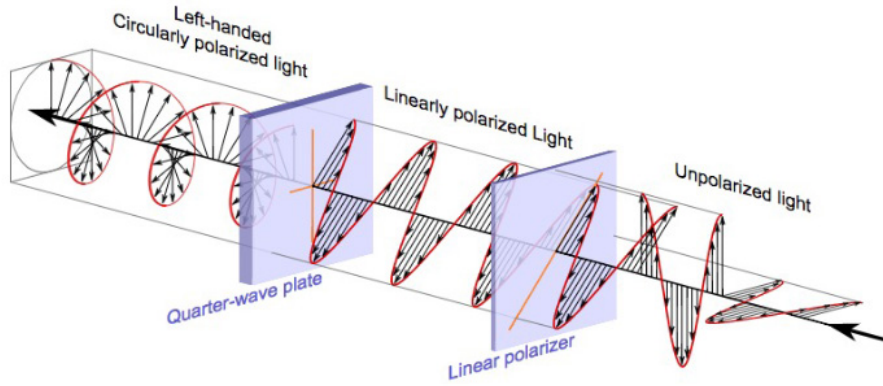


Figure 4: Left-hand circular polarizer <https://en.wikipedia.org/wiki/Polarizer>.

### 3 Analysis of Photoelastic Images

In order to track the positions and kinematics, contact fabric, and inter-particle forces in a photoelastic granular material, image analysis must be performed. Analysis of 2D images for particle locations and contacts will be covered elsewhere in the doctoral school. Here, we simply focus on inter-particle forces.

The fringe patterns observed in the discs Fig. 3c reflect variations in the principal stress difference,  $\sigma_1 - \sigma_2$ , as well as the variations in the periodic function  $\sin^2(\delta/2)$ . Analysis of individual fringes and fringe order is possible and often undertaken in traditional photoelasticity [Sha08]; it is also possible in granular materials using techniques pioneered by Majmudar and Behringer [MB05, DKP17]. Such an approach

yields the vector inter-particle forces. For the purposes of this text, we will mainly explore the simpler and now more-common force analysis technique used in granular materials known as the gradient-squared or  $G^2$  method.

### 3.1 Scalar Force Inference or the $G^2$ Method

For many studies of stress transmission in granular materials, it is sufficient to analyse the sum of forces on a particle. The sum of forces, or a scalar measure of average pressure, on a particle correlates remarkably well with the magnitude of the gradient of the image intensity within a particle [ZZW<sup>+</sup>19], even when the number of inter-particle contacts is large. To demonstrate this, consider the simulations performed in [ZZW<sup>+</sup>19] of a particle in contact with between two and ten neighbouring grains. Results of these simulations are plotted in Fig. 5. Figure 5(a) shows the relationship between  $G^2$  and  $P$ . Here,  $G^2$  is defined as

$$G^2 = \langle |\nabla I_{i,j}|^2 \rangle = \frac{1}{4} \left[ \left( \frac{I_{i-1,j} - I_{i+1,j}}{2} \right)^2 + \left( \frac{I_{i-1,j-1} - I_{i+1,j+1}}{2\sqrt{2}} \right)^2 \right] + \frac{1}{2} \left[ \left( \frac{I_{i,j-1} - I_{i,j+1}}{2} \right)^2 + \left( \frac{I_{i-1,j} - I_{i+1,j}}{2\sqrt{2}} \right)^2 \right]$$

$P$  is defined as  $P = \sum_i |\mathbf{F}_i| / (2\pi R)$ , where  $R$  is the radius of each particle and  $|\mathbf{F}_i|$  is the force magnitude at contact  $i$  on a particle.

This method, the gradient-squared or  $G^2$  method, has been used extensively to study system scale stress response in photoelastic granular packings (*e.g.* [CWBB16, HBV99, DKP17]) and grain-scale stress response (*e.g.* [WRD<sup>+</sup>18, CKB12, ZWT<sup>+</sup>19]). The benefits of using  $G^2$  in evaluating grain-level stress are: (1) it works well even with lower-resolution images with about 10 pixels across a particle; (2) processes is very fast compared to more rigorous methods; (3) only a single experiment, involving diametric compression of a single photoelastic disk, is required to calibrate the method.

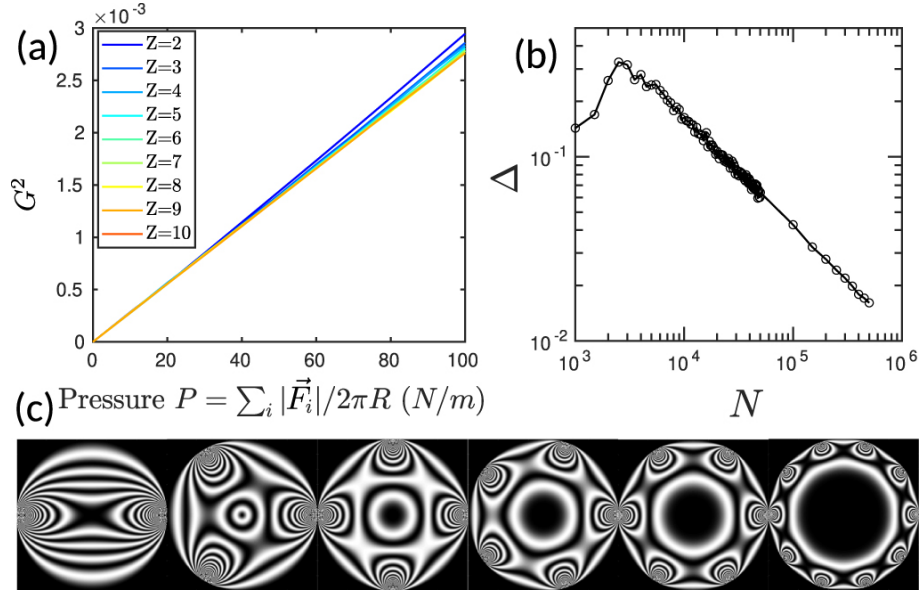


Figure 5: Results from simulating a particle with  $Z$  contacts. (a)  $G^2$ , as defined in text, of pixels within each particle. (b) Difference in  $G^2$  computed as  $(G^2(Z=2, P=100 \text{ N/m}) - G^2(Z=10, P=100 \text{ N/m})) / (G^2(Z=2, P=100 \text{ N/m}))$ , demonstrating a very small difference in the  $G^2$  value for grains with two versus ten contacts. (c) Simulated photoelastic fringes used in quantitative analysis in the remainder of the figure. Image borrowed from [ZZW<sup>+</sup>19].

### 3.2 Vector Force Inference

A more rigorous approach to the inference of vector inter-particle forces in photoelasticity images involves the use of simulation and numerical optimisation. This approach was developed by [Maj06] and involves the following steps: (1) detecting particle positions through analysis of photoelastic images; (2) generating an initial guess for the total and individual contact force magnitudes; (3) using an analytical solution to estimate stress distribution and fringe pattern in each particle and comparing the result with the experimental image. The last step is usually achieved first by using known analytical solutions for point-loaded disks from elasticity theory. An optimisation algorithm is then used to compare the analytical intensity and measured intensity at each pixel in a particle. The optimisation algorithm most often used is the Levenberg-Marquardt algorithm [DKP17], which is implemented in Matlab. An open-source code for performing photoelastic force analysis is available on GitHub <https://github.com/jekollmer/PEGS>. A representation of this technique is shown in Figure 6.

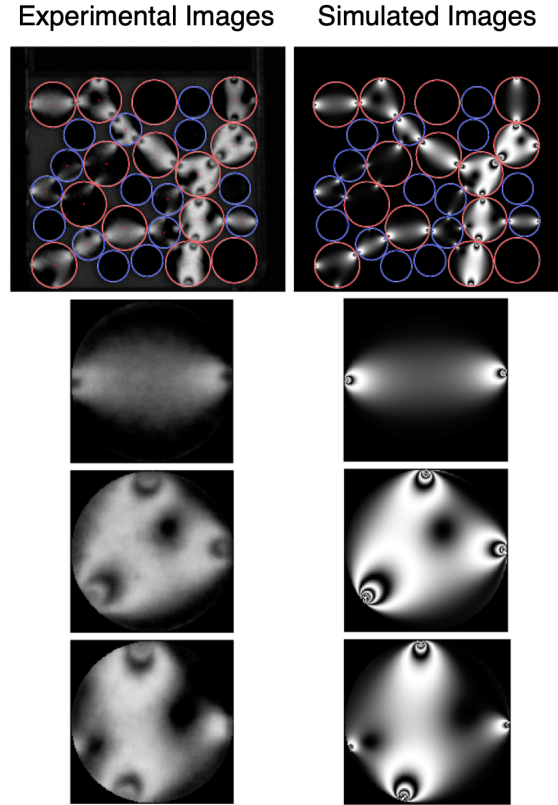


Figure 6: Experimentally-measured images of a small packing of photoelastic discs. The left column shows the experimental images, including three particles isolated from the full experimental image with two, three, and four inter-particle contacts. The right column shows the simulated images obtained from the optimisation procedure for vector inter-particle forces described in the text. Image from [DKP17].

## 4 Implications for Experimental Geomechanics

Photoelasticity has been widely adopted for studying the system-scale and grain-scale stress responses of granular packings. The geomechanics researcher is often interested in phenomena related to constitutive laws which involve the evolution of both stress and strain fields throughout their materials. For researchers studying granular geomaterials, the potential applications of using photoelasticity should be readily apparent. As described in the introduction of this chapter, fundamental insight into the nature of granular materials has been gained from photoelastic studies, including insight into the nature of force chains, stress-strain coaxiality, contact and force fabric, wave propagation, shear induced anisotropy, impact response, and granular fault

gouge. Notable recent contributions of interest to the geomechanics researcher include studies of stresses and strains around shear bands (*e.g.* [ZWT<sup>+</sup>19, Guo12, LNTP20] and Fig. 7).

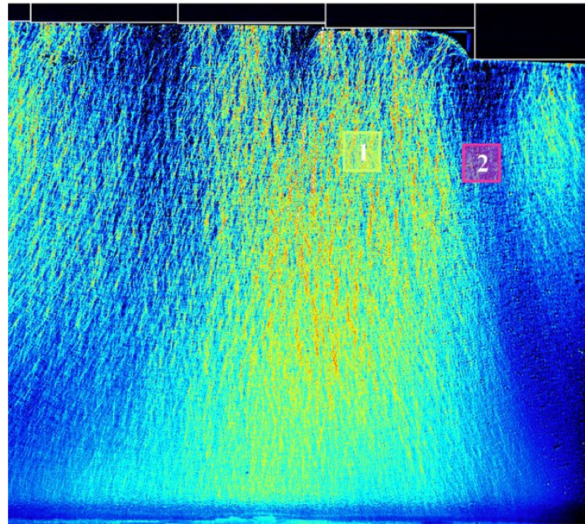


Figure 7: Shear band (labelled with a 2) developed beneath a region of active vertical pressure. Image from [LNTP20].

For researchers studying geomaterials other than granular materials, photoelasticity can still be a useful laboratory tool. For poorly lithified sandstones, loose granular materials are often good analogue for laboratory studies [HB19], making photoelastic discs an applicable laboratory medium for study. For studies of stress concentrations in other geomaterials such as deeply buried rock masses and concrete, samples containing voids or inclusions embedded in a photoelastic matrix have been used [WJX<sup>+</sup>17, JWX<sup>+</sup>17].

## References

- [AZBB<sup>+</sup>19] Aghil Abed Zadeh, Jonathan Barés, Theodore A Brzinski, Karen E Daniels, Joshua Dijkstra, Nicolas Docquier, Henry O Everitt, Jonathan E Kollmer, Olivier Lantsoght, Dong Wang, et al. Enlightening force chains: a review of photoelasticimetry in granular matter. *Granular Matter*, 21(4):1–12, 2019.
- [CKB12] Abram H Clark, Lou Kondic, and Robert P Behringer. Particle scale dynamics in granular impact. *Physical review letters*, 109(23):238302, 2012.
- [CWBB16] Meredith Cox, Dong Wang, Jonathan Barés, and Robert P Behringer. Self-organized magnetic particles to tune the mechanical behavior of a granular system. *EPL (Europhysics Letters)*, 115(6):64003, 2016.
- [DDJ72] A Drescher and G De Josselin De Jong. Photoelastic verification of a mechanical model for the flow of a granular material. *Journal of the Mechanics and Physics of Solids*, 20(5):337–340, 1972.
- [DH08] Karen E Daniels and Nicholas W Hayman. Force chains in seismogenic faults visualized with photoelastic granular shear experiments. *Journal of Geophysical Research: Solid Earth*, 113(B11), 2008.
- [DKP17] Karen E Daniels, Jonathan E Kollmer, and James G Puckett. Photoelastic force measurements in granular materials. *Review of Scientific Instruments*, 88(5):051808, 2017.
- [Guo12] Peijun Guo. Critical length of force chains and shear band thickness in dense granular materials. *Acta Geotechnica*, 7(1):41–55, 2012.
- [HB19] Suzanne JT Hangx and Nicolas Brantut. Micromechanics of high-pressure compaction in granular quartz aggregates. *Journal of Geophysical Research: Solid Earth*, 124(7):6560–6580, 2019.
- [HBV99] Daniel Howell, Robert P Behringer, and Christian Veje. Stress fluctuations in a 2d granular couette experiment: a continuous transition. *Physical Review Letters*, 82(26):5241, 1999.
- [HYK98] Shunji Hirokawa, Kouji Yamamoto, and Takashi Kawada. A photoelastic study of ligament strain. *IEEE Transactions on Rehabilitation Engineering*, 6(3):300–308, 1998.
- [JWX<sup>+</sup>17] Yang Ju, Li Wang, Heping Xie, Guowei Ma, Lingtao Mao, Zemin Zheng, and Jinbo Lu. Visualization of the three-dimensional structure and stress field of aggregated concrete materials through 3d printing and frozen-stress techniques. *Construction and Building Materials*, 143:121–137, 2017.

- [LNT20] D Leśniewska, Michał Nitka, J Tejchman, and M Pietrzak. Contact force network evolution in active earth pressure state of granular materials: photo-elastic tests and dem. *Granular Matter*, 22(3):1–31, 2020.
- [Maj06] Trushant Suresh Majmudar. *Experimental studies of two-dimensional granular systems using grain-scale contact force measurements*. PhD thesis, Duke University, 2006.
- [MB05] Trushant S Majmudar and Robert P Behringer. Contact force measurements and stress-induced anisotropy in granular materials. *Nature*, 435(7045):1079–1082, 2005.
- [OD11] Eli T Owens and Karen E Daniels. Sound propagation and force chains in granular materials. *EPL (Europhysics Letters)*, 94(5):54005, 2011.
- [OK74] Masanobu Oda and Junichi Konishi. Microscopic deformation mechanism of granular material in simple shear. *Soils and foundations*, 14(4):25–38, 1974.
- [ONNK85] Masanobu Oda, Siavouche Nemat-Nasser, and Junichi Konishi. Stress-induced anisotropy in granular masses. *Soils and foundations*, 25(3):85–97, 1985.
- [Sha08] William N Sharpe. *Springer handbook of experimental solid mechanics*. Springer Science & Business Media, 2008.
- [SZS88] A Shukla, CY Zhu, and M Sadd. Angular dependence of dynamic load transfer due to explosive loading in granular aggregate chains. *The Journal of Strain Analysis for Engineering Design*, 23(3):121–127, 1988.
- [WJX<sup>+</sup>17] Li Wang, Yang Ju, Heping Xie, Guowei Ma, Lingtao Mao, and Kexin He. The mechanical and photoelastic properties of 3d printable stress-visualized materials. *Scientific reports*, 7(1):1–9, 2017.
- [WRD<sup>+</sup>18] Dong Wang, Jie Ren, Joshua A Dijksman, Hu Zheng, and Robert P Behringer. Microscopic origins of shear jamming for 2d frictional grains. *Physical review letters*, 120(20):208004, 2018.
- [ZWT<sup>+</sup>19] Hu Zheng, Dong Wang, Xinmeng Tong, Lihui Li, and Robert P Behringer. Granular scale responses in the shear band region. *Granular Matter*, 21(4):1–6, 2019.
- [ZZW<sup>+</sup>19] Yiqiu Zhao, Hu Zheng, Dong Wang, Meimei Wang, and Robert P Behringer. Particle scale force sensor based on intensity gradient method in granular photoelastic experiments. *New Journal of Physics*, 21(2):023009, 2019.





---

# Introduction to 3D Imaging for Experimental Geomechanics

**Edward Andò**

*EPFL Center for Imaging*

---

## 1 Introduction

This short introduction aims to introduce the concepts behind 3D imaging, and particularly distinguish 3D-surface imaging from 3D-volume imaging, the latter of which will be the focus for the 3D part of the course.

The previous sections have shown a tantalising glimpse of how much quantitative experimental information can be obtained with 2D imaging, in particular the measurement of shapes and sizes of particles, the fine measurement of displacements and thus strains, as well as body-forces with photoelasticity.

Although many things can be learned from a 2D simplification of experiments (such as Schneeblü materials) and simulations (2D DEM or 2D FEM), geotechnical engineering and experimental geomechanics always are concerned with three spatial dimensions. To this end 3D imaging offers the possibility of making much more pertinent quantitative measurements of material or site structure.

## 2 3D surface imaging

3D surface imaging is interested in the measurement of the opaque 3D surface of an object, without looking inside it. Although this is not the focus of the course, a few introductory notes are presented below. In essence, this is what the human visual system presents to our brain as our perception of the world – a mapping of objects and their distance. The data representation of such 3D information is typically a cloud of 3D points, a “point cloud”, which may have additional information attached to them (typically colour). A point cloud representing surfaces of objects in a scene can be measured with different methods:

- One of the main ways, continuing from the analogy with human vision is with multiple simultaneous photographs from different points of view of the same

object. These techniques are generally known under the moniker of “stereo-imaging”, which include techniques such as stereophotogrammetry and “Structure from Motion”. Possible modes are a binocular setup with two cameras, a drone taking several photos in a short time, or a plane flying over a scene. At the heart of all these techniques is the matching of the same points in different images, and the computation of the 3D position of the point from the geometry of the cameras, meaning that these techniques work best when there is a visible and unique “texture” in the captured images.

- Also using camera detection, a related technology is called “structure light” which projects a known pattern onto a scene, and observes this pattern from a camera, computing 3D positions of key elements of the pattern from a known calibration.
- Another popular technology measured distances based on the time required for light to travel to the object and back to the camera, rather than with the geometry of multiple cameras. These “Time of Flight” methods include LiDAR.

All methods, when used appropriately deliver a point cloud, which after appropriate denoising should look like the one presented below.

## 2.1 Point Cloud Example

Below is a point cloud coming from a one-minute flight with a consumer drone with an ordinary camera. Around 30 images were acquired flying around the house which is visible in the middle. The point cloud was reconstructed using a highly recommended open-source software called “MeshRoom” [GGC<sup>+</sup>21]

Only the images were fed into the software and the positions of the images were computed from the data, making this a very easy technique to use. Below is a pre-rendered 3D visualisation of the point cloud — note the higher density of points close to the house.

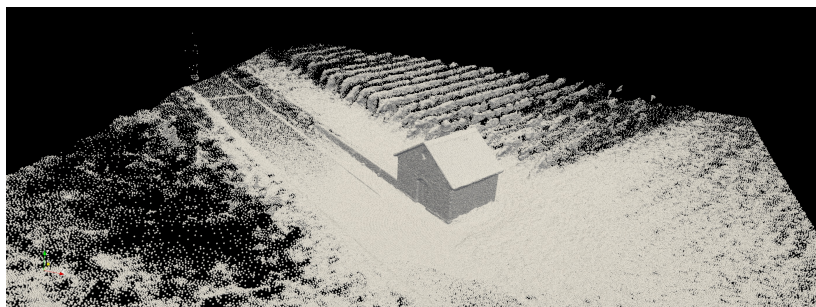


Figure 1: Point Cloud

## 2.2 Meshing a point cloud

Processing of the point cloud into a triangulated surface is not a trivial exercise, here the python open3D software is used [ZPK18] to make a Poisson surface reconstruction.

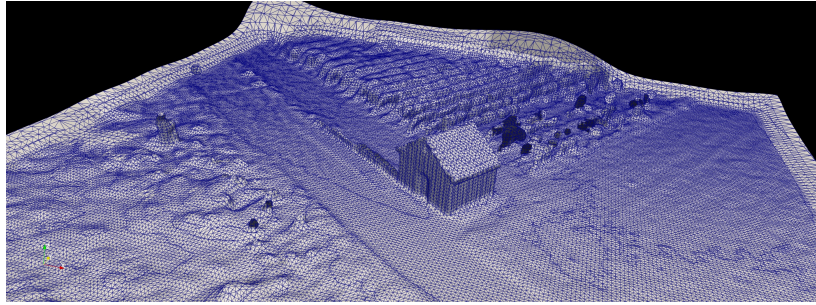


Figure 2: Surface Mesh

From such a mesh, surface areas can be computed, and surface levels of geotechnical sites can also be measured, for importing into FEA.

## 2.3 Surface Imaging for Experimental Mechanics

The example above shows 3D surface imaging at a scale of many meters. Although the focus of the rest of this 3D chapter will be on 3D volume imaging, it is important to note that 3D surface imaging techniques are very pervasive in experimental mechanics (although less so in geomechanics) as a routine tool to follow the deformation field happening during mechanical tests in the lab.

This is the slightly more sophisticated version of Digital Image Correlation discussed in the 2D section, sometimes known as 3D-DIC but probably more accurately known as stereo-DIC. In this technique the speckled surface of a deforming (concrete, metal, polymer) sample is observed with two cameras, thus the 3D motion of the surface can be tracked in time.

## 3 Volume Imaging

Now we will switch topics to 3D **volume** imaging: this means obtaining a 3D volume representing the 3D internal and external structure of a specimen. This is typically illustrated as a series of very thin slices through an object, but generally more mental clarity is obtained by thinking of such a measurement as a single 3D picture. Where 2D images **pixel** values are accessed with coordinates  $\vec{X} = (x, y)$ , 3D **voxels** are accessed with a third dimension  $\vec{X} = (x, y, z)$ .

This *full field* imaging modality is limited to laboratory experimental mechanics (although arguably some types of seismic monitoring and crust imaging also fall into the category of volume imaging).

From a 3D picture of the interior of a specimen, a very complete picture of a state can be made, up to the spatial resolution of the measurement. Taking the case of granular materials, if the resolution is higher than about 10 pixels per particle, there is good hope to be able to individually enumerate every single particle in a sample as a unique 3D entity allowing measurement/characterisation of position, size, and shape. Repeated 3D measurements allow the movement of particles, and evolution of their shape to be measured.

The next two sections will give a very brief introduction to Direct and Indirect 3D imaging.

### 3.1 Direct 3D imaging

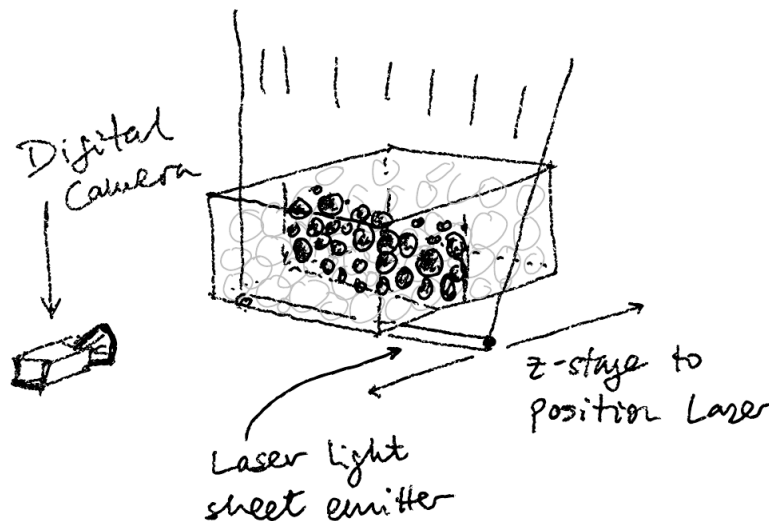


Figure 3: Sketch of RIMS

Here direct 3D imaging is intended in the sense that in these techniques the different thin 2D slices that make up the 3D volume are actually acquired directly. This is generally only possible in the case where the surrounding fluid and the object being scanned are both essentially transparent and their refractive indices are matched. The technique is therefore often known as RIMS (Refractive Index Matched Scanning) and has many similarities with Light-sheet Microscopy more often used in biology.

The trick here is to have a fluorescent fluid or solid phase that can be lit up with a laser

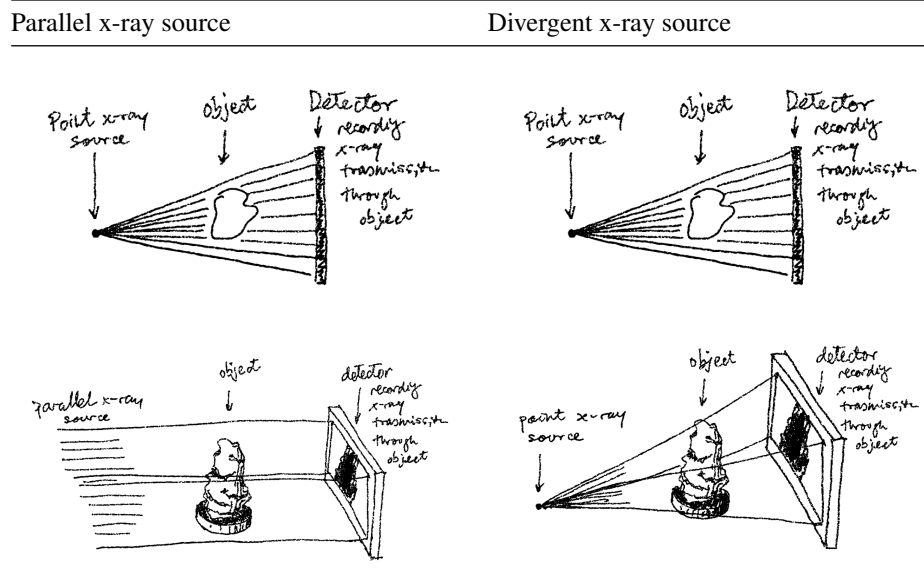
light sheet. The 3D image is therefore acquired by photographing different positions as the light sheet is scanned through the medium.

This is covered in detail in the section dedicated to this technique.

### 3.2 Indirect 3D imaging

The more general case for 3D imaging is with opaque materials, where RIMS is not applicable. This means that with regular light, only the outside surface of the object can be measured. The way out of this problem is to use penetrating radiation such as x-rays or Neutrons. It is worth mentioning that Magnetic Resonance Imaging (or Nuclear Magnetic Resonance) also belongs to the category of indirect 3D imaging, but the image is reconstructed according to different principles.

The indirectness of X-ray or neutron imaging comes from the fact that the radiation being used penetrates the sample, is partially absorbed and is then detected. This means that a single image represents an integration along the direction of the beam.



This will be covered in detail in the section dedicated to this technique

## References

- [GGC<sup>+</sup>21] Carsten Griwodz, Simone Gasparini, Lilian Calvet, Pierre Gurdjos, Fabien Castan, Benoit Maujean, Gregoire De Lillo, and Yann Lanthony. Alicevision meshroom: An open-source 3d reconstruction pipeline. In *Proceedings of the 12th ACM Multimedia Systems Conference*, pages 241–247, 2021.
- [ZPK18] Qian-Yi Zhou, Jaesik Park, and Vladlen Koltun. Open3d: A modern library for 3d data processing. *arXiv preprint arXiv:1801.09847*, 2018.

---

# Refractive Index Matched Scanning

**Joshua A. Dijksman**

*Wageningen University  
Physical Chemistry & Soft Matter*

---

## 1 Introduction

The fully three dimensional imaging and tracking of particles in a dense packing via optical methods presents a fundamental challenge: how to suppress light scattering at interfaces of different refractive index? Light scattering is necessary to both *illuminate* the sample properly inside the bulk, and to *observe* the sample without intractable image distortions. This challenge is especially pressing when more interfaces are present, such as in a dense packing of optically transparent particles. One way to solve that is via *index matching*: optical access to the bulk of the granular material is accomplished by immersing transparent particles in a fluid with the same index of refraction. This makes the resulting medium transparent. The bulk is then visualized by exciting, layer by layer, the fluorescent dye in the fluid phase, while capturing the resulting fluorescence as cross sections of the packing.

Refractive index matched scanning (RIMS) has become a popular experimental tool in recent years, although ordinary refractive index matched imaging has a long history: it has been applied to such diverse subjects as contrast variation scattering experiments with visible light, laser Doppler anemometry, blood flow anemometry, porous media flows, fluidized bed reactors and ground water hydrology [JDE75, HV80b, HV80a, AP88, PA90, MG95, EBE<sup>+</sup>99, PBN03, STG<sup>+</sup>08, ART09, FV02, HHCC08a]. In recent years index matching has been combined with particle image velocimetry [WAECA11] (PIV) and particle tracking velocimetry in two dimensions (2D PTV) for tracer particles [PBN03] and for the study of 3D flow fields [TVG03, SOK06]. These techniques have been reviewed elsewhere [HA82, YMLH94, Bud94, WAECA11].

Imaging and reconstructing the full three dimensional structure of granular packings and suspensions with an index matching technique was done already in the impressive pioneering work from Konagai *et al* [KTRM92] but not conveniently possible until about two decades ago, likely due to the technical challenges associated

with image recording and data handling; see for example Slotterback [STG<sup>+</sup>08] and Huang [HHCC08b]. Also tracking particle motion with RIMS has become possible, e.g. in the case of, three dimensional continuous [ZSG01, WDvH12, LS10, BDB15] and cyclic shear [AK10, PK10]. RIMS has been reviewed in the past [DRL<sup>+</sup>12, DBB17]; this introduction draws heavily from these, both in text and images, and summarizes these two works. We also add some more recent insights.

Refractive Index Matched Scanning (RIMS) works as follows: one submerses particles in a liquid with the same optical index. The dye, only present in the fluid or in the particles, is excited by a laser sheet — see Fig. 1a. The fluorescent light from the fluid can be detected with a camera, and a typical camera image will show the particles as dark spots in a bright, well defined cross section of the material (see Fig. 1b). When the particles contain a dye, they show up as bright spots in a dark background. The particles are visualized in three dimensions by moving the laser and simultaneously recording images to acquire image stacks, as shown in Fig. 1c. These three-dimensional image stacks are obtained for subsequent time steps, and image processing techniques can then be used to extract particle positions and trajectories. Fig. 1d shows typical examples of such trajectories [WDvH12].

The advantages of RIMS over the other three dimensional imaging methods discussed in this book can be easily provided: the single slice illumination technique allows one to image a full cross section within only one exposure time of a digital camera. The range of system sizes that RIMS can image is huge — this range is only limited from below by the diffraction limit and laser sheet thickness. The imaging speed is independent of the resolution, and set by the amount of fluorescent light available, reaching down to 10 ms per slice. Another advantage of the RIMS technique is that it is cheap compared to the other techniques mentioned. The technology required is a standard workstation, a laser sheet on a translation stage, and a digital camera, so costs are about 10-20 k\$. The drawbacks of RIMS are that the method can only work with optically transparent particles immersed in a fluid, which hugely restricts material choice and application areas. RIMS is therefore mostly used in granular model systems.

## 2 Index Matched Scanning Basics

A typical RIMS setup suitable for particle tracking uses particles with a diameter of typically  $\sim$  millimeter. Typical scan volumes measure 10-30 particles across, so the typical scan volume  $L^3$  is about a liter — see Fig. 2. The camera distance  $r$  is typically about 50 cm. The laser sheet is usually focussed on  $f \sim 30$  cm. The laser sheet thickness  $e$  should be less than a particle diameter  $d$ , and is typically a few hundred micron. Beam divergence in the laser sheet makes that the thickness of the sheet is not uniform; it is defined as the distance  $w$  over which the thickness does not vary more than  $\sqrt{2}$ , also referred to as the Rayleigh range — this is usually about a few centimeters.

These lengthscales indicate that RIMS is useful for imaging centimeter sized volumes,



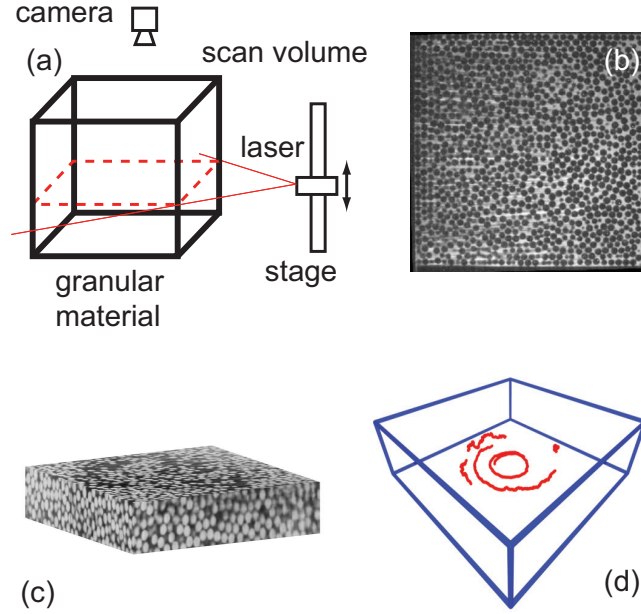


Figure 1: (a) A schematic overview of a RIMS setup, with all the essential components indicated. (b) A typical cross section of a suspension, obtained with RIMS. Particles (diameter 5 mm) appear as dark spots on a bright background. (c) A stack of cross sections. Colors are inverted for clarity. (d) From subsequent volume scans, one can obtain particle *traces*; a few examples are shown here in red/gray. The flow is driven from the bottom by a rotating disk, hence the circular trajectories. The stochastic motion of the particles is clearly visible.

in which particles of millimeter size are being tracked. For particles smaller than 10 micron, confocal microscopy is more suitable [THL07]. As we will discuss below, scan speeds of up to a volume per second can be reached. This limits flow speeds that can be imaged with RIMS to about one particle diameter per second.

The design of a RIMS setup confronts one with two main challenges: (i) how to achieve index matching, (ii) how to capture stacks of images? In the next two subsections we address both questions by reviewing the literature.

## 2.1 Materials considerations

To achieve index matching sufficient for RIMS, the difference in refractive indices of solid and liquid phase of the mixture needs to be less than  $\pm 2 \times 10^{-3}$  [DRL<sup>+</sup>12]. Over the years, several recipes for combinations of index matching fluids and particles have been found [Bud94, CA97, NYAK00, KBL96, SRJ03, YMLH94, MDM<sup>+</sup>06,

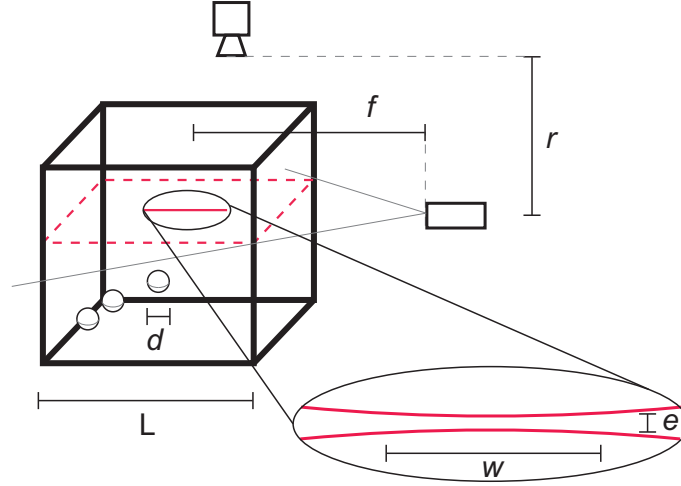


Figure 2: The lengthscales encountered in a RIMS setup. The scan volume size is  $L$ , the particle diameter is  $d$ , the laser sheet - camera distance is  $r$ . The focal point of the laser is at distance  $f$ , the sheet thickness is  $e$  and the beam divergence (see text) is  $w$ .

[HDO08](#), [WAECA11](#), [DRL<sup>+</sup>12](#), [DBB17](#)]. However, there is always some variation in the properties of commercially available products. Therefore some degree of tuning the recipes to the individual project always remains necessary.

## 2.2 Solids

Solids tend to have a higher index of refraction than liquids. There are several transparent solids we know of that have a low enough index of refraction to use them for index matching, that are also available commercially as spheres. Lists of available materials are available elsewhere [\[DRL<sup>+</sup>12\]](#). Broadly speaking, one can choose from soda lime glass, crystal glass (also known as lead glass), fused silica glass, borosilicate glass, the polymer poly(methyl metacrylate) (PMMA), also known as acrylic or plexiglas. The index of these materials ranges from 1.45 to 1.60 and is usually dependent on the manufacturer, except for standard glass types such as BK7, which has well defined properties. Hydrogel [\[DBB17, VWHF17\]](#) is different in character. This polymer gel can come in the form of  $\sim$  millimeter or centimeter sized spheres, for example from suppliers such as JRM Chemicals. It absorbs many times its own volume in water, thereby becoming large, soft and transparent, with an index of refraction comparable to that of water. Also Sephadex has been used as a soft particle for the study of mechanical properties of packings and suspensions [\[EL90\]](#), and its size ranges from 10-100s of micrometers.

The refractive indices for most materials specified are for reference only, as the index of refraction depends on temperature and wavelength (a phenomenon called *disper-*

sion) and is therefore customarily specified at the sodium D-lines at 589 nm, at 20 degrees Celsius; we will refer to it with  $n_D$  from now on. Typically dispersion is stronger for fluids than for solids. The exact dispersion relation depends on the material. For an overview of dispersion relations for typical RIM materials, consider Ref. [SRJ03, DRL<sup>+</sup>12] or <https://www.refractiveindex.info>.

*Optical homogeneity* of glass beads varies by type and manufacturer. Different batches of particles from the same source can have different refractive index with variations up to 0.01. Particles within one batch can have index variations as well. *Chemical compatibility* is also a concern; PMMA is a polymeric solid known to absorb water. We have found that it also absorbs Triton X-100 and Dimethyl sulfoxide (DMSO,  $(\text{CH}_3)_2\text{SO}$ ). Absorption of liquids changes the index of refraction of PMMA particles by as much [Ren02] as  $2.5 \times 10^{-3}$ . *Particle size* is limited by commercial availability; very monodisperse sets of particles with  $d < 500 \mu\text{m}$  are generally difficult to obtain, sieving a polydisperse set is then the only option. In the range  $d < 100 \mu\text{m}$  the situation however changes: certain chemical synthesis methods are able to produce very monodisperse particles of up to tens of microns, even at (affordable) bulk scale. Consider for example Microbeads or Cospheric. Monodisperse particles are easier to track, yet they have the tendency to crystallize [TG04] which may impede some experiments. Below 10 micrometer it becomes even easier to obtain well designed particles with even off-center fluorescent cores [YLTD21] but rigid shells, yet these are usually only available in limited quantities and display thermal motion, putting them beyond the scope of this review.

## 2.3 Liquids

For index matching of common solids, a liquid with an index of at least 1.45 is required. Several candidates for liquids have been found [Bud94, CA97, NYAK00, KBL96, SRJ03, YMLH94, MDM<sup>+</sup>06, HDO08, DRL<sup>+</sup>12]. To match the refractive index of hydrogel beads, one can use water with a polymer dissolved that is large enough to be unable to penetrate the hydrogel matrix, such as a large (100s of MW) polyvinylpyrrolidone (PVP) dissolved. Besides the refractive index, there are other physical and chemical properties to consider, which can be found in our review [DRL<sup>+</sup>12]. Tuning of the liquid to the solids used is an art in itself, and exhaustively discussed in existing reviews [DRL<sup>+</sup>12, DBB17].

## 2.4 Fluorescent dyes

When choosing a fluorescent dye, the peak in its absorption spectrum should be matched with the wavelength of the laser used. Besides this consideration and the price, there are other less obvious properties of laser dyes that are essential in RIMS applications. The *Stokes shift* is the difference between the absorbed and the emitted wavelength. This shift is measured between the peaks of the absorption and emission spectra of the dye. On the one hand, the shift is large enough so that the two spectra do not overlap. This allows for the filtering of scattered photons in the imaging with

cheaper optical components as described below. On the other hand, the Stokes shift should not be too large since index matching can only be tuned to one wavelength. Practically, a Stokes shift of more than 30 nm is not desirable [DRL<sup>+</sup>12].

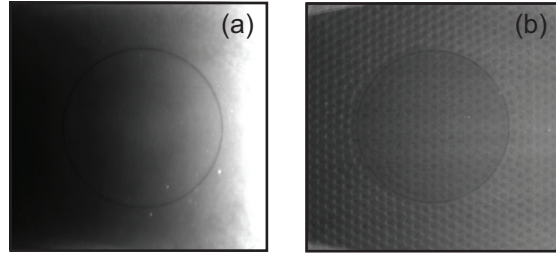


Figure 3: Top views of a cross section of a RIMS volume. The laser sheet shines from the right and intersects a layer in which only the dyed fluid is present. (a) With a high dye concentration, the gradient in the fluorescence is clearly visible. (b) Using a lower dye concentration, the contrast is decreased, and even deep in the box, far to the left, fluorescence is still observed.

The *emission spectrum* of the dye should be narrow for dispersion, and to cover the absorption spectrum of the light sensitive element used in the digital camera. Typically digital cameras have their maximum sensitivity around 500-600 nm. The *quantum yield* of the dye needs to be as high as possible, since absorption of photons increases the contrast gradient (see below). *Photobleaching* is the effect of the dye losing its capacity to fluoresce. This is a natural degradation process that is enhanced in the presence of (laser) light. For this reason most laser dyes have to be stored in a dark environment. The sensitivity to photobleaching depends on the type of dye. The *solvent* can adversely affect the absorption and emission spectrum of laser dyes. Nile Blue 690 Perchlorate is an example [KD04]: it turns pink in pure Triton, but when water or HCl are added to the solvent, it becomes dark blue as the dye interacts with the free protons available in these ingredients.

The amount of laser dye in the RIM liquid balances two effects: with more dye present, the fluorescence will be brighter so the contrast between the dark particles and the bright fluid will be more pronounced. Additionally, more fluorescence allows for shorter exposure times. On the other hand, the presence of the dye will prevent the laser light from penetrating deep into the measurement volume; typically  $I(x) \propto \exp(-\rho x)$ , where  $I(x)$  is the intensity of the laser light at distance  $x$  from the source, and  $\rho$  is the dye concentration – this is usually referred to as Bouguer-Lambert-Beer’s law as in X-ray attenuation. See Fig. 3 for an example of this effect. Note that the use of a laser line generator with a necessarily finite fan angle will naturally produce an intensity gradient  $I \sim A - Bx$  with  $A$  and  $B$  constants, due to the broadening of the laser line; the exponential drop in intensity due to the presence of the dye comes in addition to this effect. Thus, a higher dye concentration leads to particle-fluid contrast inhomogeneities in the imaging volume, which can make imaging impossible, or may affect tracking algorithms. Note that fluorescent dyes can also

be added to the particle. Commercially, fluorescent transparent particles are available, for example from Cospheric. One can also use acrylamide hydrogel particles in combination with laser dyes that are slightly hydrophobic. The hydrophobic groups on fluorescent molecules will make them favor absorption inside the hydrogel beads, where acrylamide also has hydrophobic domains. This effect depends sensitively on the choice of hydrogel; for example Sephadex will not display such dye absorption.

### 3 Instrument Design

Various engineering details of RIMS imaging setups affect their performance. We shall briefly highlight the role of setup size, imaging rates, video, illumination and optics, and mechanical components.

#### 3.1 Setup Dimensions

We had determined the typical size of a RIMS setup to be about a liter, with particles being about millimeter sized. These dimensions cannot be arbitrarily reduced or increased. What are the limiting factors? The wavelength of the laser light limits the thickness of the sheet and therefore the particle size. Laser lines that create a sheet thickness  $e$  of about  $15 \lambda$  within a workable focussing width  $w$  are commercially available.

The observable imaging volume is limited by the increasing scatter with increasing penetration depth. There is a maximum number of layers of particles  $l_s$  the laser sheet can traverse without scattering too much. Additionally, there is a maximum number of layers of particles  $l_f$  that the fluoresced photons can traverse to reach the camera.  $l_s$  and  $l_f$  cannot be both maximized simultaneously, since index matching must be done either at the wavelength of the laser or at the emission peak of the fluoresced photons. Typically one may assume  $l_s + l_f$  to be roughly constant. This total length can be  $> 30$  for good index matching [LS10, WAECA11, DRL<sup>+</sup>12].  $l_s + l_f$  itself can only be improved by better matching. However, this photon path length constraint can be geometrically relaxed by using two laser sources from opposing sides as discussed above, or by using two cameras imaging the volume from opposing sides.

#### 3.2 Imaging Rate

In designing a RIMS setup the deformation- or displacement rate one would like to image is a crucial parameter, since it sets the imaging rate. The required imaging rate sets the maximum stage speed, video system requirement, laser power, lens properties, et cetera. Identifying particles in subsequent frames is necessary to *trace* the trajectory of a single particle from frame to frame and to measure trajectories as shown in Fig. 1d. The amount of displacement per unit of time depends strongly on the type of experiment. Apart from the strain rate limitation, there are also other factors that favor faster scanning rates, such as evaporation of the liquid components, temperature drift, or dye bleaching. *Scan rate limitations* There are several experimental factors

that limit the maximum scan rate, among which stage inertia and laser stage design and camera exposure time.

### 3.3 Illumination, Optics & Video

Ideally the thickness of a laser sheet is less than a tenth of a particle diameter. It should have a uniform thickness throughout the scan volume. Modern sophisticated line generators can create such uniform laser sheets. However, beam divergence always limits the uniformity in flatness away from the focal point. Since the focal point is best placed in the center of the imaging volume (Fig. 2), it is helpful if the focus of the laser can be adjusted.

*Optics* Since the imaging rate is typically a concern, large aperture lenses are favorable for a RIMS setup. Direct (Reynolds) scatter of the photons from the laser beam creates intensity inhomogeneities in the captured images. To eliminate these scattered photons in the image, a filter can be used. Depending on the Stokes shift (see above) either a longpass filter [GRG10], or a band pass or notch filter, tuned to the laser wavelength, has to be used. Band passfilters are typically much more expensive.

*Video* Image capturing is turnkey nowadays - imaging at 10-1000 fps for long times is not an experimental challenge anymore. The efficiency of video recording does bring the challenge of data handling. Of course the bit depth of the camera used has to be good enough to be able to detect features in post processing, but also this constraint does not pose significant limitations anymore.

### 3.4 Mechanics

To scan different cross sections of the suspension it is necessary to move the laser sheet. The images have to stay in focus during the motion of the laser. There are two ways to achieve this: first, either the camera is placed at a large, fixed distance and optics is chosen such that the depth of field extends over the whole range of laser sheet position. Second, for faster scanning, another solution is more favorable. For higher frame rates one needs as much light as possible and since the dye in the fluid fluoresces photons in random directions the camera should be close to the sheet. Moreover, a large aperture lens is typically used, since they capture more light.

Regardless of this choice, the total optical path length between the sheet and the camera sensor changes with the distance the light travels through the optically denser liquid. The camera and the laser sheet therefore have to be moved by different amounts. The added complexity of dual laser/camera motion is however inhibitive; a proper choice of  $f$  and aperture can keep the depth of field large enough to relax this constraint. The small distortion in calibration in the images that then remains can be corrected for in postprocessing.

### 3.5 Distortion compensation in 3D

The first step in image postprocessing is to ensure the camera system presents no optical distortion. This is the case with cheap lenses, or by using a zoom lens at suboptimal settings. In order to estimate the distortion field of the camera system, one can use the checkerboard method with implementation taken from OpenCV [Bra08, Bra00]. Images of the checkerboard in multiple 3D orientations are taken in order to estimate both the 3D projection model from the camera to the real world, together with the lens distortion parameters. In practice, little distortion is usually observed. The second step is to compensate for varying optical path lengths. This can be done by measuring the position of each corner of the hydrogel container, in the image for each depth. One then tags the positions of these corners in selected images at various depths, building a list of  $(r, c, 1)$  triplets for each corner (standing respectively for row, column, and a constant for homogeneous coordinates). Each of these triplets ideally corresponds to known coordinates  $(x, y, z, 1)$  in the container referencial. A least-squared error fit is then needed [Lou04] to estimate the  $3 \times 4$  projection matrix  $M$  such that

$$\left\| \alpha \begin{bmatrix} r_1 & r_2 & \dots & r_n \\ c_1 & c_2 & \dots & c_n \\ 1 & 1 & \dots & 1 \end{bmatrix} - M \begin{bmatrix} x_1 & x_2 & \dots & x_n \\ y_1 & y_2 & \dots & y_n \\ z_1 & z_2 & \dots & z_n \\ 1 & 1 & \dots & 1 \end{bmatrix} \right\|^2$$

is minimal, where  $n$  is the number of observations and  $\alpha$  is a free coefficient for the homogeneous transform. This method implicitly handles the rotation of the image so that the bottom of the tank appears horizontal. For each image, a robust sub-pixel position of the corners is obtained from the projection. These positions are then used to rescale and stack images into 3D. The net result is a properly scaled three dimensional image based on the (noisy) image slices. The next step is to denoise this 3D image volume.

An easier method is used below in the example post processing section, in which the front and back of the 3D volume are manually measured and then rescaled with an interpolation method.



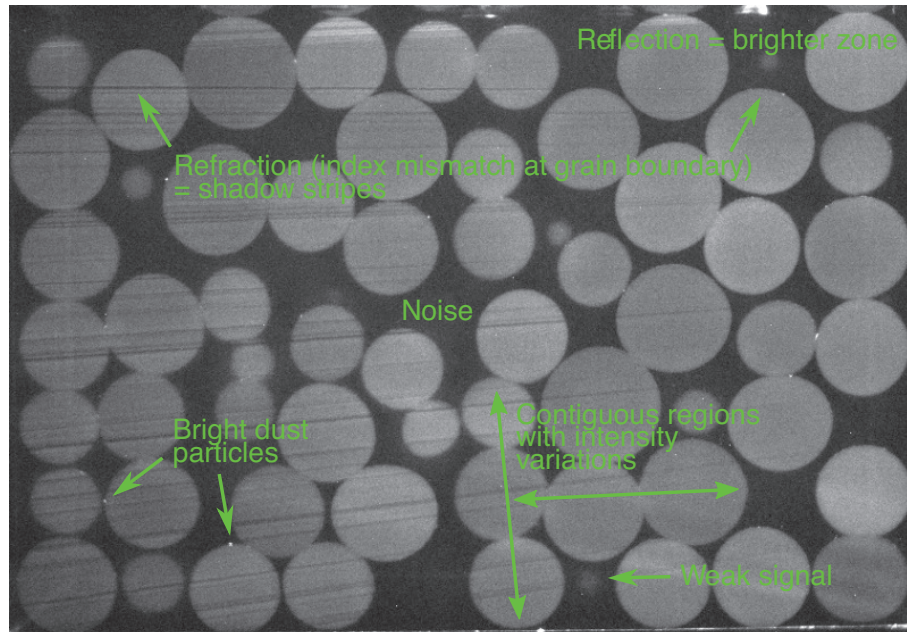


Figure 4: Raw image with major sources of artifacts that needs to be processed.



### 3.6 Image Denoising

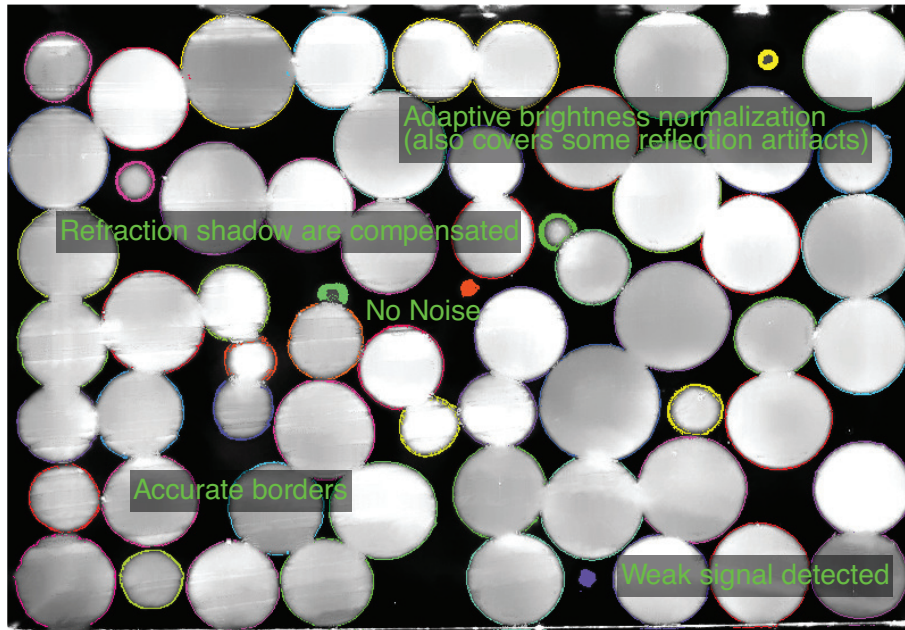


Figure 5: Processed image after artefact removal.

There are several types of noise in the slice images (shown in Fig.4), that are specific to RIMS. They can be dealt with separately (see Fig.5). *Dust from particles* and turbidity or leftover dye in water generates noise with unknown characteristics, so NL-Means filtering [BCM11] can be used to adequately remove it. This step can in fact be performed on the raw images, before stacking them in 3D.

*Refraction shadows:* These are due to a slight index mismatch, especially at the interface between grains. In the laser sheet plane, the grain cross-section appears as a disk. The deflection on each side of the grain surface produces a dark zone, starting tangentially to the disk, opposite the direction of the laser source. The solution to remove these can be as described in [DBB17].

*Reflection shadows* and laser light absorption can be solved with a local grey-level renormalization, often called histogram normalization. More examples of imaging artefacts can be seen in Fig. 6

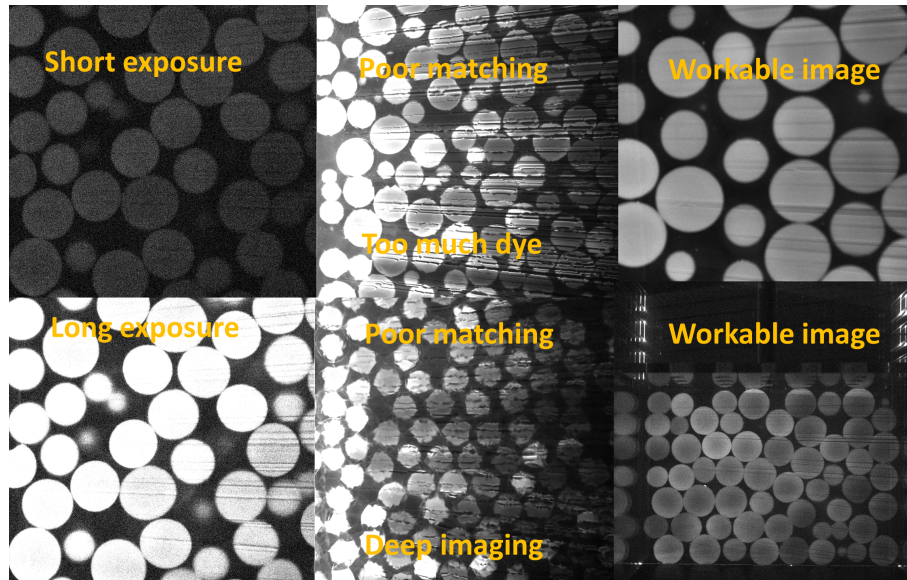


Figure 6: More examples of image artefacts. From left to right: too long and too short exposure times; Insufficient index matching at the front and back of the imaging volume; workable images in close up and full image.

### 3.7 Routines for postprocessing RIMS images

After obtaining an image as shown in Fig. 1c, particle positions can be obtained by (a combination of) common image processing techniques such as thresholding, convolution, pattern matching, morphological operations etc. Sub-pixel approximation can improve most tracking techniques to  $\pm 0.1$  pixel; algorithms are discussed in Ref. [OE10, CG96, BIWP09]. If applicable well developed routines such as the ones by Grier, Crocker and Weeks [DWP<sup>+</sup>01, CG96] can be used, which are nowadays also available in Python.

## 4 Sample Code

Below you can find a sample set of code that illustrates the process of using RIMS on a set of images to perform a reconstruction.

```
import PIL.Image
import numpy
import scipy.ndimage
import glob
import matplotlib.pyplot as plt
import spam.DIC
import spam.deformation
```

```
# Let's scan the ScanRef folder and get a sorted list of the
  ↳JPG files
files = sorted(glob.glob("./path/to/files/*.jpg"))

# Read one JPG file to get 2D dimensions (x and y)
im = numpy.array(PIL.Image.open(files[0]))

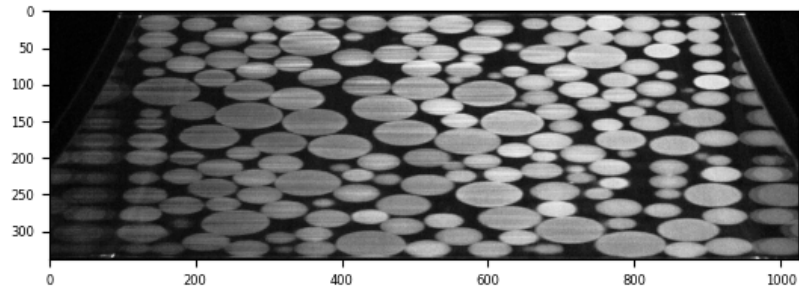
# Allocate an empty 3D matrix, (x, y) and number of files (z)
im3D = numpy.zeros((len(files), im.shape[0], im.shape[1]))

# For every JPG file in the list, load it and copy the
  ↳greyscale values into our empty 3D array
for i, file in enumerate(files):
    im3D[i] = numpy.array(PIL.Image.open(files[i]))
```

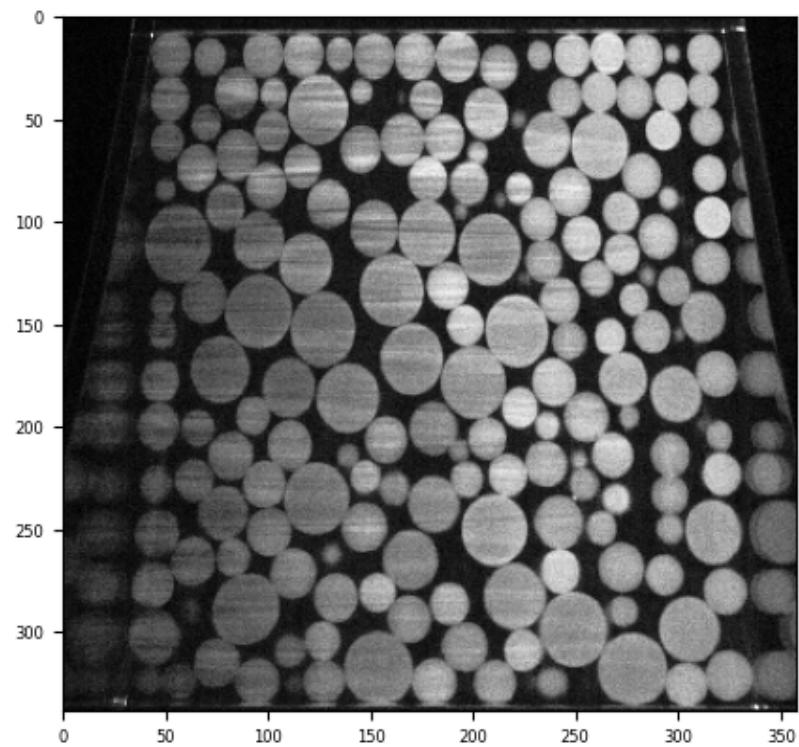
```
# This is now a 3D volume saved in (z, y, x) coordinates.
# Let's cut down the middle of the y-axis and show this image.
plt.imshow(im3D[:,im3D.shape[1]//2], cmap='Greys_r');
plt.show()

# It's clear that the size of pixels is not isotropic -- let's
  ↳stretch the image in the z-direction
# to try to roughly even it out, by scaling x and y down by a
  ↳factor of 0.35.
im3Diso = scipy.ndimage.zoom(im3D, [1, 0.35, 0.35])
print(im3Diso.shape)
plt.imshow(im3Diso[:,im3Diso.shape[1]//2], cmap='Greys_r');
plt.show()
```

## 96 Refractive Index Matched Scanning



(339, 358, 358)



**Please note: stretching looks OK, but it's fatter at the bottom**

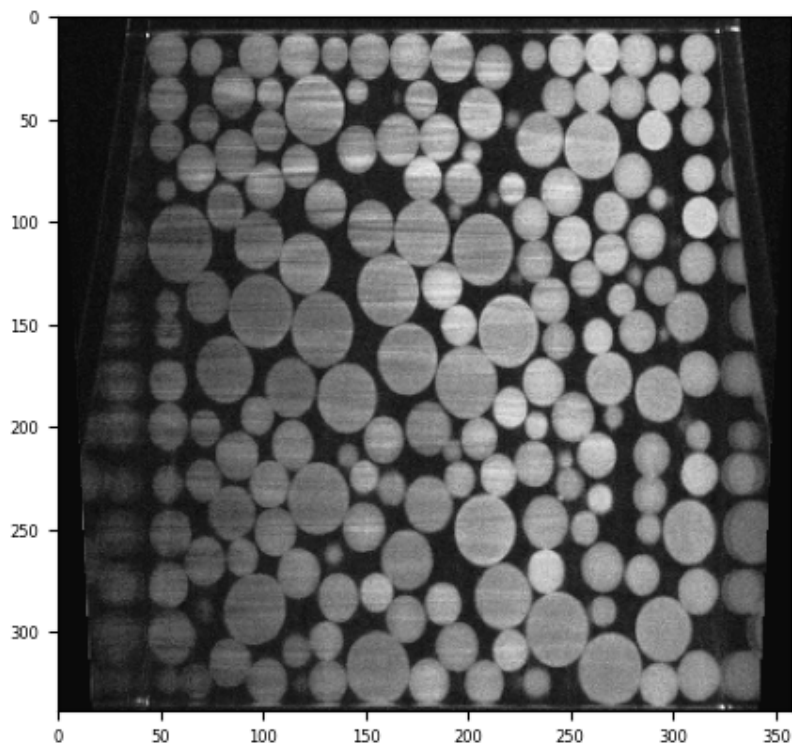
widths on this slice (measured by eye): - W=882 at the Z=end - W=802 at the Z=beginning

#### 4.1 Let's apply a increasing un-zoom as we go down Z

```
# Let's progressively unzoom the image, here we're making a
# ↪ correction factor for each Z-slice
# This is very rough, and should ideally be combined with the
# ↪ 0.35 scaling step above.
zoom = numpy.linspace(1, 1*(802/882), 339)

# Make a new empty 3D array, which we'll fill applying the
# ↪ zoom correction to each slice
im3DisoDC = numpy.zeros_like(im3Diso)
for z in range(im3Diso.shape[0]):
    im3DisoDC[z] = spam.DIC.applyPhiPython(im3Diso[z][numpy.
    ↪ newaxis, ...], spam.deformation.computePhi({'z': [1,
    ↪ zoom[z], zoom[z]]}))

# Show this new image, it is straighter?
plt.imshow(im3DisoDC[:,im3DisoDC.shape[1]//2], cmap='Greys_r');
plt.show()
```



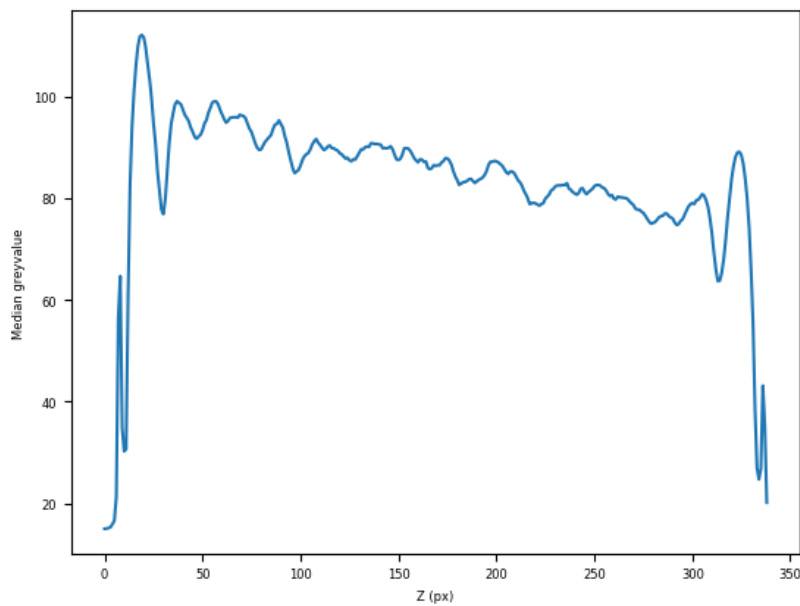
## 4.2 Greyscale homogeneity

Now we can try to correct the fact that the greyscale values are slightly fading as Z increases. We'll try to measure this by computing the median value of greylevels throughout Z with a crop.

The median will give a relatively well-denoise value for the particles, on condition that the volume fraction of particles is  $> 0.5$

Let's just plot the greylevel evolution down the z-axis:

```
plt.plot(numpy.median(im3DisoDC[:, 90:300, 50:-50],
    ↪axis=(1,2)));
plt.xlabel('Z (px)')
plt.ylabel('Median greyvalue')
plt.show()
```



## 4.3 Eye fitting!

Let's just very roughly fit a line to this data by eye (this could be easily automated)

- Value = 100 at  $z=0$
- Value = 75 at  $z=338$

We'll use this line to "correct" (i.e., increase) the greylevels in the higher-Z slices)

```

correction = numpy.zeros(im3Diso.shape[0])
for z in range(im3DisoDC.shape[0]):
    c = 100 / (100 - (25 / (339 / (z + 1))))
    correction[z] = c
    #print(f"Correction = {c}")

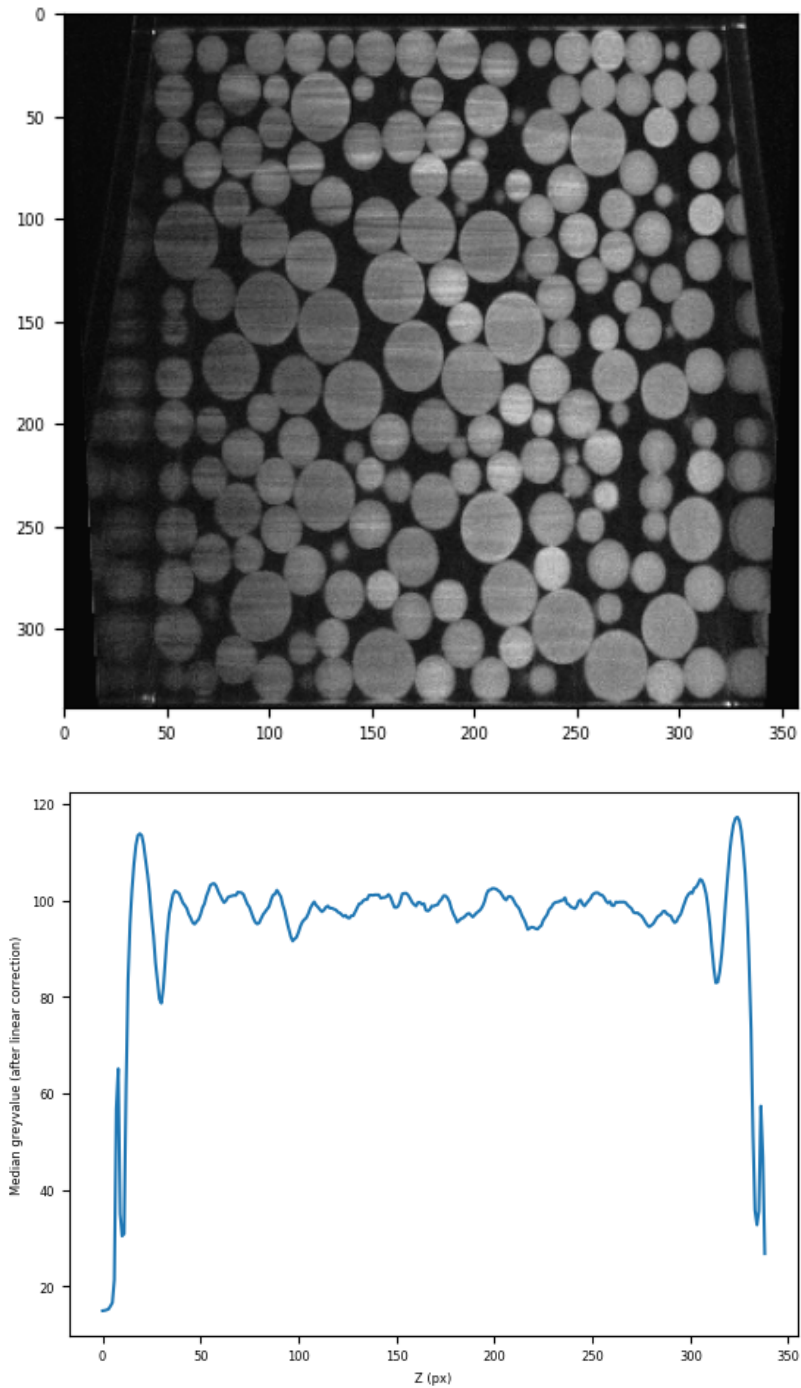
#print(correction)
#plt.plot(correction * numpy.median(im3DisoDC[:, 90:300, 50:
    ↪ -50], axis=(1, 2)));
plt.show()

# Apply correction to im3Diso:
im3DisoDC_GC = numpy.zeros_like(im3DisoDC)
for z in range(im3DisoDC.shape[0]):
    im3DisoDC_GC[z] = im3DisoDC[z] * correction[z]
plt.imshow(im3DisoDC_GC[:, im3DisoDC_GC.shape[1] // 2],
    ↪ cmap='Greys_r');
plt.show()

# So now it's flat?
plt.plot(numpy.median(im3DisoDC_GC[:, 90:300, 50:-50],
    ↪ axis=(1, 2)));
plt.xlabel('Z (px)')
plt.ylabel('Median greyvalue (after linear correction)')
plt.show()

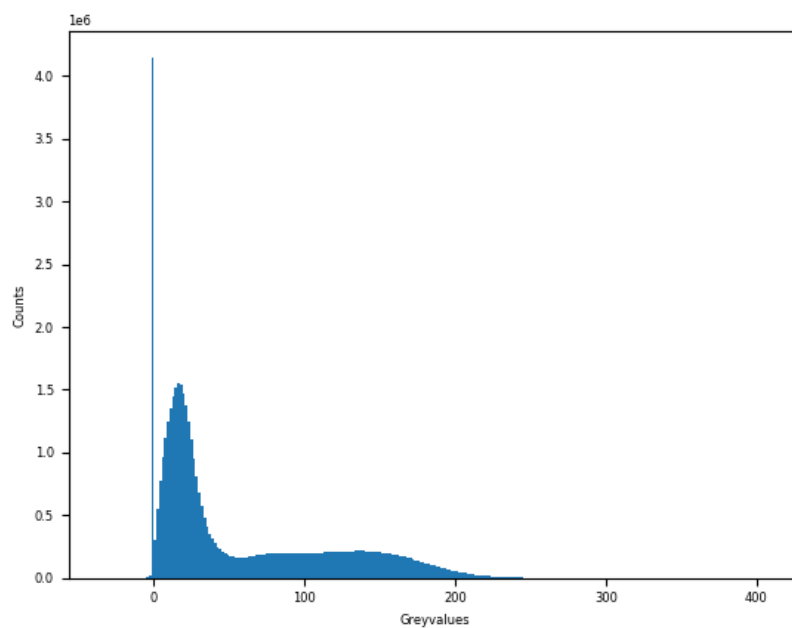
```

## 100 Refractive Index Matched Scanning

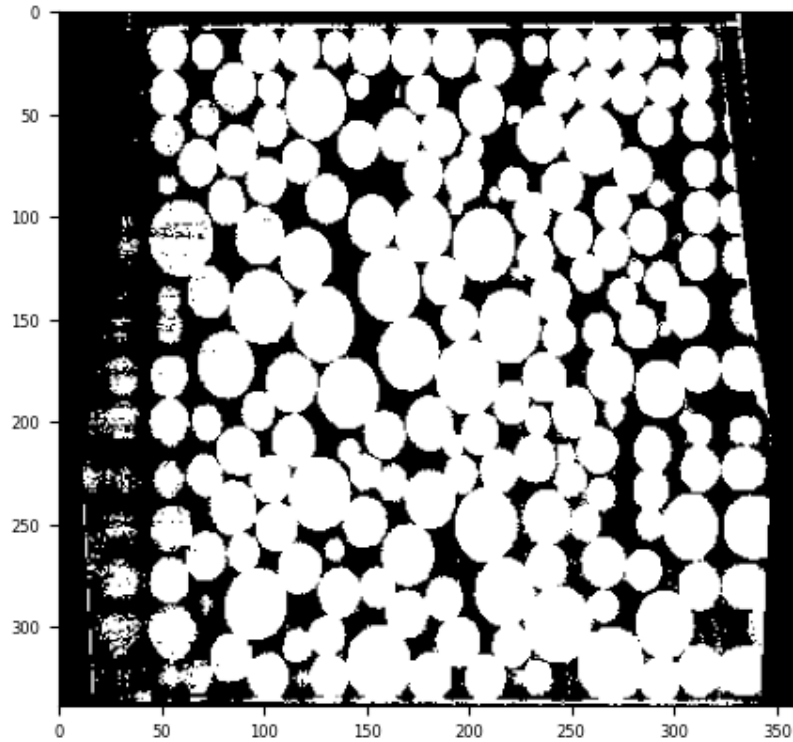




```
# After these greylevel corrections, let's look at the
    ↳ histogram of greyvalues.
# hopefully there will be two well-separated greyvalue peaks:
    ↳ the background and the particles
plt.hist(im3DisoDC_GC.ravel(), bins=256)
plt.xlabel('Greyvalues')
plt.ylabel('Counts')
plt.show()
```



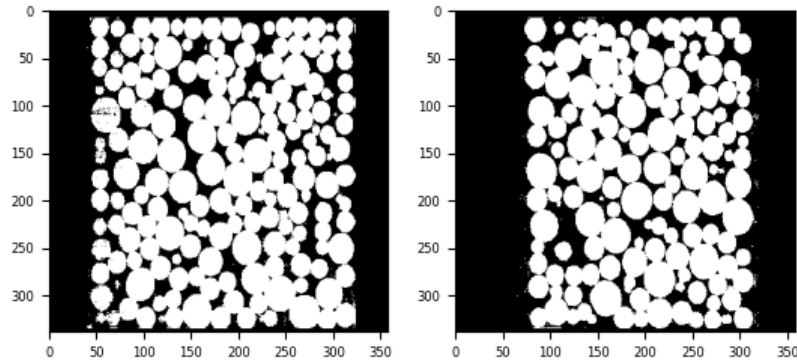
```
# A threshold value of 50 looks reasonable, let's apply it:
T = 50
plt.imshow(im3DisoDC_GC[:,im3Diso.shape[1]//2] > T,
    ↳ cmap='Greys_r');
plt.show()
```



```
# Let's now crop the outsides of the box...
im3DisoDC_GC_binary = im3DisoDC_GC.copy() > T
im3DisoDC_GC_binary[0:9] = 0
im3DisoDC_GC_binary[-3::] = 0

im3DisoDC_GC_binary[:, :, 0:40] = 0
im3DisoDC_GC_binary[:, :, 323::] = 0
plt.subplot(1,2,1)
plt.imshow(im3DisoDC_GC_binary[:,im3Diso.shape[1]//2],  
           cmap='Greys_r');

im3DisoDC_GC_binary[:, 0:60] = 0
im3DisoDC_GC_binary[:, 320::] = 0
plt.subplot(1,2,2)
plt.imshow(im3DisoDC_GC_binary[:,im3Diso.shape[2]//2],  
           cmap='Greys_r');
plt.show()
```



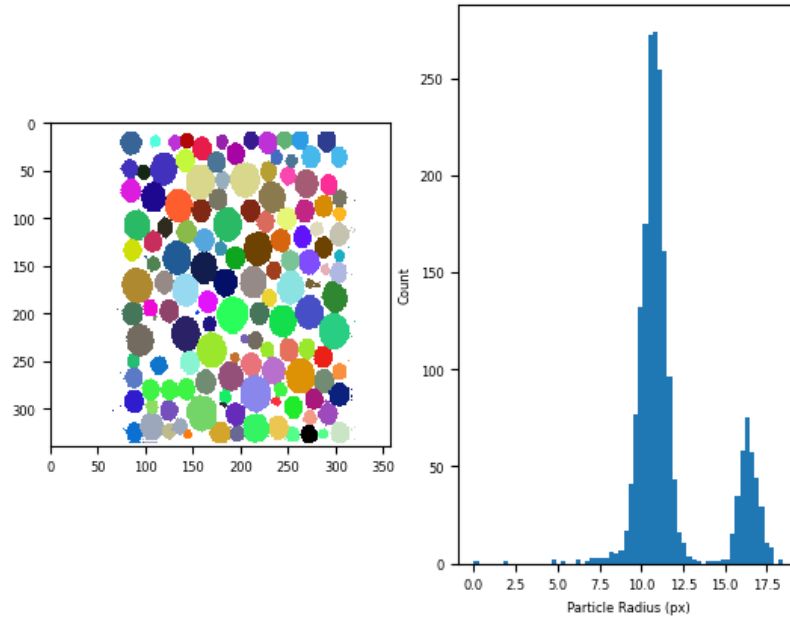
```
# We can now try to separate all touching particles with a
↳ standard 3D watershed:
import spam.label
lab = spam.label.watershed(im3DisoDC_GC_binary)

print(f"There are {lab.max()} particles")
plt.subplot(1,2,1)
plt.imshow(lab[:, :, im3Diso.shape[2]//2],
           cmap=spam.label.randomCmap,
           interpolation='none')

# Compute the radius of the sphere of the same volume as each
↳ particle
particleRadii = spam.label.equivalentRadii(lab)

plt.subplot(1,2,2)
plt.hist(particleRadii, bins=64)
plt.xlabel("Particle Radius (px)")
plt.ylabel("Count")
plt.show()
```

There are 1954 particles

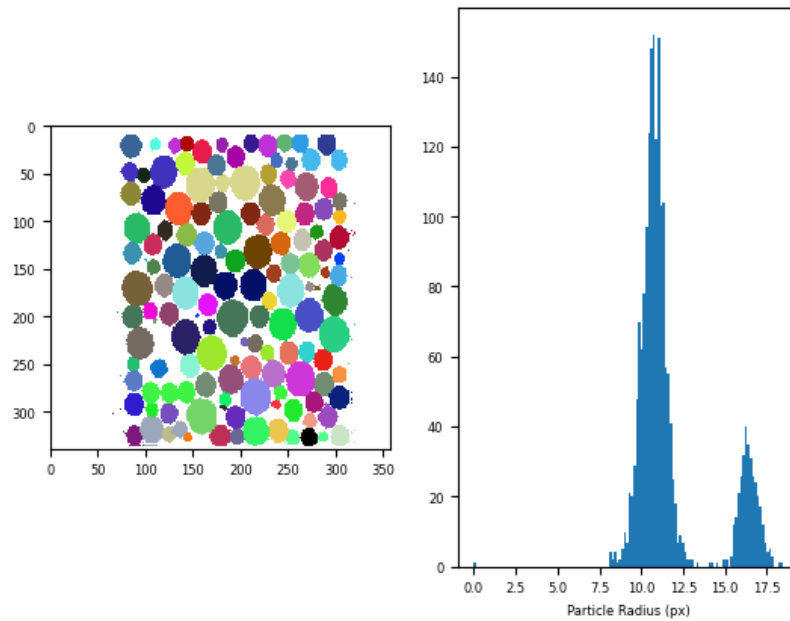


```
# Tidy up too-small particles
lab = spam.label.removeLabels(lab, numpy.where(particleRadii < 8))
lab = spam.label.makeLabelsSequential(lab)

# Recompute radii
particleRadii = spam.label.equivalentRadii(lab)

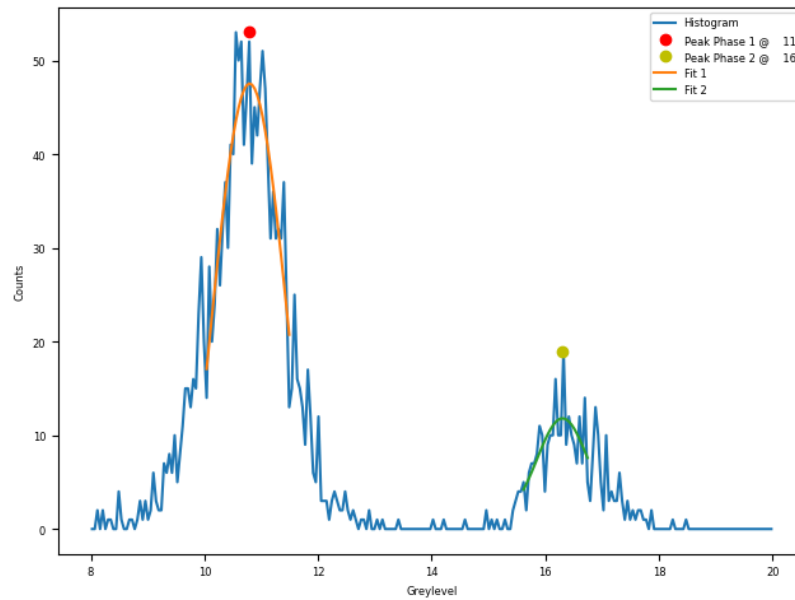
plt.subplot(1,2,1)
plt.imshow(lab[:, :, im3Diso.shape[2]//2],
           cmap=spam.label.randomCmap,
           interpolation='none')

plt.subplot(1,2,2)
plt.hist(particleRadii, bins=128)
plt.xlabel("Particle Radius (px)")
plt.show()
```



```
import spam.helpers
spam.helpers.findHistogramPeaks(particleRadii,
                                valley1=14,
                                gaussianFit=True,
                                showGraph=True,
                                greyRange=[8,20])
```

## 106 Refractive Index Matched Scanning

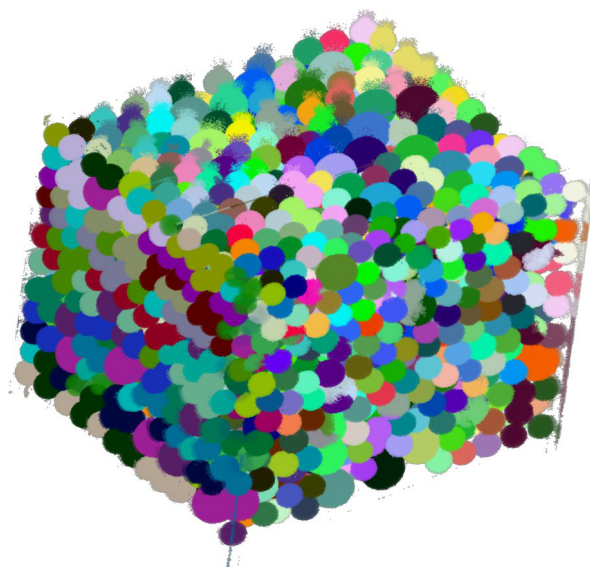


```
array([10.796, 16.302])
```

```
#import tiff file
#tiff file imwrite("lab.tif", lab)

# 3D rendering in your favourite programme...

PIL.Image.open("../im/3Drendering.jpg")
```



Volume Viewer

## References

- [AK10] A. Panaitescu and A. Kudrolli. Experimental investigation of cyclically sheared granular particles with direct particle tracking. *Prog. Theor. Phys. Suppl.*, 184:100, 2010.
- [AP88] Bruce J. Ackerson and P. N. Pusey. Shear-induced order in suspensions of hard spheres. *Phys. Rev. Lett.*, 61(8):1033–1036, Aug 1988.
- [ART09] James K. Arthur, Douglas W. Ruth, and Mark F. Tachie. Piv measurements of flow through a model porous medium with varying boundary conditions. *J. Fluid Mech.*, 629:343–374, JUN 25 2009.
- [BCM11] Antoni Buades, Bartomeu Coll, and Jean-Michel Morel. Non-Local Means Denoising. *Image Processing On Line*, 1, 2011. [https://doi.org/10.5201/ipol.2011.bcm\\_nlm](https://doi.org/10.5201/ipol.2011.bcm_nlm).
- [BDB15] Nicolas Brodu, Joshua A Dijksman, and Robert P Behringer. Spanning the scales of granular materials through microscopic force imaging. *Nature communications*, 6(1):1–6, 2015.
- [BIWP09] R. Besseling, L. Isa, E. R. Weeks, and W. C.K. Poon. Quantitative imaging of colloidal flows. *Adv. Coll. Interf. Sci.*, 146(1-2):1 – 17, 2009.
- [Bra00] G. Bradski. *Dr. Dobb’s Journal of Software Tools*, 2000.
- [Bra08] G. Bradski. *Dr. dobb’s journal of software tools*, 2008.
- [Bud94] R Budwig. Refractive-Index Matching Methods For Liquid Flow Investigations. *Exp. Fluids*, 17(5):350–355, September 1994.
- [CA97] M.M. Cui and R.J. Adrian. Refractive index matching and marking methods for highly concentrated solid-liquid flows. *Exp. Fluids*, 22(3):261–264, JAN 1997.
- [CG96] John C. Crocker and David G. Grier. Methods of digital video microscopy for colloidal studies. *Journal of Colloid and Interface Science*, 179(1):298 – 310, 1996.
- [DBB17] Joshua A Dijksman, Nicolas Brodu, and Robert P Behringer. Refractive index matched scanning and detection of soft particles. *Review of Scientific Instruments*, 88(5):051807, 2017.
- [DRL<sup>+</sup>12] Joshua A Dijksman, Frank Rietz, Kinga A Lőrincz, Martin van Hecke, and Wolfgang Losert. Invited article: Refractive index matched scanning of dense granular materials. *Review of Scientific Instruments*, 83(1):011301, 2012.
- [DWP<sup>+</sup>01] A. D. Dinsmore, Eric R. Weeks, Vikram Prasad, Andrew C. Levitt, and D. A. Weitz. Three-dimensional confocal microscopy of colloids. *Appl. Opt.*, 40(24):4152–4159, 2001.



- [EBE<sup>+</sup>99] C.J. Egelhoff, R.S. Budwig, D.F. Elger, T.A. Khraishi, and K.H. Johansen. Model studies of the flow in abdominal aortic aneurysms during resting and exercise conditions. *Journ. Biomech.*, 32(12):1319–1329, December 1999.
- [EL90] Ian D Evans and Alexander Lips. Concentration dependence of the linear elastic behaviour of model microgel dispersions. *Journal of the Chemical Society, Faraday Transactions*, 86(20):3413–3417, 1990.
- [FV02] Mirrya M. Fontenot and R. Dennis Vigil. Pore-scale study of nonaqueous phase liquid dissolution in porous media using laser-induced fluorescence. *J. Coll. Interf. Science*, 247(2):481 – 489, 2002.
- [GRG10] Jeffrey S. Guasto, Andrew S. Ross, and J. P. Gollub. Hydrodynamic irreversibility in particle suspensions with nonuniform strain. *Phys. Rev. E*, 81(6):061401, Jun 2010.
- [HA82] F. Hendriks and A. Aviram. Use of zinc iodide solutions in flow research. *Rev. Sci. Instr.*, 53(1):75–78, 1982. Publisher: AIP.
- [HDO08] Yassin A. Hassan and E. E. Dominguez-Ontiveros. Flow visualization in a pebble bed reactor experiment using piv and refractive index matching techniques. *Nucl. Eng. Design*, 238(11):3080–3085, NOV 2008.
- [HHCC08a] Alice Huang, Michelle Huang, Herve Capart, and Rong-Her Chen. Optical measurements of pore geometry and fluid velocity in a bed of irregularly packed spheres. *Exp. Fluids*, 45(2):309–321, 2008. Publisher: Springer Berlin / Heidelberg.
- [HHCC08b] Alice Huang, Michelle Huang, Herve Capart, and Rong-Her Chen. Optical measurements of pore geometry and fluid velocity in a bed of irregularly packed spheres. *Exp. Fluids*, 45:309–321, 2008.
- [HV80a] A. K. Van Helden and A. Vrij. Contrast variation in light scattering: Silica spheres dispersed in apolar solvent mixtures. *J. Coll. Interf. Science*, 76(2):418 – 433, 1980.
- [HV80b] A. K. Van Helden and A. Vrij. Static light scattering of concentrated silica dispersions in apolar solvents. *J. Coll. Interf. Science*, 78(2):312 – 329, 1980.
- [JDE75] William Johnston, Alexander Dybbs, and Robert Edwards. Measurement of fluid velocity inside porous media with a laser anemometer. *Phys. Fluids*, 18(7):913–914, 1975.
- [KBL96] G. P. Krishnan, S. Beimfohr, and D. T. Leighton. Shear-induced radial segregation in bidisperse suspensions. *J. Fluid Mech.*, 321(-1):371–393, 1996.

- [KD04] H. S. Patel K. Das, B. Jain. Nile blue in triton-x 100/benzene-hexane reverse micelles: a fluorescence spectroscopic study. *Spectroch. Acta Part A*, 60:2059–2064, 2004.
- [KTRM92] Kazuo KONAGAI, Choshiro TAMURA, Peter RANGELOW, and Takashi MATSUSHIMA. Laser-aided tomography: A tool for visualization of changes in the fabric of granular assemblage. *Doboku Gakkai Ronbunshu*, 1992(455):25–33, 1992.
- [Lou04] M.I.A. Lourakis. levmar: Levenberg-marquardt non-linear least squares algorithms in C/C++. [web page] <http://www.ics.forth.gr/~lourakis/levmar/>, Jul. 2004. [Accessed on 31 Jan. 2005.].
- [LS10] K.A. Lőrincz and P. Schall. Visualization of displacement fields in a sheared granular system. *Soft Matt.*, 6:3044–3049, 2010.
- [MDM<sup>+</sup>06] P. Miller, K. Danielson, G. Moody, A. Slifka, E. Drexler, and J. Hertzberg. Matching index of refraction using a diethyl phthalate/ethanol solution for in vitro cardiovascular models. *Exp. Fluids*, 41:375–381, 2006.
- [MG95] C.D. Montemagno and W.G. Gray. Photoluminescent Volumetric Imaging - A Technique For The Exploration Of Multiphase Flow And Transport In Porous-Media. *Geophys. Res. Lett.*, 22(4):425–428, February 1995.
- [NYAK00] T.L. Narrow, M. Yoda, and S.I. Abdel-Khalik. A simple model for the refractive index of sodium iodide aqueous solutions. *Exp. Fluids*, 28(3):282–283, MAR 2000.
- [OE10] J. Olafsen (Ed.). *Experimental and Computational Techniques in Soft Condensed Matter Physics*. 2010.
- [PA90] SE Paulin and Bruce J Ackerson. Observation of a phase transition in the sedimentation velocity of hard spheres. *Physical review letters*, 64(22):2663, 1990.
- [PBN03] O. Pouliquen, M. Belzons, and M. Nicolas. Fluctuating particle motion during shear induced granular compaction. *Phys. Rev. Lett.*, 91(1):014301, July 2003. Publisher: American Physical Society.
- [PK10] Andreea Panaitescu and Arshad Kudrolli. Spatial distribution functions of random packed granular spheres obtained by direct particle imaging. *Phys. Rev. E*, 81(6):060301, Jun 2010.
- [Ren02] Y. Ren. Efficiency shifts of prism coupling into polymer waveguides subject to environmental variations. *Opt. Mater.*, 19:443–447, 2002.
- [SOK06] S. Siavoshi, A. V. Orpe, and A. Kudrolli. Friction of a slider on a granular layer: Nonmonotonic thickness dependence and effect of bound-

- ary conditions. *Phys. Rev. E*, 73(1):010301, January 2006. Publisher: American Physical Society.
- [SRJ03] M. Stohr, K. Roth, and B. Jahne. Measurement of 3d pore-scale flow in index-matched porous media. *Exp. Fluids*, 35(2):159–166, AUG 2003.
- [STG<sup>+</sup>08] S. Slotterback, M. Toiya, L. Goff, J. F. Douglas, and W. Losert. Correlation between particle motion and voronoi-cell-shape fluctuations during the compaction of granular matter. *Phys. Rev. Lett.*, 101(25):258001, 2008. Publisher: APS.
- [TG04] J.-C. Tsai and J. P. Gollub. Slowly sheared dense granular flows: Crystallization and nonunique final states. *Phys. Rev. E*, 70(3):031303, Sep 2004.
- [THL07] Masahiro Toiya, Jacco Hettinga, and Wolfgang Losert. 3d imaging of particle motion during penetrometer testing. *Gran. Matt.*, 9:323–329, 2007.
- [TVG03] J-C Tsai, Greg A Voth, and Jerry P Gollub. Internal granular dynamics, shear-induced crystallization, and compaction steps. *Phys. Rev. Lett.*, 91(6):064301, 2003. Publisher: APS.
- [VWHF17] Daniel Von Wangenheim, Robert Hauschild, and Jiří Friml. Light sheet fluorescence microscopy of plant roots growing on the surface of a gel. *JoVE (Journal of Visualized Experiments)*, (119):e55044, 2017.
- [WAECA11] Sébastien Wiederseiner, Nicolas Andreini, Gaël Epely-Chauvin, and Christophe Ancey. Refractive-index and density matching in concentrated particle suspensions: a review. *Experiments in Fluids*, 50(5):1183–1206, 2011.
- [WDvH12] E. Wandersman, J. Dijksman, and M. van Hecke. Particle diffusion in slow granular bulk flows. *Eur. Phys. Lett.*, 2012.
- [YLTD21] Taiki Yanagishima, Yanyan Liu, Hajime Tanaka, and Roel PA Du-lens. Particle-level visualization of hydrodynamic and frictional couplings in dense suspensions of spherical colloids. *Physical Review X*, 11(2):021056, 2021.
- [YMLH94] B Yip, M.F. Miller, A. Lozano, and R.K. Hanson. a combined oh/acetone planar laser-induced fluorescence imaging technique for visualizing combusting flows. *Exp. Fluids*, 17(5):330–336, September 1994.
- [ZSG01] K. B. Zitoun, S. K. Sastry, and Y. Guezennec. Investigation of three dimensional interstitial velocity, solids motion, and orientation in solid-liquid flow using particle tracking velocimetry. *Int. J. Multiphase Flow*, 27(8):1397 – 1414, 2001.



---

## 3D imaging of opaque materials

**Edward Andò**

*EPFL Center for Imaging*

---

### 1 3D imaging of opaque materials with tomography

As justified in the introduction to this section, in the case of experimental geomechanics, a non-destructive 3D picture of a sample being tested — especially one at the pertinent internal scales (of the most important inclusions, pores, particles) can reveal a lot about the structure of the material.

Furthermore, leveraging the non-destructiveness of x-ray tomography, multiple different states can be imaged resulting in a time series of 3D images, sometimes known as a 3D+t or 4D dataset (time being one of the dimensions).

Unlike the case of RIMS described above, in an opaque (to visible light) material, it is not possible to directly illuminate and image a 2D slice within the material, thus obtaining the 3D image by correcting and stitching the acquired images. The “trick” to making a 3D image is to make an image using something other than visible light, typically higher-energy light (in the form of x-rays or gamma rays) but Neutrons can also work. X-rays photons are higher energy than visible light photons and (also) have quite complex interaction with matter. What is leveraged for volumetric imaging is the fact that relatively high-energy x-rays are not easily stopped by matter — the intensity of light (in photons/second) can be reduced (“attenuated”) but some x-ray light will shine through centrimetric-sized objects with minimum deviation.

#### 1.1 From Beer-Lambert Law to Radiograph

The law that dictates how x-ray intensity varies with the thickness of the object being traversed is the famous Beer-Lambert Law. The initial x-ray intensity  $I_0$  is reduced to an “output” intensity  $I$  (expected to be  $\leq I_0$ ):

$$I = I_0 \exp^{-\mu x}$$

where  $x$  is the path length and  $\mu$  is an attenuation coefficient (which in this case hides a lot of complexity, notably a dependence on density, but also on x-ray energy).

Looking at the equation, when the path length is zero then  $I = I_0$ , and for fixed  $\mu$ , as  $x$  increases,  $I$  reduces exponentially.

The attenuation coefficient for x-rays tends to follow the atomic number and therefore roughly the density of the material. In the appendix of [Grünauer, F. (2005). Design, optimisation, and implementation of the new neutron radiography facility at FRM-II (Doctoral dissertation, Technische Universität München)] an extremely convenient periodic table is found showing the difference between neutron and x-ray attenuation (for a fixed energy) — note the progressive increase of x-ray attenuation from top to bottom.

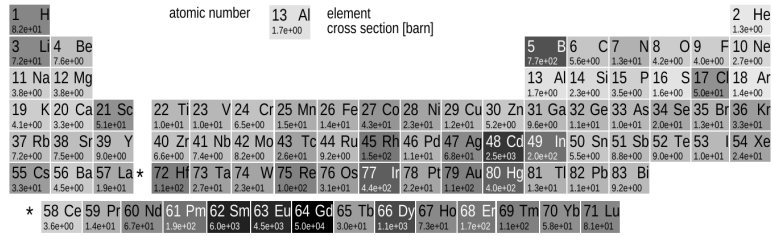


Fig. A.64: Total microscopic cross section  $\sigma$  [barn] for neutrons with an energy of 25 meV [94]. The displayed gray value is proportional to  $\log_{10}(\sigma)$ .

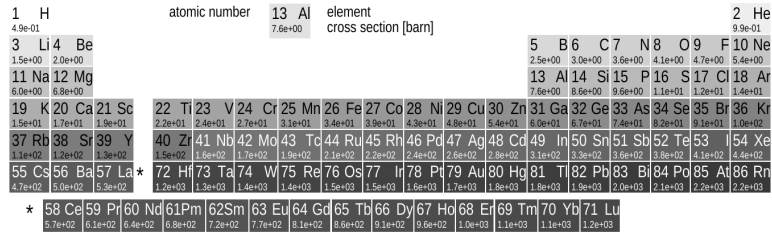


Fig. A.65: Total microscopic cross section  $\sigma$  [barn] for photons with an energy of 100 keV [8]. The displayed gray value is proportional to  $\log_{10}(\sigma)$ .

Figure 1: Cross sections

In the case of x-ray imaging, we now know that we will be interested in x-rays that travel straight through the specimen, and that denser materials will attenuate more x-rays. The figure below shows a very simple system that allows a 1D x-ray image of an object to be acquired. A parallel x-ray beam is generated on the left, the beam travels through the object (and is partially attenuated). The attenuated beam is then measured on a detector on the right. Normally the procedure is to measure the x-ray intensity without the object in place ( $I_0$ , also known as a “flat-field”) and compare it to the x-ray intensity measured with the object in place ( $I$ ).

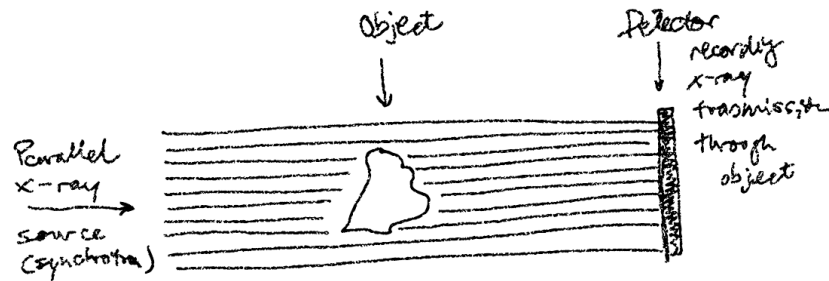


Figure 2: 2D illustration of parallel x-ray beam.

What is measured using the detector is the x-ray *transmission* through the object, it goes without saying that x-rays absorbed by the object are not detected. If the detector is composed of a series of individual pixels (a so-called “line detector”), the resulting measurement is a vector of numerical values representing x-ray intensity. Although a lot of line detectors are used in industry (but also research), the most common form of x-ray detector for imaging is a flat-panel detector, meaning that what is measured is a 2D matrix of values:

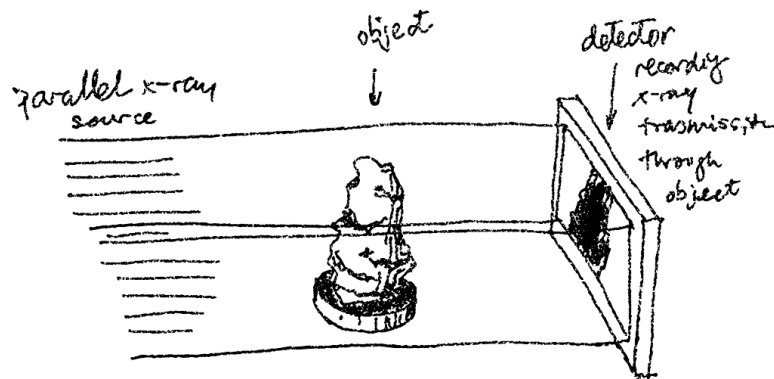


Figure 3: Configuration of parallel x-ray imaging in 3D.

Such a 2D image representing the attenuation of the sample is called a radiograph. Since bones attenuate significantly more than the surrounding flesh, this is a key tool for the medical investigation of broken bones.

Note that in the particular case of medical imaging, dark values represent high transmission. Taking this into account, one can see that the bone indeed attenuates much

more than the surrounding flesh, and some internal structures are visible.

## 1.2 Radiograph to Projection to Reconstruction

Such a radiograph allows a number of things to be understood — it is a view *through* an object. Indeed this was used to great effect in Roscoe’s 1970 work [Ros70] to track lead shot (highly attenuating) deep within a geotechnical experiment.

However, this imaging modality is highly dependent on the orientation of the object being scanned. With the explicit aim of building up a 3D picture of the object, it is useful to think about a radiograph as an image resulting from *the summing of the attenuation along each beam path*. Said differently, the radiograph is a flattened picture of the object *projected* in the direction of the beam. In the context of “reconstructing” a 3D picture of the object, a radiograph is often referred to as a *projection*.

The objective thus is to try to make an unflattened picture of the object: the trick here will be to measure projections at different angles and try to compute the 3D object that could have created these projections: this is *par excellence* an inverse problem. The function that we’re trying to inverse is the **Radon transform**.

For the sake of illustration, we will use the following parallel, 2D imaging geometry (discussed above):

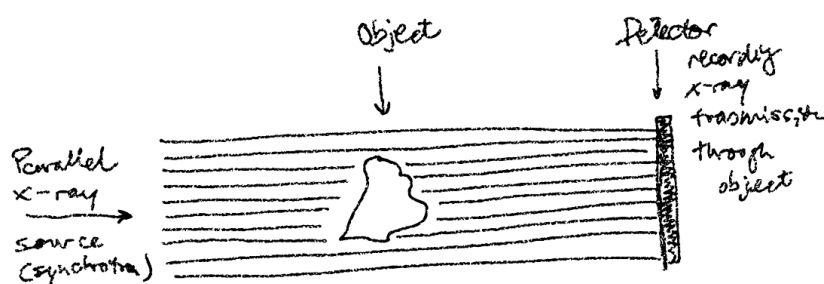


Figure 4: 2D illustration of a parallel x-ray beam, object, and detector.

In this case therefore, the objective will simply be to “reconstruct” the 2D slice of the object — if this is successful, the process can be repeated for all other horizontal rows on the detector.

The rest of the notebook is based on the radon transform notebook from scikit-image: [[VdWSNI+14] [https://scikit-image.org/docs/stable/auto\\_examples/transform/plot\\_radon\\_transform.html](https://scikit-image.org/docs/stable/auto_examples/transform/plot_radon_transform.html)



### 1.3 Computing a single projection at a given angle

We will start from the slice we're trying to measure as a basis, this is taken from previously reconstructed data — it's a 2D slice through a cylinder containing grains. The first step will be to simulate a projection of this field in a single direction — this is the only thing that we're able to measure. Feel free to vandalise the loaded image with some very high pixel to see where they end up in two projections at 0 and 90°. What we are doing here is a “forward projection” of the known 2D field into a 1D signal.

```
import numpy
import tifffile
import matplotlib.pyplot as plt

from skimage.data import shepp_logan_phantom
from skimage.transform import radon, rescale

image = tifffile.imread("M2EA05-01-bin4-s200-zeroed.tif").
    ↳astype(float)
print(f"Loaded image dimensions: {image.shape}")
#image[10:15, 100:115] = 400000

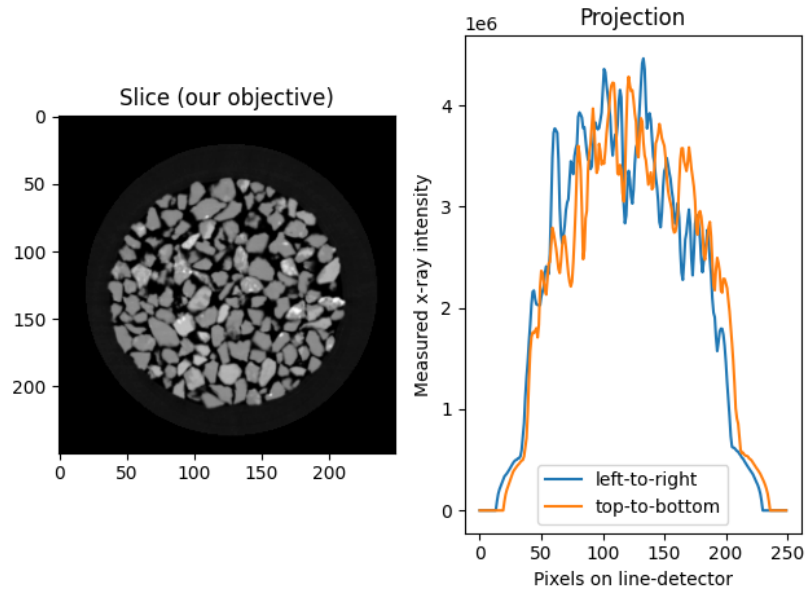
plt.subplot(1, 2, 1)
plt.title("Slice (our objective)")
plt.imshow(image, cmap=plt.cm.Greys_r)

plt.subplot(1, 2, 2)
plt.title("Projection")
#print(radon(image, theta=numpy.array([90])))

plt.plot(radon(image, theta=numpy.array([90])),
    ↳label='left-to-right')
plt.plot(radon(image, theta=numpy.array([0])),
    ↳label='top-to-bottom')
plt.ylabel("Measured x-ray intensity")
plt.xlabel("Pixels on line-detector")
plt.legend()

plt.tight_layout()
plt.show()
```

Loaded image dimensions: (250, 250)



```
import scipy.ndimage

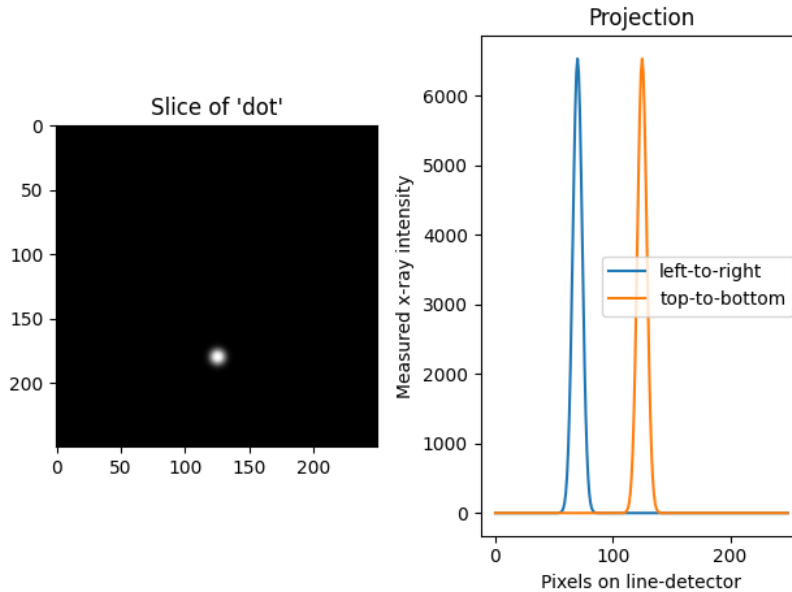
imageDot = numpy.zeros_like(image)
imageDot[180, 125] = 65535
imageDot = scipy.ndimage.gaussian_filter(imageDot, 4)

plt.subplot(1, 2, 1)
plt.title("Slice of 'dot'")
plt.imshow(imageDot, cmap=plt.cm.Greys_r)

plt.subplot(1, 2, 2)
plt.title("Projection")
# print(radon(image, theta=numpy.array([90])))

plt.plot(radon(imageDot, theta=numpy.array([90])),
         label='left-to-right')
plt.plot(radon(imageDot, theta=numpy.array([0])),
         label='top-to-bottom')
plt.ylabel("Measured x-ray intensity")
plt.xlabel("Pixels on line-detector")
plt.legend()

plt.tight_layout()
plt.show()
```



## 1.4 Computing a sinogram

The two different projections above might be sufficient to get an idea of a very simple object such as a square aligned with the image, but in the general two views are not sufficient. What needs to be acquired is a large number of different projections — in the case of filtered back projection, the Nyquist-Shannon sampling theorem gives us:

$P \geq \frac{\pi}{2} S$  — with  $P$  being the number of projections and  $S$  roughly the number of pixels along one side of the reconstructed slice. [Kha13]

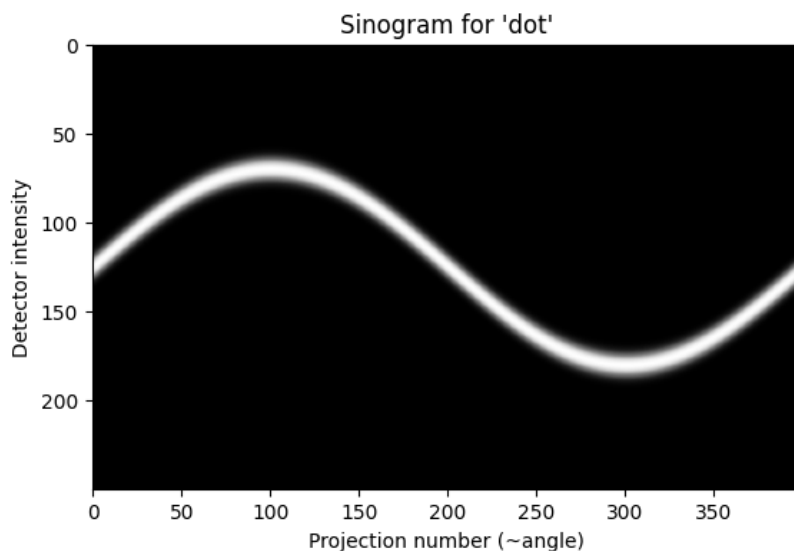
Let's try to “acquire” this many different projection angles on our fake data above, as it rotates around  $360^\circ$ . The slice is  $250 \times 250$  pixels meaning  $P$  should be more than 392, let's call it 400 different angles. Instead of producing 392 different 1D plots as above, we will define a new way to look at the data, a **sinogram**.

As seen above our simulated linear detector has 250 pixels, so we will define a new “image” of size 250 (pixels) by 400 different angles; this is a sinogram (the reason will become apparent in a second), and is the default input to a reconstruction algorithm. For every projection angle (like the two simulated above), the resulting 250 “measurements” will be written into one line of the sinogram.

```
theta = numpy.linspace(0., 360., 400, endpoint=False)
sinogramDot = radon(imageDot, theta=theta)

plt.imshow(sinogramDot, cmap="Greys_r")
plt.title("Sinogram for 'dot'")
```

```
plt.ylabel("Detector intensity")
plt.xlabel("Projection number (~angle)")
plt.show()
```



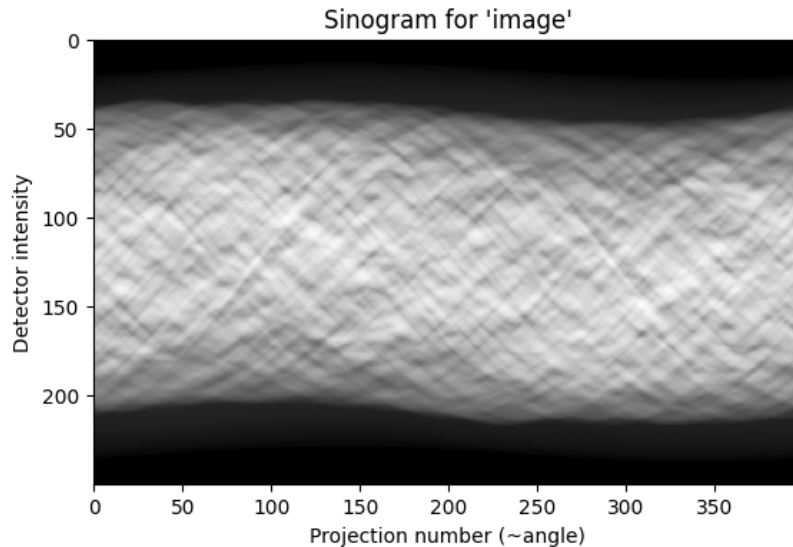
The dot of `imageDot` clearly describes a sinusoid. In the case of a parallel beam, there is only need to spread the angles to acquire through  $180^\circ$  instead of  $360^\circ$ , but this is not the general case with a divergent (cone, or in 2D, fan) beam.

Play around with `imageDot` (add more dots, perhaps one in the centre) and see the effect in the sinogram. You'll see that the further an object is from the center of rotation, the larger the amplitude of the sine wave.

Going back to the much more complex grains data, here is the corresponding sinogram:

```
theta = numpy.linspace(0., 360., 400, endpoint=False)
sinogram = radon(image, theta=theta)

plt.imshow(sinogram, cmap="Greys_r")
plt.title("Sinogram for 'image'")
plt.ylabel("Detector intensity")
plt.xlabel("Projection number (~angle)")
plt.show()
```



### 1.5 Reconstruction with the Filtered Back Projection (FBP)

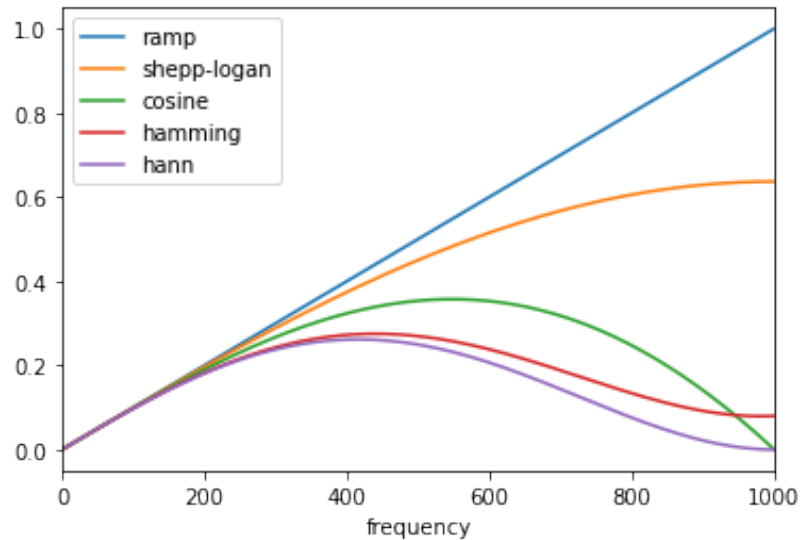
The mathematical foundation of the filtered back projection is the Fourier slice theorem. It uses Fourier transform of the projection and interpolation in Fourier space to obtain the 2D Fourier transform of the image, which is then inverted to form the reconstructed image. The filtered back projection is among the fastest methods of performing the inverse Radon transform. The only tunable parameter for the FBP is the filter, which is applied to the Fourier transformed projections. It may be used to suppress high frequency noise in the reconstruction. `skimage` provides the filters 'ramp', 'shepp-logan', 'cosine', 'hamming', and 'hann':

```
import matplotlib.pyplot as plt
from skimage.transform.radon_transform import _get_fourier_filter

filters = ['ramp', 'shepp-logan', 'cosine', 'hamming', 'hann']

for ix, f in enumerate(filters):
    response = _get_fourier_filter(2000, f)
    plt.plot(response, label=f)

plt.xlim([0, 1000])
plt.xlabel('frequency')
plt.legend()
plt.show()
```



Applying the inverse radon transformation with the 'ramp' filter, we get:

```
from skimage.transform import iradon

reconstruction_fbp = iradon(sinogram, theta=theta,
    filter_name='ramp')
error = reconstruction_fbp - image
print(f'FBP rms reconstruction error: {numpy.sqrt(numpy.
    mean(error**2)):.3g}')

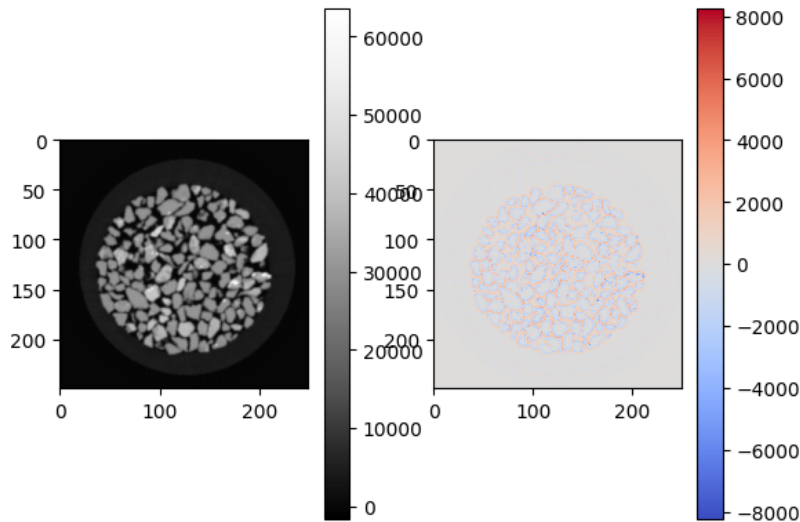
maxError = numpy.max(numpy.abs(error))
imkwargs = dict(vmin=-maxError, vmax=maxError)

plt.subplot(1,2,1)
plt.imshow(reconstruction_fbp, cmap='Greys_r')
plt.colorbar()

plt.subplot(1,2,2)
plt.imshow(error, cmap='coolwarm', **imkwargs)
plt.colorbar()

plt.show()
```

FBP rms reconstruction error: 1.06e+03



## 1.6 Reconstruction with the Simultaneous Algebraic Reconstruction Technique

Algebraic reconstruction techniques for tomography are based on a straightforward idea: for a pixelated image the value of a single ray in a particular projection is simply a sum of all the pixels the ray passes through on its way through the object. This is a way of expressing the forward Radon transform. The inverse Radon transform can then be formulated as a (large) set of linear equations. As each ray passes through a small fraction of the pixels in the image, this set of equations is sparse, allowing iterative solvers for sparse linear systems to tackle the system of equations. One iterative method has been particularly popular, namely Kaczmarz' method, which has the property that the solution will approach a least-squares solution of the equation set.

The combination of the formulation of the reconstruction problem as a set of linear equations and an iterative solver makes algebraic techniques relatively flexible, hence some forms of prior knowledge can be incorporated with relative ease.

`skimage` provides one of the more popular variations of the algebraic reconstruction techniques: the Simultaneous Algebraic Reconstruction Technique (SART). It uses Kaczmarz' method as the iterative solver. A good reconstruction is normally obtained in a single iteration, making the method computationally effective. Running one or more extra iterations will normally improve the reconstruction of sharp, high frequency features and reduce the mean squared error at the expense of increased high frequency noise (the user will need to decide on what number of iterations is best suited to the problem at hand). The implementation in `skimage` allows prior information of the form of a lower and upper threshold on the reconstructed values to be supplied to the reconstruction.

```

from skimage.transform import iradon_sart

reconstruction_sart = iradon_sart(sinogram, theta=theta)
error = reconstruction_sart - image
print(f'SART (1 iteration) rms reconstruction error: '
      f'{numpy.sqrt(numpy.mean(error**2)):.3g}')

fig, axes = plt.subplots(2, 2, figsize=(8, 8.5), sharex=True,
                        ↳sharey=True)
ax = axes.ravel()

ax[0].set_title("Reconstruction\nSART")
ax[0].imshow(reconstruction_sart, cmap=plt.cm.Greys_r)

ax[1].set_title("Reconstruction error\nSART")
ax[1].imshow(reconstruction_sart - image, cmap=plt.cm.
            ↳coolwarm, **imkwargs)

# Run a second iteration of SART by supplying the
↳reconstruction
# from the first iteration as an initial estimate
reconstruction_sart2 = iradon_sart(sinogram, theta=theta,
                                  image=reconstruction_sart)
error = reconstruction_sart2 - image
print(f'SART (2 iterations) rms reconstruction error: '
      f'{numpy.sqrt(numpy.mean(error**2)):.3g}')

ax[2].set_title("Reconstruction\nSART, 2 iterations")
ax[2].imshow(reconstruction_sart2, cmap=plt.cm.Greys_r)

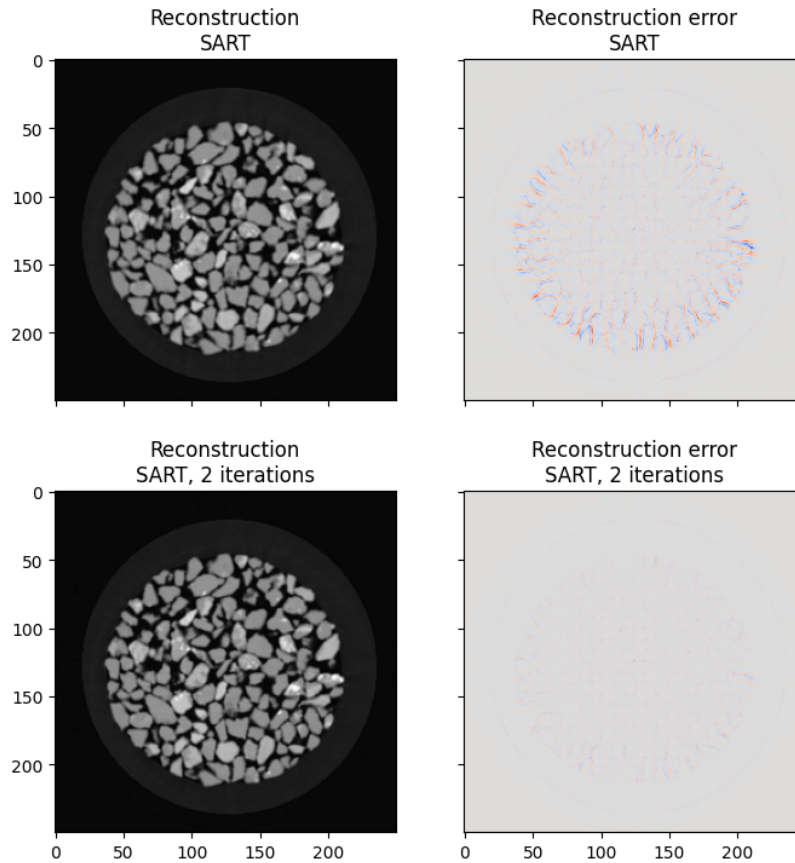
ax[3].set_title("Reconstruction error\nSART, 2 iterations")
ax[3].imshow(reconstruction_sart2 - image, cmap=plt.cm.
            ↳coolwarm, **imkwargs)
plt.show()

```

SART (1 iteration) rms reconstruction error: 738

SART (2 iterations) rms reconstruction error: 448





## 1.7 Reconstructing all the slices

Returning back to 3D with a parallel beam (as pictured below) the line detector example developed above now corresponds to a horizontal row of pixels on the detector. Each row can be reconstructed separately, and thus a series of horizontal cross-sections can be recovered. Stacking them all together will yield a 3D image with slices as thick as the pixel size (in this case the pixel size of the detector if there's no magnification).

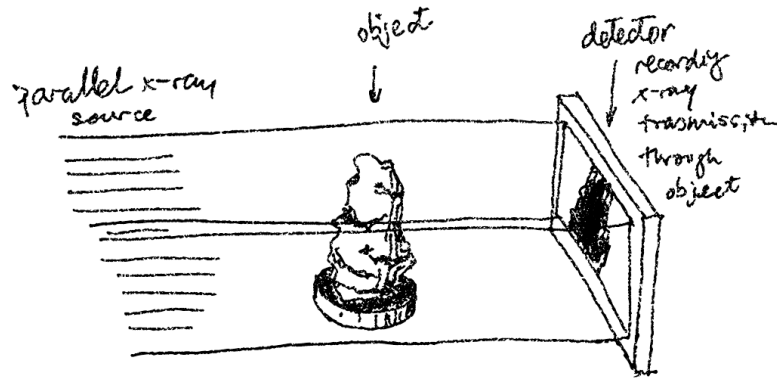


Figure 5: parallel\_3D

In a lab x-ray scanner, a different type of x-ray source is used, which emits a divergent x-ray beam from a small point (by focusing an electron beam onto a target which generates x-rays).

In the same vein as the higher up sketch above, the imaging system now looks like this:

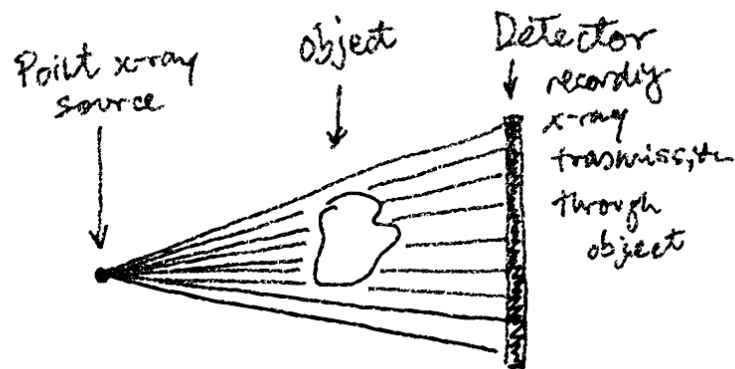


Figure 6: 2D illustration of a divergent x-ray beam, object, and detector system.

In 2D this is known as a fan-beam, and although the mathematical function representing the projection is a little more complex (and outside the scope of this tutorial), it

is possible to integrate along each beam path between pixel on the detector and the source. In this case the pixel size is not given by the physical size of pixels on the detector but rather the geometry of the imaging. The edges of a pixel and the source spot make a triangle, that describes the decreasing pixel size as a sample is translated closer to the source.

The same argument as above applies to the passage to 3D scanning with a flat-panel:

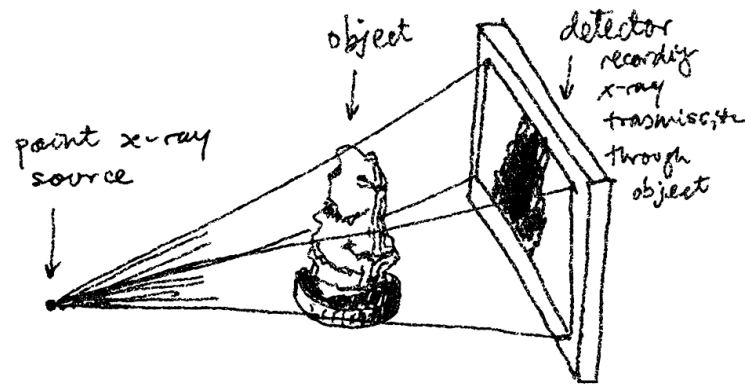


Figure 7: 3D illustration of a cone beam, object, detector system.

The “Feldkamp” algorithm can be used to reconstruct 3D divergent “cone beam” projections in 3D.

## 1.8 Quantitative use of the reconstructed field

The reconstructed field is basically  $\mu(x, y, z)$ . However unless a *monochromatic* (i.e., with only one energy) x-ray beam is used, or a *spectral* detector (which detects the energy of incoming photons, exceedingly rare as of time of writing), the dependency of  $\mu$  on x-ray energy cannot be made, meaning that the reconstructed value is often called a “CT value” rather than a quantitative  $\mu$ .

Polychromatic x-ray sources being detected with simple detectors (the overwhelmingly most common cause) can have some problems due to the fact that energy cannot be studied, such as an artefact called *beam hardening*.

Experience shows that between repeated scans in the same imaging configuration, the CT value can drift a little: this can normally be corrected by having some reference materials in the picture which can be used to normalise CT values with time.

However once this essential step is made, the evolution of CT values can be expected

to follow the mass transfer in the system. It is on this basis that optical flow equations (conservation of CT values) can be written, enabling particle tracking that will be the object of the next tutorial.

Going further, a recent paper [SAR<sup>+</sup>20] uses this fact to predict evolution of CT values during swelling.

## References

- [Kha13] Faycal Kharfi. Mathematics and physics of computed tomography (ct): demonstrations and practical examples. *Imaging and radioanalytical techniques in interdisciplinary research-fundamentals and cutting edge applications*, pages 81–106, 2013.
- [Ros70] K\_H Roscoe. The influence of strains in soil mechanics. *Geotechnique*, 20(2):129–170, 1970.
- [SAR<sup>+</sup>20] Eleni Stavropoulou, Edward Andò, Emmanuel Roubin, Nicolas Lenoir, Alessandro Tengattini, Matthieu Briffaut, and Pierre Bésuelle. Dynamics of water absorption in callovo-oxfordian claystone revealed with multimodal x-ray and neutron tomography. *Frontiers in Earth Science*, 8:6, 2020.
- [VdWSNI<sup>+</sup>14] Stefan Van der Walt, Johannes L Schönberger, Juan Nunez-Iglesias, François Boulogne, Joshua D Warner, Neil Yager, Emmanuelle Gouillart, and Tony Yu. scikit-image: image processing in python. *PeerJ*, 2:e453, 2014.



---

## 3D Analysis

**Edward Andò**

*EPFL Center for Imaging*

---

### 1 Introduction

As seen in the section on 2D imaging, to measure motion between two images of an evolving object two main principles can be used:

1. **Particle Tracking:** Identification of the object in every time frame, followed by a temporal linking of identified objects. In the fluid mechanics world this is close to “PTV” (Particle Tracking Velocimetry). This family of techniques is extremely efficient when reliable object identifications can be made systematically for the material — it is not only related to granular media: it can be effectively used to track pores or inclusions in a matrix.
2. **Image Correlation:** Tracking of greylevel texture using techniques based on greylevel conservation (“optical flow”) the family of Digital Image Correlation (more correctly Digital Volume Correlation when comparing 3D images), which map into “PIV” (Particle Image Velocimetry) in fluid mechanics. This technique is much more general than particle tracking, requiring “texture” in both images, but can be applied very successfully to granular materials.

This section will discuss both methods with some examples, starting with a general introduction for Digital Volume Correlation to introduce a “global” measurement of strain which will be used to help a particle tracking approach. Finally, image correlation will be also shown at the “micro” scale, for 3D volumes when particles are identifiable, and when they are not.

```
# Let's load some example data
import tifffile
import numpy
import matplotlib.pyplot as plt

im1 = tifffile.imread("M2EA05-01-bin4.tif").astype(float)
print(f"Shape of im1 (Z,Y,X): {im1.shape}")
```

```

im5 = tiffimage.imread("M2EA05-05-bin4.tif").astype(float)

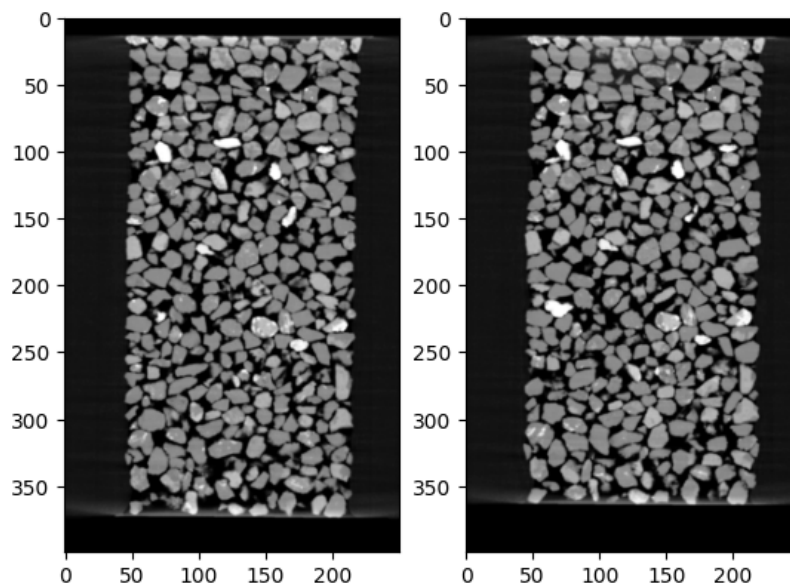
# Let's show some vertical slices
plt.subplot(1,2,1)
plt.imshow(im1[:, :, im1.shape[2]//2], cmap='Greys_r')
plt.subplot(1,2,2)
plt.imshow(im5[:, :, im5.shape[2]//2], cmap='Greys_r')
plt.show()

# Some vertical strain (being applied at the bottom) is
↪ visible!

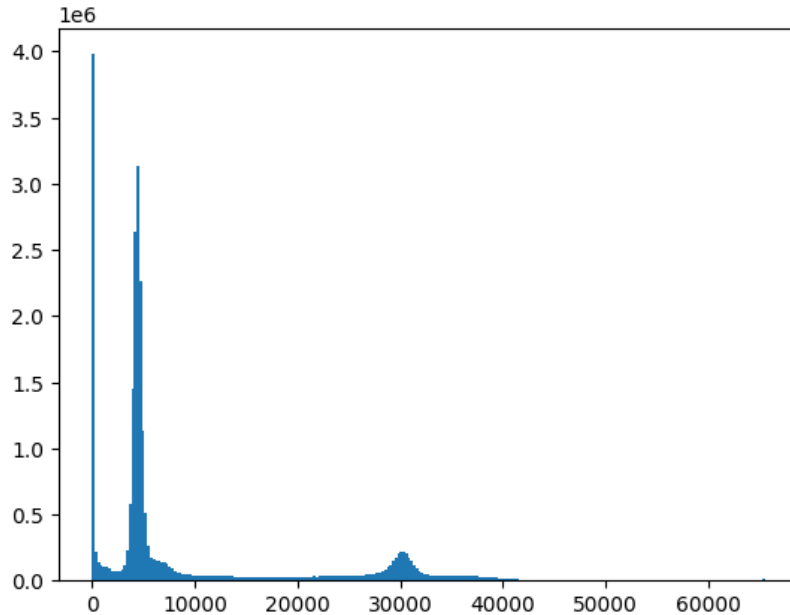
plt.hist(im1.ravel(), bins=256, range=[0, 65535])
plt.show()

```

Shape of im1 (Z,Y,X): (400, 250, 250)







We see that the distribution of the greyvalues in the image has a peak at zero (mask of the outside of the sample), a gaussian-looking peak around 5000 which represents the air CT value and another gaussian peak at 30000 CT values which represents the most common CT value for the particles, although it's visible from the slices that there are some brighter particles.

## 2 Digital Image/Volume Correlation for registration

In this first section, we will introduce Digital Volume Correlation in general, with the aim of mapping (“registering”) a whole 3D volume into another, *i.e.*, to measure the overall deformation between the two volumes.

3D correlation libraries are not so easy to find, here we will use *spam* (<https://pypi.org/project/spam/>) that includes this functionality. Spam proposes a non-rigid registration trying to find the optimal linear deformation function  $\Phi$  to map one image into the other.  $\Phi$  is expressed in homogeneous coordinates.

### 2.1 Homogeneous coordinates and $\Phi$

$\Phi$  will be a 4x4 matrix as follows:

$$\Phi = \begin{bmatrix} F_{zz} & F_{zy} & F_{zx} & t_z \\ F_{zy} & F_{yy} & F_{yx} & t_y \\ F_{xz} & F_{xy} & F_{xx} & t_x \\ 0 & 0 & 0 & 1 \end{bmatrix}$$

With 3D coordinates for a point:

$$x = (x, y, z)$$

we pad with a one and turn the coordinates into a column vector (this means we pass into a “homogeneous” coordinate system), to give:

$$x = \begin{bmatrix} z \\ y \\ x \\ 1 \end{bmatrix}$$

We can then transform the coordinate with the deformation function  $\Phi$  as follows:

$$\Phi \cdot x = x'$$

## 2.2 Identity Matrix

A  $\Phi$  which is the identity matrix does not deform the point

$$\Phi = \begin{bmatrix} 1 & 0 & 0 & 0 \\ 0 & 1 & 0 & 0 \\ 0 & 0 & 1 & 0 \\ 0 & 0 & 0 & 1 \end{bmatrix} \quad \text{and} \quad \Phi \cdot x = x$$

### 2.2.1 Translation

A simple translation of the point  $x$  is applied with components

$$t_x, t_y, t_z$$

$$\Phi = \begin{bmatrix} 1 & 0 & 0 & t_z \\ 0 & 1 & 0 & t_y \\ 0 & 0 & 1 & t_x \\ 0 & 0 & 0 & 1 \end{bmatrix}$$

When applied:

$$\Phi \cdot x = x' = \begin{bmatrix} z + t_z \\ y + t_y \\ x + t_x \\ 1 \end{bmatrix}$$

Remember that when dealing with differently binned images (see later), translations must be scaled, unlike linear transformations.

### 2.2.2 Linear transformations (rotations, “zoom”, “shear”)

All remaining components of the transformation are found mixed together in the top left 3x3 matrix in  $\Phi$ , leading to our familiar, from continuum mechanics, deformation gradient tensor  $\mathbf{F}$ .

For example uniaxial stretching can be performed by a change in the components along the diagonal of  $\mathbf{F}$ :

$$\Phi = \begin{bmatrix} F_{zz} & 0 & 0 & 0 \\ 0 & F_{yy} & 0 & 0 \\ 0 & 0 & F_{xx} & 0 \\ 0 & 0 & 0 & 1 \end{bmatrix}$$

Rotations in 3D can be quite complex. There are a number of different ways of representing rotations in 3D — see this very clear explanation on Wikipedia ([https://en.wikipedia.org/wiki/Rotation\\_formalisms\\_in\\_three\\_dimensions](https://en.wikipedia.org/wiki/Rotation_formalisms_in_three_dimensions)). A simple example of a rotation around the z axis of an angle  $\theta$  would look like :

$$\Phi = \begin{bmatrix} 1 & 0 & 0 & 0 \\ 0 & \cos \theta & -\sin \theta & 0 \\ 0 & \sin \theta & \cos \theta & 0 \\ 0 & 0 & 0 & 1 \end{bmatrix}$$

To represent rotations simply, we choose the *Rotation Vector* format, which is in the family of *axis-and-angle* representations. A rotation vector is a three-component vector whose direction is the rotation axis and whose length is the rotation angle in degrees.

### 2.2.3 Differences between images

In image correlation we have two images — *im1* and *im2* which differ in some way. We are looking for some  $\Phi$  that makes *im1* and *im2* as similar as possible. Here  $x$  is a position vector:

$$\text{im1}(x) = \text{im2}(\Phi \cdot x)$$

or:

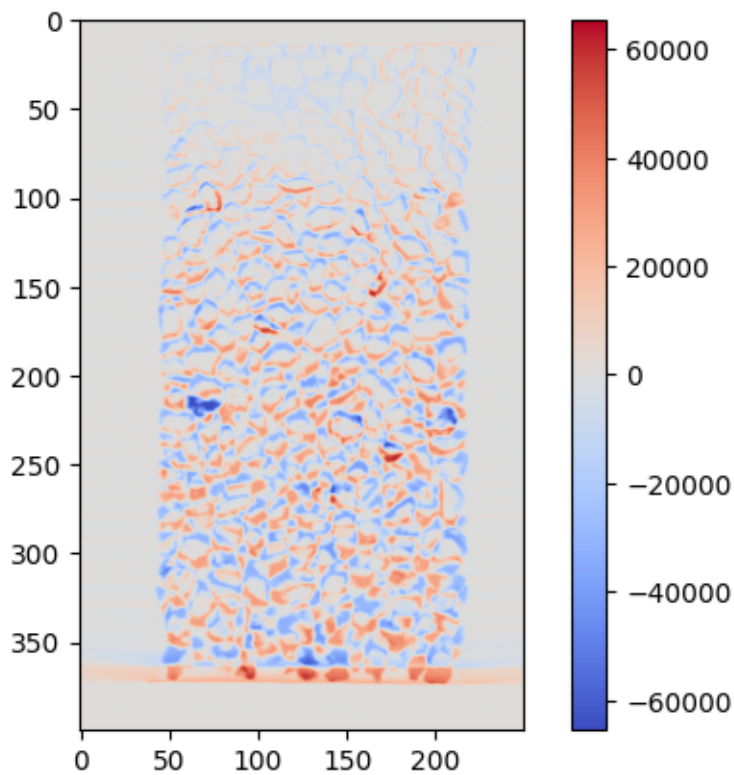
$$\text{im1}(x) - \text{im2}(\Phi.x) = 0$$

This is an important point to visualise: let's see what

$$\text{im1}(x) - \text{im2}(x)$$

looks like for two different images :

```
diff = im1[:, :, im1.shape[2]//2] - im5[:, :, im5.shape[2]//2]
plt.imshow(diff, cmap='coolwarm', vmin=-numpy.abs(diff).
    ↪max(), vmax=numpy.abs(diff).max())
plt.colorbar()
plt.show()
```



Blue means a negative number, grey = 0 and red is positive.

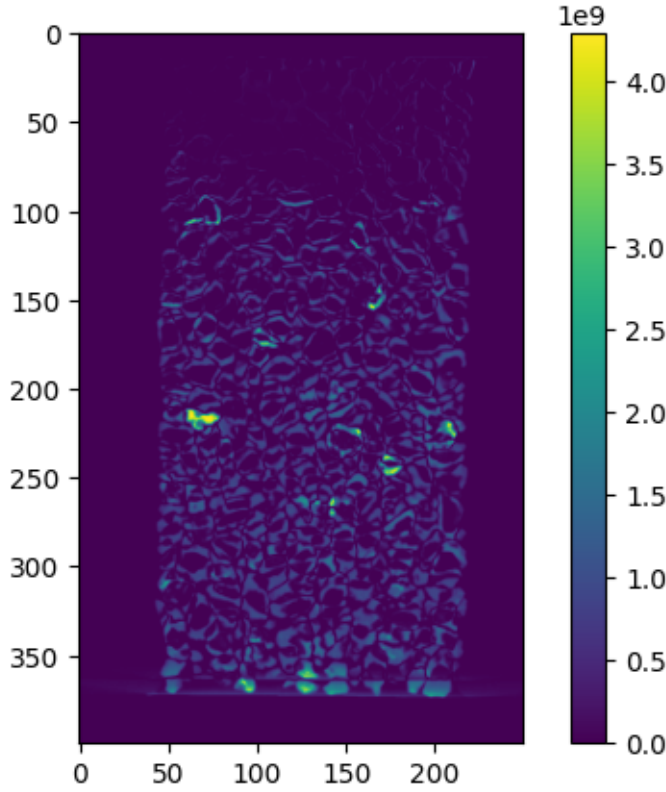
We can see that there are differences between these images. However, there is some alignment — especially the top of the sample seems good, and there is increasing mis-overlap as we go downwards towards 300. This is relatively expected, since we are loading the sample from the bottom. The middles of some particles have low error — but there are problems on the edges. Since the amount of dark and light voxels are approximately the same in the two images that have been subtracted, the sum of this image could be expected to be close to zero.

Under this transformation, this difference is clearly not zero. If **im1** and **im2** have been acquired with a real measurement device which has some noise, even with the *a-priori* knowledge of  $\Phi$  this difference will never be zero. In what follows, the objective will be to find the transformation  $\Phi$  that minimises this difference as far as possible.

If we'd like to define the difference between **im1** and **im2**, if we *square* the value of all the voxels in the difference, then low values will stay low, and highly negative and highly positive differences will both become highly positive. The choice of the *square* particular makes sense for Gaussian noise.

$$(\text{im1}(x) - \text{im2}(x))^2$$

```
diff = im1[:, :, im1.shape[2]//2] - im5[:, :, im5.shape[2]//2]
plt.imshow(diff**2)
plt.colorbar()
plt.show()
```



Here low values are well matched, and high values are poorly matched.

#### 2.2.4 Image correlation — Finding $\Phi$

We want to find  $\Phi$ . Since it has 12 unknowns ( $4 \times 4 = 16$  components, of which the bottom row is known), this is quite a complicated problem. The first thing to do is to define an error *function* of  $\Phi$ , which in this case is simply the classic *sum of squared difference* as introduced above, *i.e.*,

$$\mathcal{T}(\Phi) = \frac{1}{2} \sum_{x \in ROI} (\text{im1}(x) - \text{im2}(\Phi \cdot x))^2$$

$\mathcal{T}$  is a scalar function of the matrix  $\Phi$ . The scalar returned is the sum-of-squares difference between **im1** and **im2** deformed by  $\Phi$ . *ROI* is a 3D region-of-interest in which we are calculating this error, and for which we will now try to find  $\Phi$ . Since we're trying to measure a  $\Phi$  in a small region, rather than for every voxel (which would be impossible), we have written a *weak* form of the solution.

Given this error function we can state our objective more clearly: we would like to find a  $\Phi$  that minimises this error function. In previous work we had searched the space of displacements, rotations, *etc.* making small steps (line searches) to decrease the error, but what follows is much faster and more robust: we have implemented the incremental [LK<sup>+</sup>81] approach for image correlation. We use the formulation in homogeneous coordinates (*i.e.*, with  $\Phi$ ) by the LMT in [TJM<sup>+</sup>17], build on previous work such as [HR12].

Let's try to measure a single  $\Phi$  with the above approach to map the whole on image 1 into image 5.

Here we'll use the internal function programmed in spam, again, it is iterative, and will make progressive corrections to a guess initial  $\Phi$  function. The function will continue to iterate until the step size to correct  $\Phi$  has become very small, or unless we hit a maximum number of iterations.

Furthermore, to save time and increase robustness we will use a “multiscale” approach, which is a very common way to formulate problems in image analysis. In essence this means that we will downscale both images (8 times in this case) so that they are smaller, try to measure a  $\Phi$ , then downscale the original images only 4 times, and try to refine the  $\Phi$ , and repeat all the way back to the original images.

This means that a rough fit (which is not confused by fine details) is initially computed quickly computed (since there are fewer data and also less noisy, given the inherent averaging in downscaling images). The multiscale process can be seen in the output below: please note that the final converged result at each scale is printed, with the current  $\Phi$  decomposed into  $\mathbf{t}$  (a translation vector),  $\mathbf{r}$  (a rotation vector in degrees), and  $\mathbf{z}$  (a change of size of axes)

```
import spam.DIC
import spam.deformation

registration = spam.DIC.registerMultiscale(im1, im5, 8,
    verbose=True, imShowProgress=False)
```

```
spam.DIC.correlate.registerMultiscale(): working on binning: 8
```

```
    Iteration Number:17    dPhiNorm=0.00009    error=5971.78
    ↳t=[-0.453 -0.012
-0.146]    r=[-0.112 0.341 -0.065]    z=[0.972 1.015 1.021]
    ↳(Elapsed Time:
0:00:00)
```

```
Start correlation with Error = 10860.94
```

```
-> Converged
```

```
spam.DIC.correlate.registerMultiscale(): working on binning: 4
```

## 140 3D Analysis

```
Iteration Number:6    dPhiNorm=0.00007    error=3048.70  ┐
↪t=[-0.935 -0.014
-0.399]    r=[-0.115 0.330 -0.021]    z=[0.975 1.019 1.019]┐
↪(Elapsed Time:
0:00:00)

Start correlation with Error = 3173.32

-> Converged
spam.DIC.correlate.registerMultiscale(): working on binning:  2
Iteration Number:0    (Elapsed Time: 0:00:00)

Start correlation with Error = 1599.93

Iteration Number:5    dPhiNorm=0.00003    error=1590.55  ┐
↪t=[-1.903 -0.020
-0.804]    r=[-0.104 0.352 -0.043]    z=[0.975 1.018 1.019]┐
↪(Elapsed Time:
0:00:00)

-> Converged
spam.DIC.correlate.registerMultiscale(): working on binning:  1
Iteration Number:0    (Elapsed Time: 0:00:00)

Start correlation with Error = 1404.86

Iteration Number:6    dPhiNorm=0.00006    error=1402.39  ┐
↪t=[-3.798 -0.032
-1.628]    r=[-0.107 0.361 -0.042]    z=[0.975 1.018 1.019]┐
↪(Elapsed Time:
0:00:17)

-> Converged
```

```
# Decompose Phi from registration to make it more┐
↪understandable
PhiDecomposed = spam.deformation.
↪decomposePhi(registration['Phi'])

names = [['t', 'Translation px (z, y, x)'],
          ['z', 'Axis stretch (z, y, x)'],
          ['r', 'Rotation vector deg (z, y, x)']]

for n, N in names:
```



```
print(f"{N}:\n\t{PhiDecomposed[n]}\n")
```

```
Translation px (z, y, x):
      [-3.798 -0.032 -1.628]
```

```
Axis stretch (z, y, x):
      [0.9749452303793242, 1.0178265653802065, 1.
↪ 019311381463713]
```

```
Rotation vector deg (z, y, x):
      [-0.107  0.361 -0.042]
```

This allow the compression in Z to be seen (axis stretch in Z less than 1) with radial expansion in Y and X.

### 3 Particle identification

Particle-based analysis clearly requires the particles to be uniquely identified, which is really **the** key step in our opinion for the analysis of granular geomaterials.

Here we will use a pretty standard technique to separate particles: first we will binarise the image into only black and white or true and false voxels (which will indicate the solid, granular phase *v.s.* everything else). Given the low noise in the image we can quite safely just apply a threshold CT value, around 20000.

Thereafter a 3D watershed algorithm will be applied. This was invented by [Beu79], and improved by [BM18]. Here we're using the helper function from the *spam* library [SAR<sup>+</sup>20] which implement's ITK's watershed [BL06]. In short, in this sub-species of this method, we will first attempt to find “markers” in the inside of each particle in 3D. This is achieved by working on the binary image - the 3D Euclidean distance map is computed on the grain phase, computing the distance for each grain-voxel to the other voxels. This field is expected to increase towards the centre of grains, and in the case of quite rounded particles is expected to have a single peak in the middle of the particle. Therefore the local maxima of the distance map are identified — in order to have some robustness to convex but non-spherical shapes some nearby maxima can be merged into a single one.

Once this is done, each merged marker will be given a unique number (label), and these markers will be grown using the watershed algorithm and the Euclidean distance map until they cover all the solid phase and generally should only touch at the contacts.

There are subtle differences between “interpixel” algorithms and “watershed line” implementations: the interpixel will label all voxels of the grain phase as belonging to a label, whereas the watershed line will split particles at the contacts. The algorithm used here is an interpixel one, so we'll get touching labels out directly.

Let's run the algorithm and see what happens!

```
import spam.label

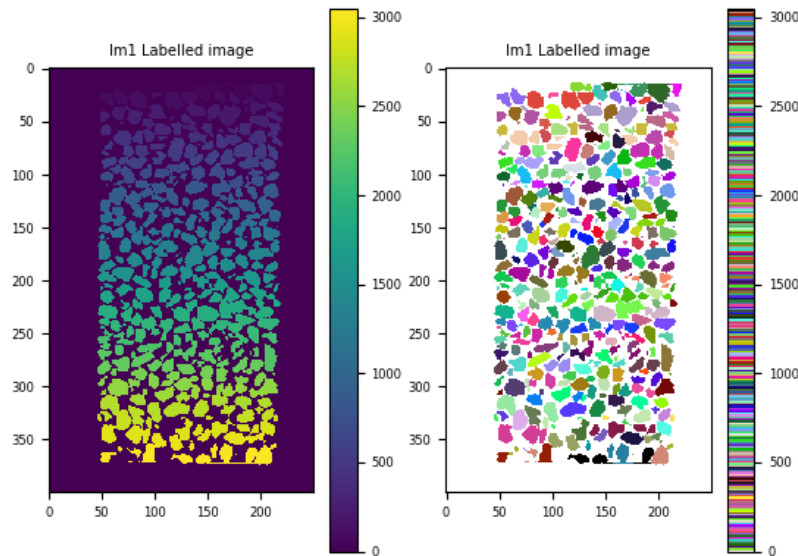
# This could take a few minutes, so we'll leave it in a cell
↳by itself
im1lab = spam.label.watershed(im1 > 20000)

# Let's see what happened
print(f"The maximum value found in the labelled im1 is {im1lab.
↳max()}")

# Let's show some vertical slices
plt.subplot(1,2,1)
plt.title("Im1 Labelled image")
plt.imshow(im1lab[:, :, im1.shape[2]//2],
            interpolation='none')
plt.colorbar()
plt.subplot(1,2,2)
plt.title("Im1 Labelled image")
plt.imshow(im1lab[:, :, im5.shape[2]//2],
            cmap=spam.label.randomCmap,
            interpolation='none')
plt.colorbar()

plt.show()
```

The maximum value found in the labelled im1 is 3052



How to interpret these images? In general labelling algorithms proceed down one direction, as can be seen on the left, label values seem to increase as Z increases.

On the right, we're using a special colourmap inspired by [GvdHTG07] where each level of the colourmap is randomised to accentuate differences between nearby values.

What is visible here is that each grain pixel (identified previously with a greyscale threshold) has a label number; the non-grain phase has value 0 and each identified contiguous (i.e., touching) blob of voxels has a unique label number identifying it.

Generally the algorithm seems to have done a good job: there is a possible merged label in the middle of the volume (this is called undersegmentation), however oversegmentation (a real particle split into two or more labels) does not seem to be present.

A labelled image allows discrete analysis, but extracting and interrogating each label individually. This is very easy to program, it simply means fetching all the voxels corresponding to a given label: thereafter a number of computations are easy, such as:

- the barycentre of the object (the spatial average of the coordinates of each voxel)
- the volume (the sum of the voxels)
- Some shape/orientation descriptors such as the orientated caliper lengths or “feret diameters” or the moment of inertia

Other measurements on discretely voxelised objects require a little more care:

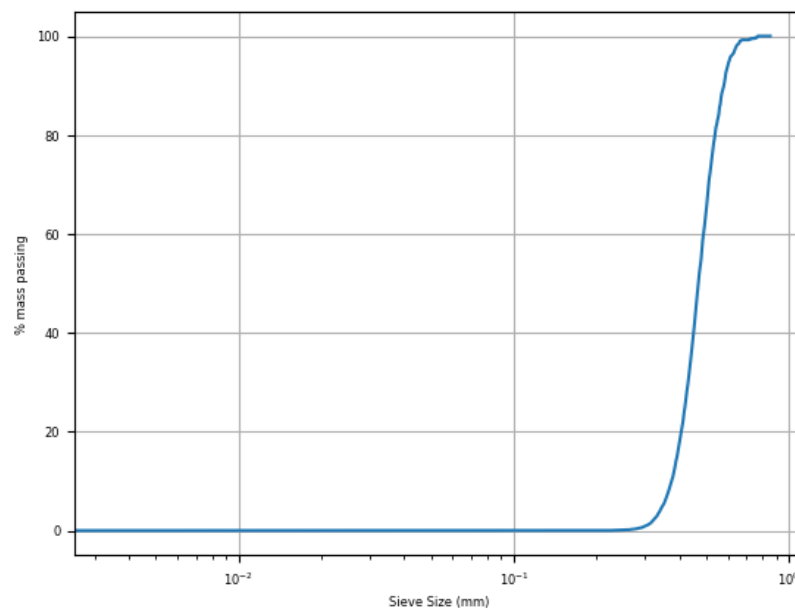
- surface area
- interparticle contact presence and orientation

The article [AV18] treats this exact problem in more detail.

As an illustration, the volume of each particle can be easily computed, allowing the diameter of the sphere of the same volume to be computed, from here a per-particle, particle size distribution can be computed. Please note that the 215.56 represents the conversion between pixels and mm.

```
im1radii = spam.label.equivalentRadii(im1lab)

import spam.plotting
spam.plotting.plotParticleSizeDistribution(im1radii*2*15.56/
    ↪1000,
                                     cumulative=True,
    ↪
    ↪cumulativePassing=True,
                                     mode="mass",
                                     logScaleX=True,
                                     logScaleY=False,
                                     units="mm")
```



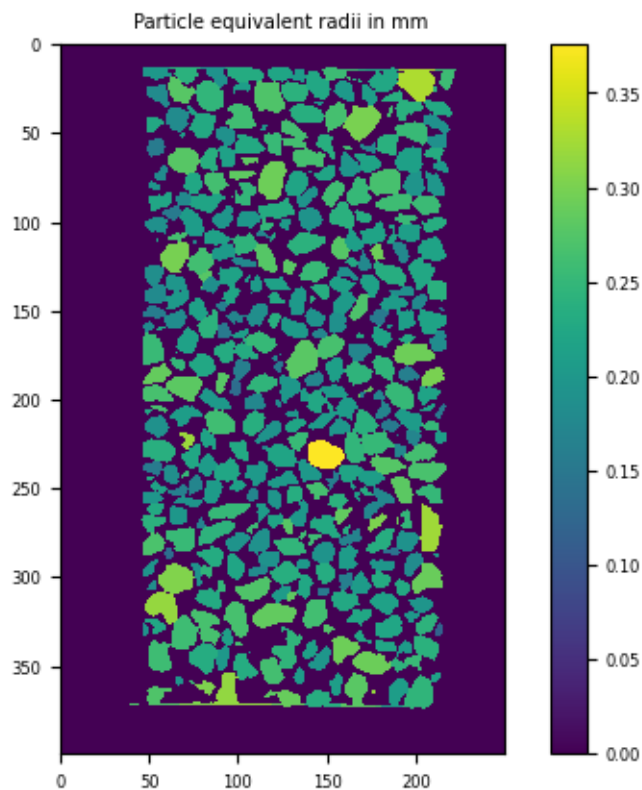
You might have seen pictures where grains are coloured according to some scalar. There are programmatically elegant ways to do this, but we can use a brute force approach here where all label values are simply replaced in a new image with corresponding values in a vector... for example the equivalent radii would work:

```

tmp = spam.label.convertLabelToFloat(im1lab[:, :, (im1.
    ↪shape[2]//2)-2:(im1.shape[2]//2)+2],
                                     im1radii*2*15.56/1000)

plt.title("Particle equivalent radii in mm")
plt.imshow(tmp[:, :, 2],
           interpolation='none')
plt.colorbar()
plt.show()

```



We can also use such measurements to make a quality control of the specimen... for example checking the spatial distribution of the large particles.

## 4 Particle Tracking

For a particle tracking approach we need to identify objects in the other image. It seems reasonable to keep the threshold the same, so let's compute `im5label`, and com-

pare it to im1label:

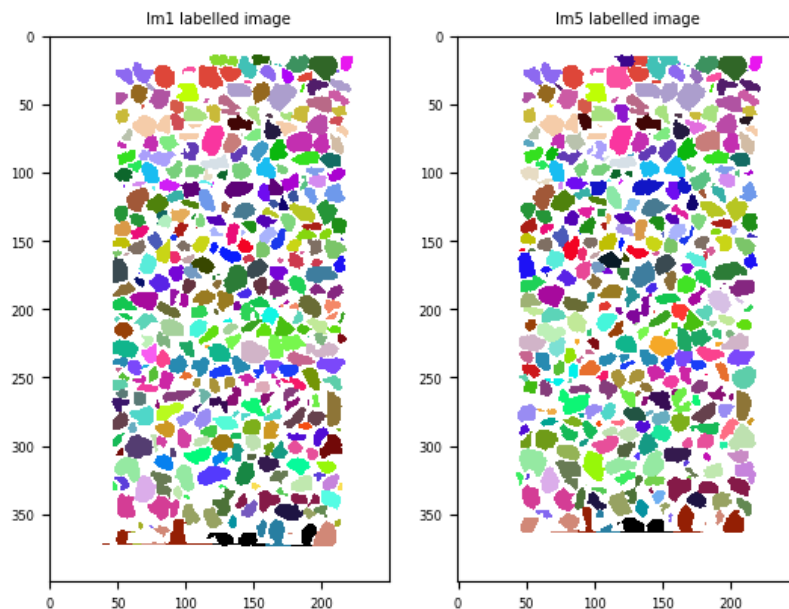
```
im5lab = spam.label.watershed(im5 > 20000)
print(f"The maximum value found in the labelled im1 is {im1lab.
    ↳max()}")
print(f"The maximum value found in the labelled im5 is {im5lab.
    ↳max()}")

plt.subplot(1,2,1)
plt.title("Im1 labelled image")
plt.imshow(im1lab[:, :, im1.shape[2]//2],
           cmap=spam.label.randomCmap,
           interpolation='none')
plt.subplot(1,2,2)
plt.title("Im5 labelled image")
plt.imshow(im5lab[:, :, im5.shape[2]//2],
           cmap=spam.label.randomCmap,
           interpolation='none')

plt.show()
```

The maximum value found in the labelled im1 is 3052

The maximum value found in the labelled im5 is 3035



Looking at label colours at the top (Z=low) of the volume, particles seem to have

corresponding colours, however this correspondence is lost towards the bottom of the volume. This is either due to different amount of over- and under-segmentation in both images, which will make tracking difficult, or more benignly due to particle rearrangements (especially in the Z-direction) which will change the sequencing of labels.

A particle tracking technique simply now becomes a question of linking labels in image 1 to labels in image 5. This tracking/particle recognition can become quite sophisticated, but here we will just match particles based on nearest neighbours. More sophisticated techniques such as ID-Track have been developed for geomaterials [AHV<sup>+</sup>12], but the general framework worth delving into is the “Hungarian Method” [Kuh55].

This means that we will compute particle centers in image 1, apply the above-measured Phi to each centre to move it to an approximate position in image 5, and match each image 1 particle to the closest in image 5.

```
im1centers = spam.label.centresOfMass(im1lab)
# Each row in im1centers represents the z, y, x positions in
# pixels of the particle of that row number.
print(im1centers)
im5centers = spam.label.centresOfMass(im5lab)

[[ 0.      0.      0.   ]
 [ 16.845  54.581 127.949]
 [ 19.901  84.51  64.063]
 ...
 [368.836 193.365 105.735]
 [370.304 183.124  73.776]
 [369.94  184.613  92.404]]

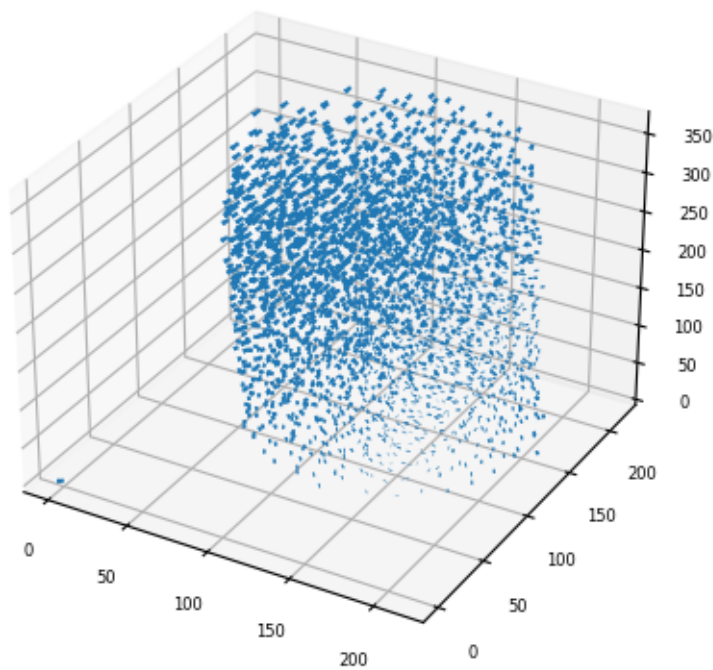
registrationDisplacements = spam.DIC.
    ↳applyRegistrationToPoints(registration['Phi'],
                                (numpy.
    ↳array(im1.shape) - 1) / 2.0,
    ↳im1centers,
    ↳applyF='no',
    ↳verbose=True)[: , 0:3, -1]

im1centersDeformed = im1centers + registrationDisplacements

ax = plt.figure().add_subplot(projection='3d')
```

```
ax.quiver(im1centers[:,2],
          im1centers[:,1],
          im1centers[:,0],
          registrationDisplacements[:,2],
          registrationDisplacements[:,1],
          registrationDisplacements[:,0],
          length=1,
          normalize=False)

plt.show()
```



```
import scipy.spatial

distanceMatrix = scipy.spatial.
    ↪ distance_matrix(im1centersDeformed, im5centers)
```

```
labelCorrespondence5_to_1 = numpy.zeros(distanceMatrix.
    ↪ shape[1])
```



```

for im5l in range(distanceMatrix.shape[1]):
    #print(numpy.argmin(distanceMatrix[im1l]))
    labelCorrespondence5_to_1[im5l] = numpy.
    ↪argmin(distanceMatrix[:,im5l])

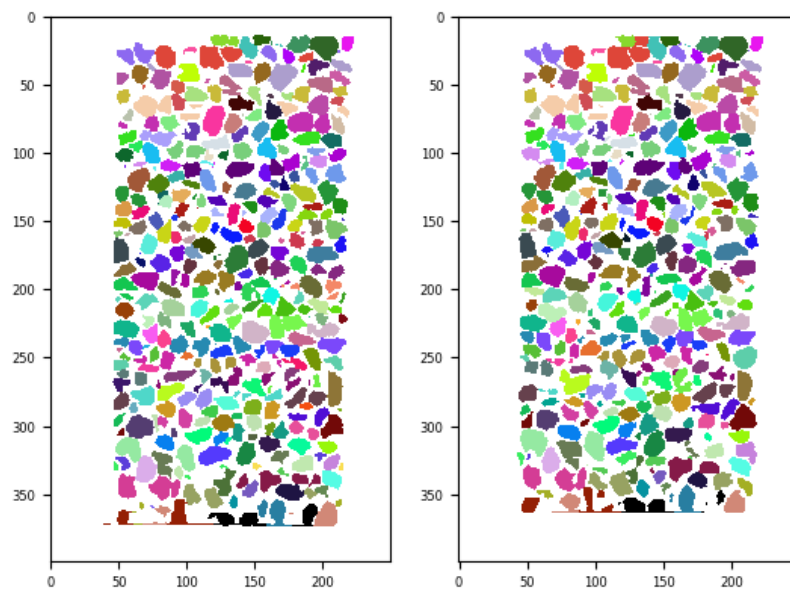
```

```

im5relab = spam.label.convertLabelToFloat(im5lab, ↪
    ↪labelCorrespondence5_to_1)
im5newcenters = spam.label.centresOfMass(im5relab)

# Let's show some vertical slices
plt.subplot(1,2,1)
plt.imshow(im1lab[:, :, im1.shape[2]//2],
           cmap=spam.label.randomCmap, interpolation='none')
plt.subplot(1,2,2)
plt.imshow(im5relab[:, :, im5relab.shape[2]//2],
           cmap=spam.label.randomCmap, interpolation='none')
plt.show()

```



```

particleTrackingDisplacements = im1centers - im5newcenters

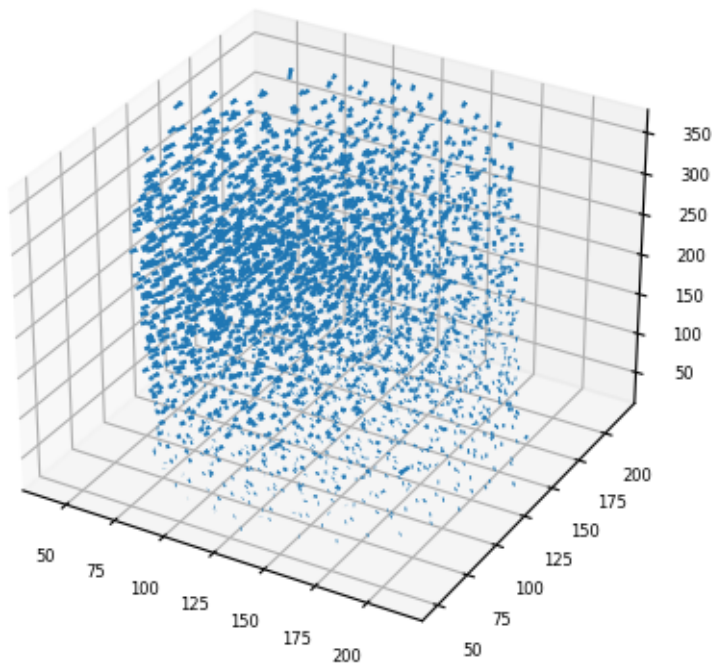
ax = plt.figure().add_subplot(projection='3d')
ax.quiver(im1centers[:,2],
          im1centers[:,1],
          im1centers[:,0],

```

```

particleTrackingDisplacements[:,2],
particleTrackingDisplacements[:,1],
particleTrackingDisplacements[:,0],
length=1,
normalize=False)
plt.show()

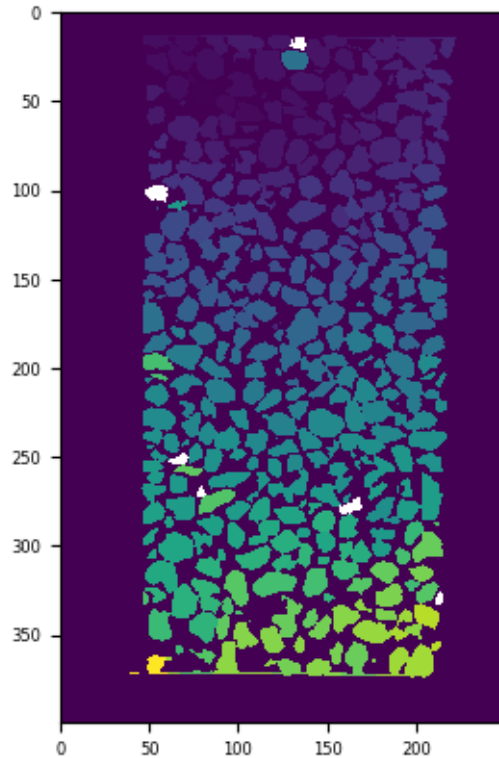
```



```

tmp = spam.label.convertLabelToFloat(im1lab[:, :, (im1.
    ↳shape[2]//2)-2:(im1.shape[2]//2)+2],
                                numpy.sqrt(numpy.sum(numpy.
    ↳square(particleTrackingDisplacements), axis=1)))
plt.imshow(tmp[:, :, 2],
            interpolation='none')
plt.show()

```



## 5 Discrete DVC

Now we will use **only** the labelled image in the reference configuration (`im1lab`) and adapt the earlier registration procedure to operate on a grain-by-grain basis. In the language introduced above, we will perform one registration procedure per grain setting the ROI to be the label for each grain. This “Discrete DVC” procedure was proposed in [HLV<sup>+</sup>09] and has found a lot of success in image-based particle tracking.

It has the advantage that the labelled image is only used once and thus can be optimised and manually checked and corrected until it is almost as good as possible.

As before we will take into account the overall registration between image 1 and image 5 as the initial guess for particle displacements.

```
import spam.helpers
tiff.save("M2EA05-01-bin4-lab.tif", im1lab)
spam.helpers.writeRegistrationTSV("M2EA05-01-05-bin4.tsv",
                                (numpy.array(im1.shape) - 1) / 2.0,
```

```

                                registration)
! spam-ddic "M2EA05-01-bin4.tif" "M2EA05-01-bin4-lab.tif"
↪ "M2EA05-05-bin4.tif" -pf "M2EA05-01-05-bin4.tsv"

DDIC = spam.helpers.
↪ readCorrelationTSV("M2EA05-01-bin4-M2EA05-05-bin4-ddic.tsv")['PhiField']

tmp = spam.label.convertLabelToFloat(im1lab[:, :, (im1.
↪ shape[2]//2)-2:(im1.shape[2]//2)+2],
                                numpy.sqrt(numpy.
↪ sum(numpy.square(DDIC[:,0:3,-1]), axis=1)))
plt.imshow(tmp[:, :, 2],
            interpolation='none')
#plt.show()

spam.tsvio.readCorrelationTSV(): Number of labels: 3053

<matplotlib.image.AxesImage at 0x7f0a4477a810>

```

## 5.1 Computing strains

What to do with this 3D displacement field? A natural question is to try to convert it into strains.

This is essentially a coarse-graining problem (mixed with a strain calculation problem). The two main families of approaches are:

- Grain based: particle centres are triangulated with an appropriate algorithm (Delaunay-style), making tetrahedra in 3D thus creating a basis on which strains can be calculated
- Spatial: A 3D grid is computed and particle kinematics are computed on the grid, where cubic shape functions can be used to compute strains.

Both options are available in spam, and both will be illustrated now (although the tetrahedra; strains will be rendered with an external programme — Paraview).

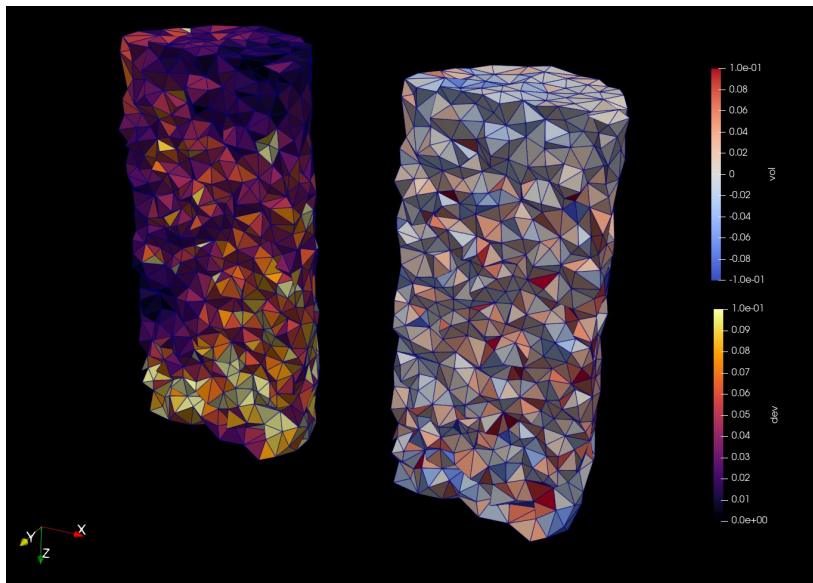
### 5.1.1 Tetrahedra

In the case of dense, mono-disperse spherical packings a Delaunay triangulation will create tetrahedra whose vertices will be at the particle contacts. In the case of poly-dispersity, this is not respected, so adding a weight to the triangulation (making it a Radical Delaunay, or “Laguerre” triangulation) will help improve things.

Strains can be computed on this tetrahedral basis as per [Bag96] and later [ZR15]:

```
! spam-discreteStrain M2EA05-01-bin4-M2EA05-05-bin4-ddic.tsv
→-tri -a 300 -rl M2EA05-01-bin4-lab.tif
```

This file is then loaded into paraview, showing a mesh of tetrahedra that link particle centres. For this visualisation, the cylinder is cut in half to reveal tetrahedra, which are coloured either by the deviatoric strains computed by the displacements of the four particles at each vertex, or volumetric strains:



This clearly shows some clear concentrations of deviatoric strain early in the test. We can compare these fields to the grid processing method:

## 5.2 Grid analysis

```
! spam-passPhiField -im1 M2EA05-01-bin4-lab.tif -ns 10 -vtk
→-pf M2EA05-01-bin4-M2EA05-05-bin4-ddic.tsv -tif
! spam-regularStrain
→M2EA05-01-bin4-M2EA05-05-bin4-ddic-passed-ns10.tsv -Q8 -rst
→1 -tif
```

```
plt.subplot(1,3,1)
zField = tiffFile.
→imread("M2EA05-01-bin4-M2EA05-05-bin4-ddic-passed-ns10-Zdisp.tif")
plt.title("Z displacement field on grid")
plt.imshow(zField[:,zField.shape[1]//2], cmap='inferno')
plt.colorbar()
```

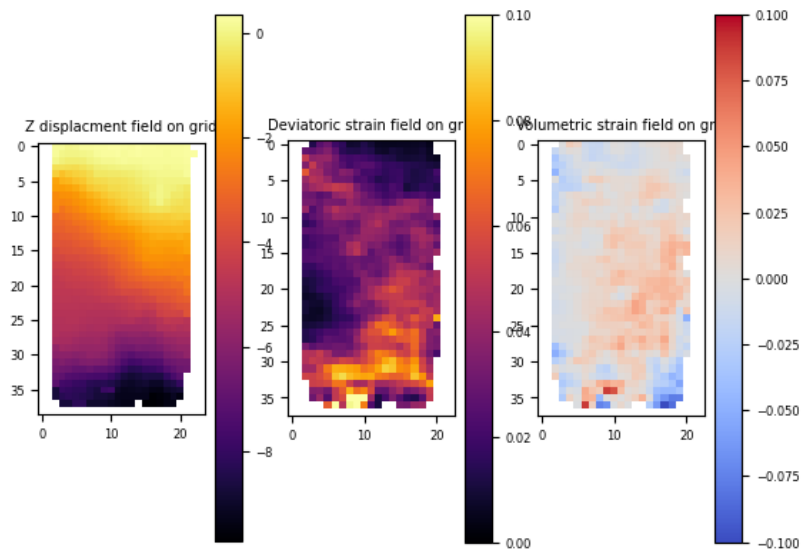
```

plt.subplot(1,3,2)
devField = tifffile.
    ↳ imread("M2EA05-01-bin4-M2EA05-05-bin4-ddic-passed-ns10-dev-Q8.tif")
plt.title("Deviatoric strain field on grid")
plt.imshow(devField[:,devField.shape[1]//2], cmap='inferno',
    ↳ vmin=0, vmax=0.1)
plt.colorbar()

plt.subplot(1,3,3)
volField = tifffile.
    ↳ imread("M2EA05-01-bin4-M2EA05-05-bin4-ddic-passed-ns10-vol-Q8.tif")
plt.title("Volumetric strain field on grid")
plt.imshow(volField[:,volField.shape[1]//2], cmap='coolwarm',
    ↳ vmin=-0.1, vmax=0.1)
plt.colorbar()

plt.show()

```



It is our contention that these continuous fields are easier to interpret. A final question may come to mind: why not simply split the reference image into cubic correlation volumes (and not use the labelled image), since the displacement field is interpolated onto a regular grid using this method? The fact of the matter is that the labelled image is the perfect definition of the objects that will move in this image, and so it is the most pertinent base on which to do the tracking!

## References

- [AHV<sup>+</sup>12] Edward Andò, Stephen A Hall, Gioacchino Viggiani, Jacques Desrues, and Pierre Bésuelle. Grain-scale experimental investigation of localised deformation in sand: a discrete particle tracking approach. *Acta Geotechnica*, 7(1):1–13, 2012.
- [AV18] Edward Andò and Gioacchino Viggiani. On the ease of experimental access to deformation entities in granular assemblies. *Ital. Geotech. J*, 52(2):44–51, 2018.
- [Bag96] Katalin Bagi. Stress and strain in granular assemblies. *Mechanics of materials*, 22(3):165–177, 1996.
- [Beu79] Serge Beucher. Use of watersheds in contour detection. In *Proceedings of the International Workshop on Image Processing*. CCETT, 1979.
- [BL06] Richard Beare and Gaëtan Lehmann. The watershed transform in itk-discussion and new developments. *Insight J*, 92:1–24, 2006.
- [BM18] Serge Beucher and Fernand Meyer. The morphological approach to segmentation: the watershed transformation. In *Mathematical morphology in image processing*, pages 433–481. CRC Press, 2018.
- [GvdHTG07] Chris Glasbey, Gerie van der Heijden, Vivian FK Toh, and Alision Gray. Colour displays for categorical images. *Color Research & Application: Endorsed by Inter-Society Color Council, The Colour Group (Great Britain), Canadian Society for Color, Color Science Association of Japan, Dutch Society for the Study of Color, The Swedish Colour Centre Foundation, Colour Society of Australia, Centre Français de la Couleur*, 32(4):304–309, 2007.
- [HLV<sup>+</sup>09] SA Hall, N Lenoir, G Viggiani, J Desrues, and P Bésuelle. Strain localisation in sand under triaxial loading: characterisation by x-ray micro tomography and 3d digital image correlation. In *Proceedings of the 1st Int. Symp. On Computational Geomechanics (ComGeo 1)*, pages 239–247, 2009.
- [HR12] François Hild and Stéphane Roux. Comparison of local and global approaches to digital image correlation. *Experimental Mechanics*, 52(9):1503–1519, 2012.
- [Kuh55] Harold W Kuhn. The hungarian method for the assignment problem. *Naval research logistics quarterly*, 2(1-2):83–97, 1955.
- [LK<sup>+</sup>81] Bruce D Lucas, Takeo Kanade, et al. *An iterative image registration technique with an application to stereo vision*, volume 81. Vancouver, 1981.

- [SAR<sup>+</sup>20] Olga Stamati, Edward Andò, Emmanuel Roubin, Rémi Cailletaud, Max Wiebicke, Gustavo Pinzon, Cyrille Couture, Ryan Hurley, Robert Caulk, Denis Caillerie, et al. Spam: software for practical analysis of materials. *Journal of Open Source Software*, 5(51):2286, 2020.
- [TJM<sup>+</sup>17] Erika Tudisco, Clément Jailin, Arturo Mendoza, Alessandro Tenggatini, E Andò, Stephen A Hall, Gioacchino Viggiani, Francois Hild, and Stéphane Roux. An extension of digital volume correlation for multimodality image registration. *Measurement Science and Technology*, 28(9):095401, 2017.
- [ZR15] Boning Zhang and Richard A Regueiro. On large deformation granular strain measures for generating stress–strain relations based upon three-dimensional discrete element simulations. *International Journal of Solids and Structures*, 66:151–170, 2015.



---

# Stress and Force Measurements in 3D

**Ryan Hurley**

*Johns Hopkins University  
Department of Mechanical Engineering*

---

Here we provide an introduction to the use of x-ray imaging and diffraction techniques for stress and force measurements in geomaterials (sand, rocks, concrete). A brief history, an overview of the fundamental concepts, and some example applications and data are provided.

## 1 Introduction

3D x-ray diffraction (3DXRD, also called far-field high-energy diffraction microscopy, FF-HEDM) has been developed and employed for over two decades in the study of strain tensors, orientations, and positions of individual grains within polycrystalline materials [PNL<sup>+</sup>01, Pou04]. In the last decade, 3DXRD data analysis has matured and been implemented in several open-source codes now routinely used at synchrotron beamlines including the Advanced Photon Source (APS), the European Synchrotron Radiation Facility (ESRF), and the Cornell High Energy Synchrotron Source (CHESS) [SHO12, SAP<sup>+</sup>16, BBLM11, OSP<sup>+</sup>10, Wri17].

About one decade ago, geomechanics researchers began to employ x-ray diffraction and neutron diffraction measurements to investigate strain states of individual grains and bulk grain packings in natural geomaterials such as sands [HWP<sup>+</sup>11]. At the time, there was only the “tantalising” indication of the potential of such methods for studying granular media and other geomaterials. Ten years on, we have witnessed tremendous progress in multi-modal measurements in geomaterials enabled by x-ray scattering and particularly 3DXRD. The tantalising prospects identified ten years ago [HWP<sup>+</sup>11] have led to studies of grain strains and stresses in small uniaxially-compressed sand samples [ACKL13, HW15], the first inference of force vectors in 3D quartz sphere packings [HHAW16], and a steady stream of new insight into 3D granular packings, including insight into: breakage mechanics, length scales, grain-scale dissipation, ultrasound wave propagation, and particle rearrangements [HHW17, HLP<sup>+</sup>18, ZHHH19, ZHH20, SHHH22, ZAE<sup>+</sup>22].

Researchers have also begun to apply 3DXRD to the study of geomaterials other than loose granular materials, including salt rock and concrete [MAT<sup>+</sup>21, ZPH20, HP19]. These studies have provided, for instance, insight into grain-resolved stresses in support of validating micromechanics theories for concrete. In the near future, it is likely that 3DXRD will become an increasingly useful tool for quantifying grain-resolved stress and its heterogeneity in a variety of geomaterials. Our group has begun to use 3DXRD heavily at synchrotron facilities, and recently with laboratory x-ray sources (using an Excillum MetalJet x-ray source) to study stress fields in sandstones, salt rock, and various cementitious composites in stress or fluid-submersion states relevant to applications. As noted throughout this doctoral school, the goal of the geomechanics researcher is often to examine the mechanical response of geomaterials in the context of constitutive relationships, which relate stress and strain. Although strain, as relevant to continuum constitutive relations, can be calculated using particle kinematics alone, spatially-resolved stress measurements require a measurement of intra-particle deformation which can be supplied by 3DXRD.

## 2 Experimental setup

### 2.1 Material basics

Grain-resolved stress measurements with 3DXRD require the use of crystalline materials. Experiments were first performed on synthetic single crystals (*e.g.* SiO<sub>2</sub> (quartz), Al<sub>2</sub>O<sub>3</sub> (sapphire, ruby, or alumina), and NaCl (halite)) to take advantage of pristine lattice structures which led to well-defined and ideal diffraction peaks [HWP<sup>+</sup>11, HW15, MAT<sup>+</sup>21]. More recently, 3DXRD measurements of grain-resolved stress have been successfully performed in natural sand grains, which are primarily single SiO<sub>2</sub> crystals with minor crystalline mosaicity or imperfections [CAKL14, CAK17]. Our group is increasingly applying 3DXRD to make grain-resolved stress measurements in sandstone, which is essentially a naturally-sintered solid composed of sand grains. Natural sandstones, including Berea, Nugget, and Bentheimer, are quartz-rich and produce clear, albeit slightly streaked or elongated, diffraction spots amenable to 3DXRD analysis.

### 2.2 Experimental Configurations and Basic Theory

Currently, x-ray computed tomography (XRCT) and 3DXRD can be performed together (simultaneously or sequentially) *in-situ* at the APS ID1, the ESRF ID11, the CHESS FAST 3A, the Petra III P07, and the Soleil Psiche beamlines. XRCT can be performed in many more locations than this of course, including in many laboratories, but 3DXRD requires the use of monochromatic, or single-energy, x-rays. Monochromatic x-rays must be used because the principal upon which 3DXRD is based is Bragg's law, which is described more in the coming paragraphs. We have performed combined XRCT and 3DXRD measurements only at the first three facilities. The general experimental configuration for combined XRCT and 3DXRD is shown in Fig. 1.

In addition to the requirement of samples containing crystalline grains described in Sec. 2.1, key hardware of experiments for geomechanics researchers include:

1. A loading frame to subject geomaterials to desired stress or strain paths.
2. A scintillator or near-field tomography detector for radiography measurements which can be used for XRCT.
3. A far-field area detector for diffraction pattern measurements which can be used for 3DXRD analysis.

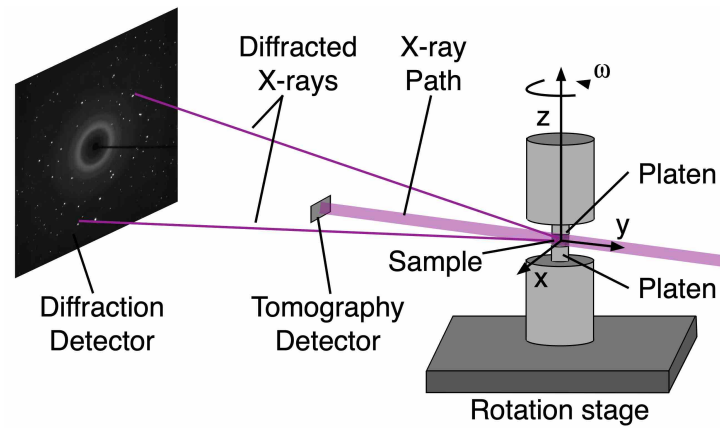


Figure 1: Standard experimental setup for combined *in-situ* XRCT and 3DXRD at APS ID1, ESRF ID11, and CHESS FAST 3A. A load frame is mounted on a rotation stage that permits 360° sample rotation while radiographs are captured for XRCT and diffraction patterns are captured for 3DXRD analysis. See [HHAW16, HLP<sup>+</sup>17, HHW17, ZHHH19, SHHH22, HP19] for descriptions of experiments in granular materials and concrete using this experimental setup.

The XRCT data analysis follows protocols described in the chapter on 3D tomography of opaque materials for parallel x-ray beams featured at all synchrotron facilities. We use open-source software tomopy, pyHST, or Nabu for reconstruction of synchrotron data. We therefore omit a description of XRCT data analysis here.

The 3DXRD data analysis follows procedures described in some detail in [BBLM11, OSP<sup>+</sup>10] and in more detail in Sec. 3. The principal upon which 3DXRD is based is Bragg's law, or coherent scattering of x-ray waves from single crystals. Bragg's law is a special case of Laue diffraction that provides the angles of diffraction of x-rays from a single crystal as a function of the diffraction order,  $n$ , the wavelength of x-rays,  $\lambda$ , the  $d$  space of the diffracting crystal planes, and the scattering angle,  $\theta$ :

$$n\lambda = 2d \sin \theta. \quad (1)$$

Figure 2 provides an illustration of the principal of Bragg diffraction, showing both constructive and destructive interference of waves (photons) at two incident and diffraction angles.

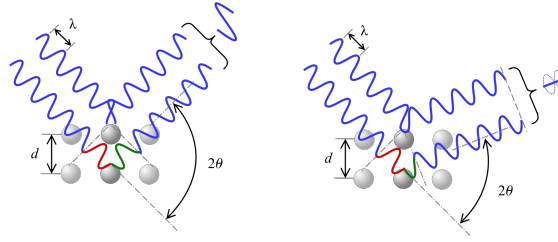


Figure 2: Bragg diffraction.

When performing 3DXRD measurements, the sample of interest is typically rotated  $360^\circ$  to capture anywhere between 1,440 and 3,600 diffraction patterns on the far-field detector (see Fig. 1). Each diffraction pattern contains a collection of Bragg peaks (also called spots or reflections) generated via scattering according to Bragg's law. In order to fully understand 3DXRD patterns for a given sample, the crystal structure of the grains within the material must be known *a priori* – this crystal structure determines the angles  $2\theta$  at which we expect to observe diffraction peaks on the far-field diffraction detector shown in Fig. 1. The  $\text{SiO}_2$  found in most quartz-rich geomaterials is alpha-quartz, which has a trigonal (rhombohedral) crystal structure in Space group 152. The unit cell parameters are well documented and are approximately  $a = b = 4.9137\text{\AA}$ ,  $c = 5.4047\text{\AA}$ ,  $\alpha = \beta = 90^\circ$  and  $\gamma = 120^\circ$ . Practically, what is important for 3DXRD and also powder diffraction is the lattice spacing of the atoms in this crystal and, given the energy of incident x-rays and Bragg's law in Eq. 1, the scattering angle  $2\theta$ .

Figure 3 illustrates the triaxial load frame and experimental setup used in our recent experiments combining XRCT and 3DXRD. Figure 3(a) shows the load frame in our RX Solutions EasyTom 160 MicroCT at JHU, Fig. 3(b) shows a cross-section of the load frame's interior, and Fig. 3(c) shows the load frame at the APS ID1 where it was used for XRCT and 3DXRD measurements.

Figure 4(a) shows a horizontal slice through a tomography reconstruction of a single-crystal quartz sample containing about 1,500 grains subjected to 30 MPa confining pressure in the triaxial load frame shown in Fig. 3. Figure 4(b) shows the diffraction patterns from the same experiment, in particular the maximum intensity on the far-field diffraction detector (see Fig. 1) over all 3,600 diffraction patterns obtained during a  $360^\circ$  sample rotation. For this experiment, the x-ray energy was 71.676 keV and the sample-to-detector distance was about 1.2 m. Quadrants of Fig. 4(b) highlight diffraction spots originating from different materials: the Aluminium (Al) and  $\text{SiO}_2$ .

Six rings are coloured in the top-right quadrant. These rings corresponding to  $hkl$ 's and  $2\theta$ 's in white in Fig. 5. Figure 4(c) illustrates the stress-strain curve and two tomography reconstructions during the experiment.

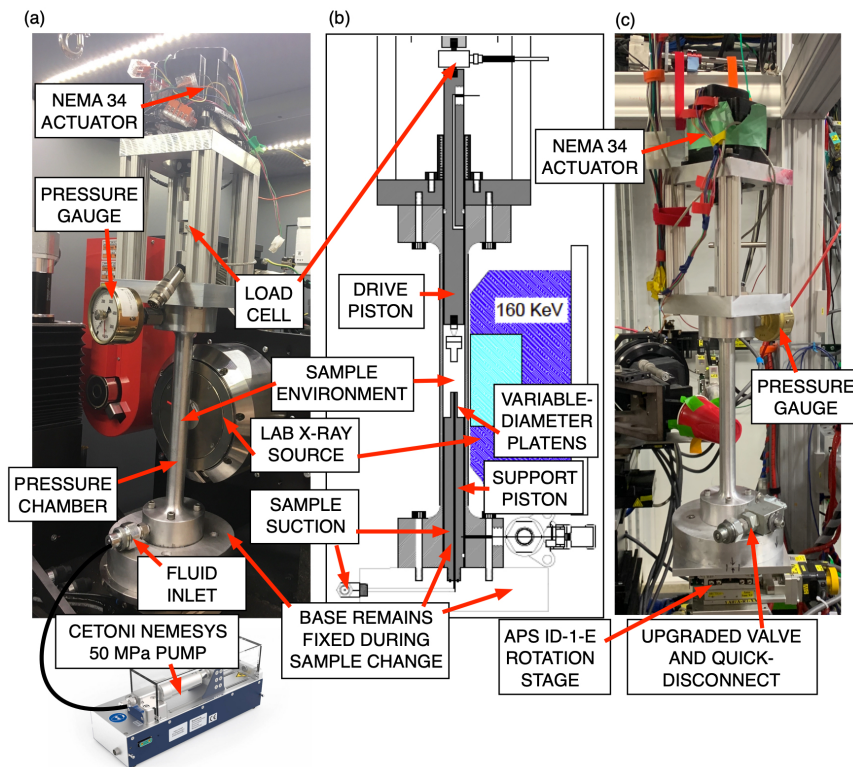


Figure 3: High Pressure TriAxial Compression Instrument (HP-TACO) at JHU used for studying geomaterials under confining pressures at up to 50 MPa in laboratory and at synchrotron x-ray sources. (a) Device in an RX Solutions MicroCT. (b) Cross-section of the device showing internal components. (c) Device at the APS ID1 beam-time.

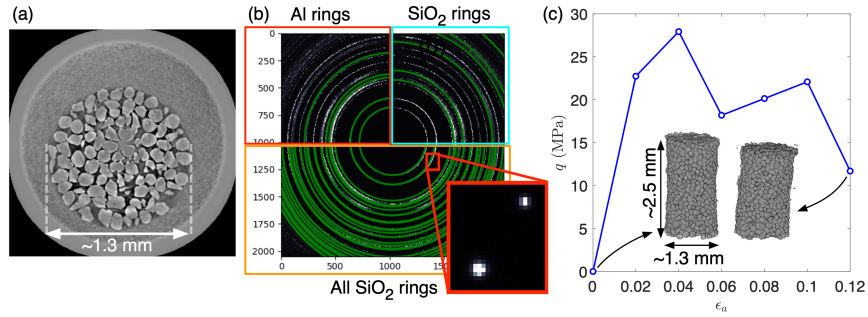
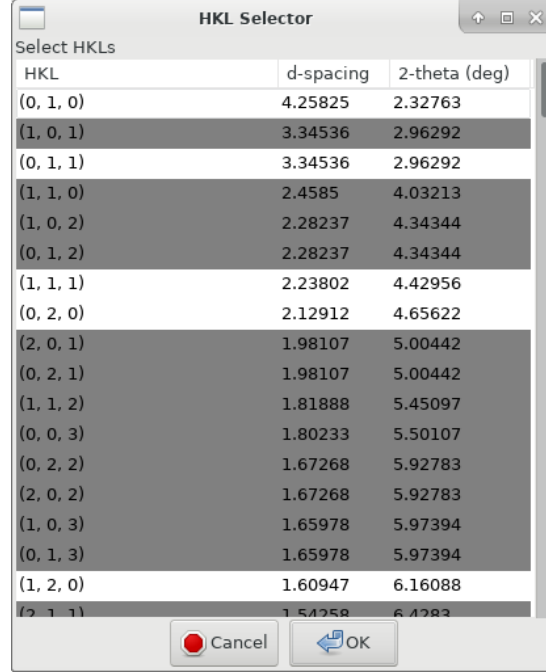


Figure 4: Experimental data from APS ID1. (a) Horizontal slice through XRCT image of a sample of quartz subjected to 30 MPa. (b) Maximum over all 3,600 diffraction patterns obtained during a single scan with quadrants overlaid with green lines indicating expected position of spots from known x-ray energy and sample-to-detector distance. Inset shows individual spots on a single frame. (c) Deviatoric stress- axial strain curve in experiment with insets showing XRCT reconstructions at two strain states during the experiment.



The screenshot shows a window titled "HKL Selector" with a table of crystallographic data. The table has three columns: "HKL", "d-spacing", and "2-theta (deg)". The rows list various Miller indices and their corresponding d-spacing and 2-theta values. The table is scrollable, and the bottom of the window has "Cancel" and "OK" buttons.

HKL	d-spacing	2-theta (deg)
(0, 1, 0)	4.25825	2.32763
(1, 0, 1)	3.34536	2.96292
(0, 1, 1)	3.34536	2.96292
(1, 1, 0)	2.4585	4.03213
(1, 0, 2)	2.28237	4.34344
(0, 1, 2)	2.28237	4.34344
(1, 1, 1)	2.23802	4.42956
(0, 2, 0)	2.12912	4.65622
(2, 0, 1)	1.98107	5.00442
(0, 2, 1)	1.98107	5.00442
(1, 1, 2)	1.81888	5.45097
(0, 0, 3)	1.80233	5.50107
(0, 2, 2)	1.67268	5.92783
(2, 0, 2)	1.67268	5.92783
(1, 0, 3)	1.65978	5.97394
(0, 1, 3)	1.65978	5.97394
(1, 2, 0)	1.60947	6.16088
(2, 1, 1)	1.54258	6.4282

Figure 5: Miller indices, real-space crystal d-spacing (in Angstroms), and  $2\theta$  (calculated using Bragg's law and the known sample-to-detector distance described in the text).

### 3 3DXRD Analysis of Diffraction Patterns and Grain Stress Analysis

Here, we provide a brief example of 3DXRD data analysis applied to diffraction patterns obtained on a sample of concrete studied at the ESRF ID11. The goal of the analysis is to obtain crystal lattice parameters ( $a, b, c, \alpha, \beta, \gamma$ ), as well as the reciprocal lattice parameters, crystallographic orientations, and crystal positions for each single crystal in the sample from the distribution of Bragg peaks on the far-field diffraction detector. From the crystal lattice parameters, crystal strains in the crystal frame for each grain,  $\epsilon^{g,cf}$ , can be obtained from sequential 3DXRD analysis performed as the sample is strained by

$$\epsilon^{g,cf} = (\mathbf{A}\mathbf{A}_0^{-1} + (\mathbf{A}\mathbf{A}_0^{-1})^T) - \mathbf{I}, \quad (2)$$

where

$$\mathbf{A} = \begin{pmatrix} a & b \cos \gamma & c \cos \beta \\ 0 & b \sin \theta & -c \sin \beta \cos \alpha^* \\ 0 & 0 & c \sin \beta \sin \alpha^* \end{pmatrix}, \quad (3)$$

containing lattice parameters (and reciprocal parameters) at a given strain step and  $\mathbf{A}_0$  is the same matrix but with reference-state lattice parameters (ideally when the sample is not experiencing any strain). Once the strain is known in the crystal frame, the elastic stress of the crystal can be obtained in the crystal frame from Hooke's law using the anisotropic stiffness tensor of the crystal,  $\boldsymbol{\sigma}^{g,cf} = \mathbf{C} : \boldsymbol{\epsilon}^{g,cf}$ . The stress tensor of each crystal or grain can then be rotated to the laboratory frame using  $\boldsymbol{\sigma}^{g,lf} = \mathbf{U} \boldsymbol{\sigma}^{g,cf} \mathbf{U}^T$ , where  $\mathbf{U}$  is a transformation tensor from crystal to laboratory frame.

The procedure involves the following steps, demonstrated in Fig. 6 for a concrete sample with single crystal alpha-quartz inclusions (an average of 150  $\mu\text{m}$  in effective diameter) studied at the ESRF ID11. The concrete sample is shown in Fig. 7. The analysis is shown for the case when the sample is under 20 MPa vertical pressure and unconfined laterally. There are 743 grains found in the sample during this analysis.

1. Read 3,600 diffraction patterns from a 360° rotation of the sample at a specific strain state and compute the median image intensity over all images. The resulting median intensity image is shown in Fig. 6(a).
2. Subtract the median from all diffraction patterns.
3. Segment peaks from the median-subtracted image. An example image is shown in Fig. 6(b) and isolated segmented peaks are shown in Fig. 6(c).
4. Filter peaks across all 3,600 diffraction patterns, requiring a minimum of a certain number of pixels in the peak to pass the filter. A resulting image is shown in Fig. 6(d) (as peaks would appear on the diffraction detector after collapsing all rotation angles,  $\omega$ , onto a single image) and the same data is shown in Fig. 6(e) in  $x = 2\theta$  and  $y = \text{azimuth}$  space (collapsing all rotation angles onto a single image).
5. Index grains: find probable grain orientations based on a minimum number of spots per grain or “completeness” in the first two rings of interest.
6. Fit grains using all rings of interest and a minimum number of spots per grain or “completeness”. A resulting image of grain locations is shown in Fig. 6(f).
7. Using the resulting grain crystal parameters and orientations, compute the individual intra-grain stress tensors in the lab frame. A resulting distribution plot of vertical stress tensor components in the concrete sample,  $p(\sigma_{zz}^{g,lf})$ , is shown in Fig. 6(g).



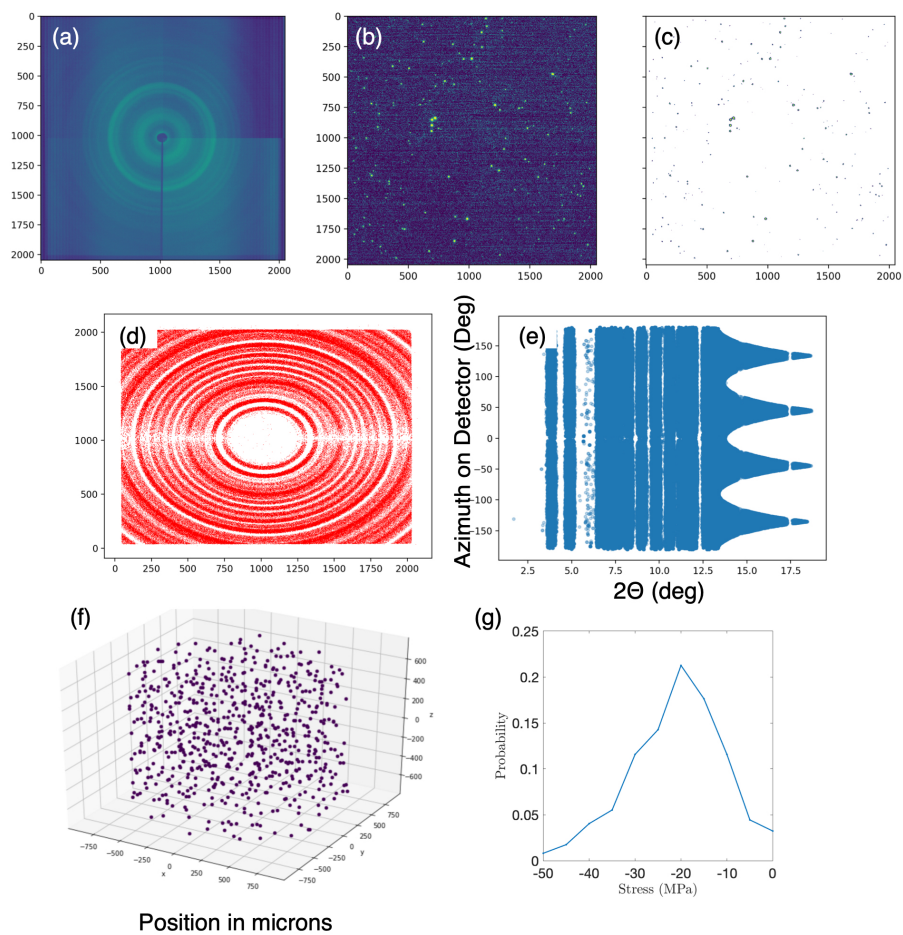


Figure 6: Process of diffraction analysis described in text. Note: if unlabelled, axes correspond to pixels on far-field diffraction detector. There are 2,048 x 2,048 pixels on the detector use in this example.

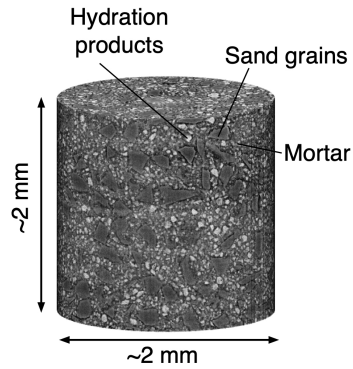


Figure 7: Concrete sample made by mixing Portland cement with single-crystal quartz aggregate (labelled as sand grains).

A collection of grain stress results from an experiment on 886 ruby spheres from [ZHHH19] and experiments on concrete cubes from [HP19] and unpublished work on another concrete cube are shown in Fig. 8 and 9, respectively.

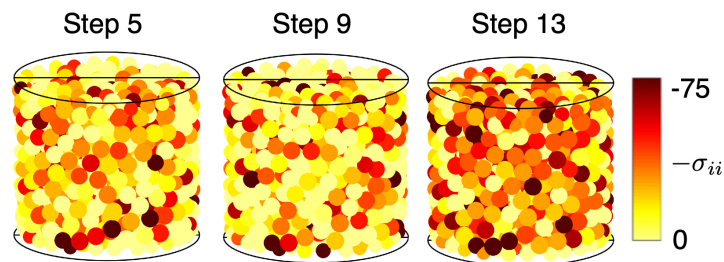


Figure 8: Stresses in ruby particles during uniaxial compression from [ZHHH19].

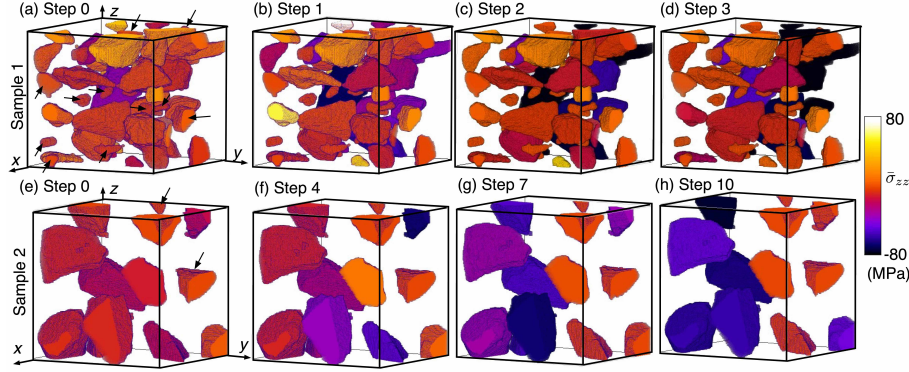


Figure 9: Stresses in sand grains within concrete specimens from [HP19] and unpublished work. Each specimen is about 1 mm x 1 mm x 1 mm. Only the sand grains are rendered; the mortar is not.

### 3.1 Inter-particle Force Inference in Granular Materials

After inter-particle contacts are known from analysis of fabric in XRCT images and intra-particle stress tensors are known from 3DXRD analysis described in the previous subsection, inter-particle force vectors can be inferred. We have described this force-inference procedure in several publications over the past 7 years [HMRA14, HLRA16, HHAW16]. Our most-recent version of the model is described here.

#### 3.1.1 Mathematical Procedure to Force Inference

The equations governing the mechanical equilibrium of a packing of particles include equilibrium equations and an equation relating the stresses to the inter-particle forces. In this subsection, we assemble these governing equations into two linear matrix equations for an entire granular packing, the first containing force and moment balance and the second containing stress-inter-particle force relations. The force inference procedure proposed in [HHAW16], and presented in slightly modified form here, simply involves selecting a set of inter-particle forces for a granular packing that minimizes the non-equality of these two matrix equations when terms within the equations are obtained through potentially inexact experimental measurements.

First, we consider the equilibrium, or force and moment balance, equations. Consider the  $p$ th particle in a granular material that interacts with a neighboring particle  $q$  at contact  $i$  and a boundary at contact  $j$ , as shown in Fig. 10. Force and moment balance of this particle can be written as [HHAW16, Hur21]

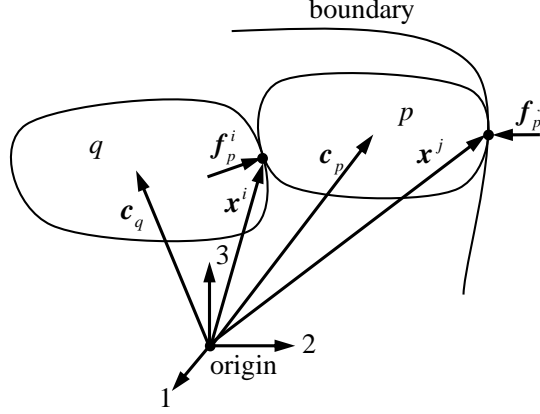


Figure 10: Illustration of particle  $p$  in contact with particle  $q$  at point  $i$  and with the boundary at point  $j$ .  $\mathbf{c}$  vectors denote centers-of-mass and  $\mathbf{f}$  vectors denote contact forces.

$$\sum_{\alpha=1}^{N_c^p} \kappa^p \mathbf{f}^\alpha = 0, \quad (4)$$

$$\sum_{\alpha=1}^{N_c^p} (\mathbf{x}^\alpha - \mathbf{c}^p) \times \mathbf{f}^\alpha = 0, \quad (5)$$

where  $\alpha$  are contact point labels ranging from 1 to  $N_c^p$  (the number of contacts for particle  $p$ ),  $\kappa^p$  is a weight factor of particle  $p$ ,  $\mathbf{f}^\alpha$  is the inter-particle force vector at contact  $\alpha$ ,  $\mathbf{x}^\alpha$  is a vector from the origin of a Cartesian coordinate system to contact  $\alpha$ , and  $\mathbf{c}^p$  is a vector from the origin to the center-of-mass of particle  $p$ . Equations 4 and 5 are simply a statement that particle  $p$  is in force and moment equilibrium under the action of all forces at  $N_c^p$  points on its boundary. In Eq. 4, the weight factor  $\kappa^p$  is a scalar that is intended to eliminate the unit difference between the force balance and moment balance equations.  $\kappa^p$  was absent in prior versions of the force inference technique [HMRA14, HHAW16, HLRA16]. The weight factor  $\kappa^p$  typically takes a value close to the particle radius. In contrast to prior force inference techniques in [HHAW16, Hur21], Eq. 5 also features  $\mathbf{c}^p$ , which makes each torque in the sum in this equation about the center of particle  $p$  rather than the origin of the coordinate system. The use of  $\mathbf{c}^p$  has the effect of making Eq. 5 independent of the origin of the coordinate system.

Equations 4 and 5 for *all particles* in a granular material can be combined in a linear matrix equation,

$$\mathbf{K}_{eq} \mathbf{f} = \mathbf{0}, \quad (6)$$

where  $\mathbf{0}$  is the zero vector,

$$\mathbf{f} = \begin{pmatrix} \vdots \\ \vdots \\ \mathbf{f}_p^i \\ \vdots \\ \vdots \\ \mathbf{f}_p^j \\ \vdots \\ \vdots \end{pmatrix}, \quad (7)$$

where  $\mathbf{f}_p^i = (f_1^i, f_2^i, f_3^i)^T$  is the force vector at contact  $i$  of particle  $p$ , where particle  $p$  contacts another particle  $q$ , and  $\mathbf{f}_p^j$  is the force vector at contact  $j$ , where particle  $p$  contacts a boundary. For the specific example shown in Fig. 10,  $\mathbf{K}_{eq}$  is given by

$$\mathbf{K}_{eq} = \begin{matrix} & i & & j & \\ \begin{matrix} p \\ q \end{matrix} & \begin{pmatrix} \ddots & \mathbf{0} & \dots & \mathbf{0} & \dots \\ \mathbf{0} & \mathbf{k}_{eq,p}^i & \mathbf{0} & \mathbf{k}_{eq,p}^j & \mathbf{0} \\ \vdots & \mathbf{0} & \ddots & \mathbf{0} & \vdots \\ \mathbf{0} & \mathbf{k}_{eq,q}^i & \mathbf{0} & \mathbf{0} & \mathbf{0} \\ \vdots & \mathbf{0} & \vdots & \mathbf{0} & \ddots \end{pmatrix} \end{matrix}. \quad (8)$$

In general, the matrix  $\mathbf{K}_{eq}$  has dimensions  $6N_p \times 3N_c$  in 3D ( $3N_p \times 2N_c$  in 2D), where  $N_c$  is the total number of contacts in a material and  $N_p$  is the total number of particles. The weights  $\kappa^p$  are captured in a sub-matrix, e.g.,  $\mathbf{k}_{eq,p}^i$ , to be defined below. The  $p$  and  $q$  row labels and  $i$  and  $j$  column labels in Eq. 8 are illustrative examples related to Fig. 10. These examples convey that a sub-matrix  $\mathbf{k}_{eq}$  appears only where a particle contacts another particle or boundary; otherwise, the corresponding entries in  $\mathbf{K}_{eq}$  are zero.

The vectors  $\mathbf{f}$  and  $\mathbf{0}$  in Eq. 6 each have dimensions  $3N_c \times 1$  in 3D ( $2N_c \times 1$  in 2D). Each sub-matrix within  $\mathbf{K}_{eq}$ , e.g.,  $\mathbf{k}_{eq,p}^i$ , is specific to a single particle. For particle  $p$  and contact  $i$ , this sub-matrix is written

$$\mathbf{k}_{eq,p}^i = \begin{bmatrix} \kappa^p & 0 & 0 \\ 0 & \kappa^p & 0 \\ 0 & 0 & \kappa^p \\ 0 & -(x_3^i - c_3^p) & (x_2^i - c_2^p) \\ (x_3^i - c_3^p) & 0 & -(x_1^i - c_1^p) \\ -(x_2^i - c_2^p) & (x_1^i - c_1^p) & 0 \end{bmatrix}. \quad (9)$$

Equation 6 can now be written as a statement of force and moment equilibrium for a granular packing with any number of particles and contacts.

We now consider the relationship between particle stresses and inter-particle forces. The volume-averaged stress within particle  $p$ ,  $\bar{\boldsymbol{\sigma}}^p$ , can be written using the linear mo-

mentum balance equation as

$$\bar{\sigma}^p = \frac{1}{V_p} \sum_{\alpha=1}^{N_c^p} (\mathbf{x}^\alpha - \mathbf{c}^p) \otimes \mathbf{f}^\alpha, \quad (10)$$

where  $V_p$  is the volume of the particle and the particle is assumed to be in static equilibrium. Equations 10 for *all particles* in a granular material can be combined in a linear matrix equation

$$\mathbf{K}_{st} \mathbf{f} = \mathbf{b}_{st}, \quad (11)$$

where  $\mathbf{b}_{st}$  is a  $6N_p \times 1$  column vector in 3D ( $3N_p$  in 2D) capturing the left-hand side of Eq. 10 multiplied by the particle volume and given by

$$\mathbf{b}_{st} = \begin{pmatrix} \vdots \\ \mathbf{b}^p \\ \vdots \\ \mathbf{b}^q \\ \vdots \end{pmatrix}, \text{ where } \mathbf{b}_p = \begin{pmatrix} V_p \bar{\sigma}_{11}^p \\ V_p \bar{\sigma}_{22}^p \\ V_p \bar{\sigma}_{33}^p \\ 2V_p \bar{\sigma}_{23}^p \\ 2V_p \bar{\sigma}_{13}^p \\ 2V_p \bar{\sigma}_{12}^p \end{pmatrix}. \quad (12)$$

In general, the matrix  $\mathbf{K}_{st}$  has dimensions  $6N_p \times 3N_c$  in 3D ( $3N_p \times 2N_c$  in 2D) and for the specific case shown in Fig. 10 is given by

$$\mathbf{K}_{st} = \begin{matrix} & i & & j & \\ \begin{matrix} p \\ q \end{matrix} & \begin{pmatrix} \ddots & \mathbf{0} & \dots & \mathbf{0} & \dots \\ \mathbf{0} & \mathbf{k}_{st,p}^i & \mathbf{0} & \mathbf{k}_{st,p}^j & \mathbf{0} \\ \vdots & \mathbf{0} & \ddots & \mathbf{0} & \vdots \\ \mathbf{0} & \mathbf{k}_{st,q}^i & \mathbf{0} & \mathbf{0} & \mathbf{0} \\ \vdots & \mathbf{0} & \vdots & \mathbf{0} & \ddots \end{pmatrix} \end{matrix}. \quad (13)$$

As with  $\mathbf{K}_{eq}$ , each sub-matrix within  $\mathbf{K}_{st}$  is specific to a single particle and contact in the granular packing. In  $\mathbf{K}_{st}$ , the sub-matrices, e.g.,  $\mathbf{k}_{st,p}^i$ , are given by

$$\mathbf{k}_{st,p}^i = \begin{bmatrix} x_1^i - c_1^p & 0 & 0 \\ 0 & x_2^i - c_2^p & 0 \\ 0 & 0 & x_3^i - c_3^p \\ x_2^i - c_2^p & x_1^i - c_1^p & 0 \\ x_3^i - c_3^p & 0 & x_1^i - c_1^p \\ 0 & x_3^i - c_3^p & x_2^i - c_2^p \end{bmatrix}. \quad (14)$$

Equation 11 can now be written to relate particle stresses to inter-particle forces for a granular packing with any number of particles and contacts.

As in prior work, the two matrix equations in Eq. 6 and 11 can be employed to infer forces throughout an entire granular packing. To do this, all terms in these equations except the inter-particle force vectors  $\mathbf{f}^\alpha$  must be measured. In practice, this is possible for crystalline grains using XRCT and 3DXRD in 3D [HHAW16] or for a variety of grain materials using imaging and DIC in 2D [HLRA16]. Once these measurements are made, forces can be inferred by

$$\mathbf{f} = \arg \min_{\mathbf{f}} (\lambda |\mathbf{K}_{eq} \mathbf{f}|_2 + |\mathbf{K}_{st} \mathbf{f} - \mathbf{b}_{st}|_2), \quad (15)$$

where  $|\cdots|_2$  is the 2-norm, and the minimization can be constrained to obey Eqs. 16 and 17. The term  $\lambda$  is a trade-off parameter that may be selected to be greater than, less than, or equal to unity, depending upon whether more, less, or equal weight, respectively, is given to the equilibrium equations in comparison to the stress-inter-particle force equations during minimization. Such weighting may be needed when weights within one set of equations can be measured with more accuracy than weights within the other set. In practice, we have found that a value of  $\lambda = 1$  typically provides a favorable minimization of errors.

Equation 15 seeks to obtain a set of forces throughout an entire granular packing,  $\mathbf{f}$ , that minimizes the non-equality of Eqs. 6 and 11. Such non-equality arises because experimental measurements may be inexact. The use of the 2-norm in our objective function is equivalent to the maximum likelihood estimate of a vector of values when Gaussian noise is present [BBV04]. That the noise or error in experimental measurements – for instance of particle stress tensor components – can be approximated by a Gaussian distribution has been demonstrated in several prior papers [HHP18, Hur21].

Two constraints – one imposing repulsive forces and one limiting inferred forces by a Coulomb friction criterion – have been imposed on the minimization in Eq. 15 in prior work [HHAW16]. These constraints can be written for any contact  $\alpha$  on particle  $p$  as

$$\mathbf{e}_p^\alpha \cdot \mathbf{f}_p^\alpha \geq 0 \quad (16)$$

$$\mu \mathbf{e}_p^\alpha \cdot \mathbf{f}_p^\alpha - \sqrt{(\mathbf{t}_{p1}^\alpha \cdot \mathbf{f}_p^\alpha)^2 + (\mathbf{t}_{p2}^\alpha \cdot \mathbf{f}_p^\alpha)^2} \geq 0, \quad (17)$$

where  $\mathbf{e}_p^\alpha$  is a normal vector to the contact plane at contact  $\alpha$  pointing toward the interior of particle  $p$ ,  $\mu$  is the Coulomb friction coefficient, and  $\mathbf{t}_{p1}^\alpha$  and  $\mathbf{t}_{p2}^\alpha$  are mutually orthogonal tangent vectors and lie in the contact plane and therefore define a basis for any point within the contact plane. The vectors  $\mathbf{t}_{p1}^\alpha$  and  $\mathbf{t}_{p2}^\alpha$  uniquely give the tangential force magnitude through the second term on the left-hand side of Eq. 17 so long as they form a basis for the contact plane. Equations 16 and 17 can be combined into a linear constraint equation that is a statement that forces are repulsive and do not exceed the Coulomb friction criterion. This linear constraint equation can be written

$$\mathbf{B} \mathbf{f} \geq \mathbf{0}. \quad (18)$$

## 4 Sample code

In practice, we execute the optimisation procedure with constraints in Matlab using CVX [GBY09]. A sample code block is shown next:

```
clear all; close all;
%% Force inference script, RCH August 2020
% Load data, make some arrays
load('D:\\LKM\\user\\LIGGGHTS\\force_inference_4\\
      ESRF2017uni\\step13\\results\\contacts3.mat');
savePath = 'D:\\LKM\\user\\LIGGGHTS\\
            force_inference_4\\ESRF2017uni\\step13\\results\\
            '
';
mu1 = 0.2;
mu2 = 0.2;
Rads = Data{19};
CenX = Data{4};
CenY = Data{5};
CenZ = Data{6};
Sxx = Data{20};
Syy = Data{21};
Szz = Data{22};
Sxy = Data{25};
Sxz = Data{24};
Syz = Data{23};

%% Initialize arrays
Nic = sum(contactMS(:,9)~=0); % Number of interior
    contacts (part.-part.)
Nec = size(contactMS,1) - Nic; % Number of exterior
    contacts (part.-bound)
Npt = size(Data{1},1);
Lamda=(-0.02216*(Nec+2*Nic)/Npt+1.20082)*Rads(1,1);

% Keq, Kst, bst
Keq = zeros(6*Npt,3*(Nic+Nec));
Kst = zeros(6*Npt,3*(Nic+Nec));
Bst = zeros(6*Npt,1);

% Initialize smaller matrices
keqc = zeros(6,3);
kstc = zeros(6,3);
bstg = zeros(6,1);
E = zeros(Nic+Nec,3*(Nic+Nec));
```



```

for ii=1:(Nic+Nec)
    T{ii} = zeros(2,3*(Nic+Nec));
    MuE{ii} = zeros(3*(Nic+Nec),1);
end
disp('Finished initialization of arrays');

% Loop over interior contacts
for ii=1:Nic
    % ID of contact
    M = contactMS(ii,8);
    S = contactMS(ii,9);

    % Build keqc, kstc
    % M master
    keqcM = [Lamda,0,0; 0,Lamda,0; 0,0,Lamda;
             0,-(contactMS(ii,3)-Particle(M,3)),
             contactMS(ii,2)-Particle(M,2);
             contactMS(ii,3)-Particle(M,3),0,
             -(contactMS(ii,1)-Particle(M,1));
             -(contactMS(ii,2)-Particle(M,2)),
             contactMS(ii,1)-Particle(M,1),0];
    kstcM = [contactMS(ii,1)-Particle(M,1),0,0; 0,
             contactMS(ii,2)-Particle(M,2),0; 0,0,contactMS(ii,
             3)-Particle(M,3);
             contactMS(ii,2)-Particle(M,2),
             contactMS(ii,1)-Particle(M,1),0; contactMS(ii,
             3)-Particle(M,3),0,
             contactMS(ii,1)-Particle(M,1);
             0,contactMS(ii,3)-Particle(M,3),
             contactMS(ii,2)-Particle(M,2)];

    % S master
    keqcS = [Lamda,0,0; 0,Lamda,0; 0,0,Lamda;
             0,-(contactMS(ii,3)-Particle(S,3)),
             contactMS(ii,2)-Particle(S,2);
             contactMS(ii,3)-Particle(S,3),0,
             -(contactMS(ii,1)-Particle(S,1));
             -(contactMS(ii,2)-Particle(S,2)),
             contactMS(ii,1)-Particle(S,1),0];
    kstcS = [contactMS(ii,1)-Particle(S,1),0,0; 0,
             contactMS(ii,2)-Particle(S,2),0; 0,0,contactMS(ii,
             3)-Particle(S,3);
             contactMS(ii,2)-Particle(S,2),

```

```

        contactMS(ii,1)-Particle(S,1),0; contactMS(
ii,3)-Particle(S,3),0,
        contactMS(ii,1)-Particle(S,1);
        0,contactMS(ii,3)-Particle(S,3),
        contactMS(ii,2)-Particle(S,2)];

% Insert into larger matrices
Keq(M*6-5:M*6,ii*3-2:ii*3) = keqcM;
Keq(S*6-5:S*6,ii*3-2:ii*3) = -keqcS;
Kst(M*6-5:M*6,ii*3-2:ii*3) = kstcM;
Kst(S*6-5:S*6,ii*3-2:ii*3) = -kstcS;

% Build E, T, MuE
E(ii,ii*3-2:ii*3) = contactMS(ii,10:12);
T{ii}(1,ii*3-2:ii*3) = contactMS(ii,13:15);
T{ii}(2,ii*3-2:ii*3) = contactMS(ii,16:18);
MuE{ii}(ii*3-2:ii*3,1) = mu1*contactMS(ii,10:12)
';
end

% Loop over exterior contacts (same but without S)
for ii=Nic+1:Nic+Nec
    % ID of grain
    M = contactMS(ii,8);

    % Build keqc, kstc
    % M master
    keqcM = [Lamda,0,0; 0,Lamda,0; 0,0,Lamda;
        0,-(contactMS(ii,3)-Particle(M,3)),
        contactMS(ii,2)-Particle(M,2);
        contactMS(ii,3)-Particle(M,3),0,-
        (contactMS(ii,1)-Particle(M,1));
        -(contactMS(ii,2)-Particle(M,2)),
        contactMS(ii,1)-Particle(M,1),0];
    kstcM = [contactMS(ii,1)-Particle(M,1),0,0; 0,
        contactMS(ii,2)-Particle(M,2),0; 0,0,contactMS(ii
        ,3)-Particle(M,3);
        contactMS(ii,2)-Particle(M,2),
        contactMS(ii,1)-Particle(M,1),0; contactMS(
ii,3)-Particle(M,3),0,
        contactMS(ii,1)-Particle(M,1);
        0,contactMS(ii,3)-Particle(M,3),
        contactMS(ii,2)-Particle(M,2)];

```

```

% Insert into larger matrices
Keq(M*6-5:M*6,ii*3-2:ii*3) = keqcM;
Kst(M*6-5:M*6,ii*3-2:ii*3) = kstcM;

% Build E, T, MuE
E(ii,ii*3-2:ii*3) = contactMS(ii,10:12);
T{ii}(1,ii*3-2:ii*3) = contactMS(ii,13:15);
T{ii}(2,ii*3-2:ii*3) = contactMS(ii,16:18);
MuE{ii}(ii*3-2:ii*3,1) = mu2*contactMS(ii,10:12)
';
end

% Add stresses
for ii=1:Npt
    % Build bstg
    indM = find(Data{1} == ii);
    % Get master and slave
    bstg = Rads(indM,1)^3*4/3*pi*[fStresses(ii,1),
    fStresses(ii,2),fStresses(ii,3),...
    2*fStresses(ii,6),2*fStresses(ii,5),2*
    fStresses(ii,4)]';
    Bst(ii*6-5:ii*6) = bstg;
end

% Report number of equations and unknowns
disp(['Number of equations: ',num2str(size(Kst,1)+
    size(Keq,1))]);
disp(['Number of unknowns: ',num2str(size(Kst,2))]);

Kt=[Keq;Kst];
Q=[zeros(size(Keq,1),1);Bst];
%% Do inference
lam = [1];
for jj=1: numel(lam)
    disp(['Beginning force inference...']);
    cvx_begin
    cvx_solver mosek
    variable forces(3*(Nic+Nec),1)
    minimize(norm(Kst*forces-Bst,2)+norm(Keq*forces
    ,2))
    subject to
    for ii=1:(Nic+Nec)
        E(ii,:)*forces>=0;
        norm(T{ii}*forces,2)<=MuE{ii}'*forces;
    end
end

```

```

end
cvx_end
% Save current set of forces
allforces{jj} = forces;
allnormKst(jj) = norm(Kst*forces-Bst,2);
allnormKeq(jj) = norm(Keq*forces,2);
end
%% force
for i=1:size(forces(:,1),1)/3
    contactMS(i,4)=forces(3*i-2);
    contactMS(i,5)=forces(3*i-1);
    contactMS(i,6)=forces(3*i);
    contactMS(i,7)=sqrt(contactMS(i,4)^2+
        contactMS(i,5)^2+contactMS(i,6)^2);
end

cd(savePath)
save('contacts_inf.mat','contactMS',
    'Data', 'fStresses', 'i', 'Particle');

```

If applied to the appropriate data in a .mat file, this code generates inter-particle force vectors at each inter-particle contact in a packing. As an example, we provide results from applying this script to data from an experiment performed at the ESRF ID11 involving uniaxial compression of 886 ruby particles described in [ZHHH19]. Figure 11(a) shows an XRCT scan of the sample at load step 1. Figure 11(b) shows a stress-load step curve, where stress is calculated as the homogenized, volume-averaged stress in the sample domain, as described in [ZHHH19]. Figure 11(c) shows the inter-particle force vectors inferred using the code in the code box above.

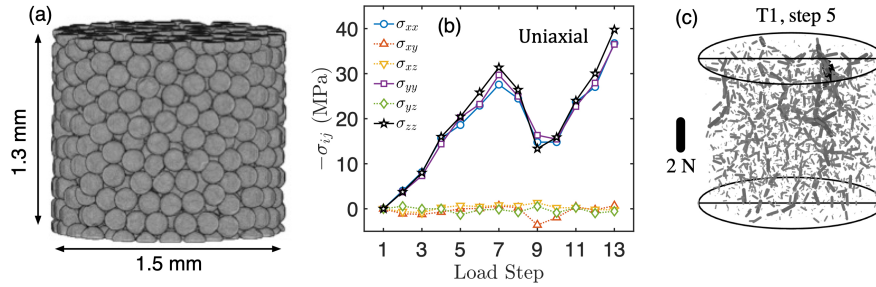


Figure 11: Uniaxial strain experiment performed on 886 ruby spheres. (a) XRCT reconstruction at load step 1. (b) Stress-load step curve (stresses volume-averaged in all grains), where stress is calculated as the homogenized, volume-averaged stress in the sample domain, as described in [ZHHH19]. (c) Inter-particle force vectors coloured as lines with on inter-particle contact points. Thickness and opacity scales linearly with force magnitude. All figures adapted from [ZHHH19].

## References

- [ACKL13] Khalid Alshibli, Mehmet B Cil, Peter Kenesei, and Ulrich Lienert. Strain tensor determination of compressed individual silica sand particles using high-energy synchrotron diffraction. *Granular matter*, 15(5):517–530, 2013.
- [BBLM11] Joel Vincent Bernier, Nathan Rhodes Barton, Ulrich Lienert, and Matthew Peter Miller. Far-field high-energy diffraction microscopy: a tool for intergranular orientation and strain analysis. *J. Strain Anal. Eng.*, 46(7):527–547, 2011.
- [BBV04] Stephen Boyd, Stephen P Boyd, and Lieven Vandenberghe. *Convex optimization*. Cambridge university press, 2004.
- [CAK17] Mehmet B Cil, Khalid A Alshibli, and Peter Kenesei. 3d experimental measurement of lattice strain and fracture behavior of sand particles using synchrotron x-ray diffraction and tomography. *Journal of Geotechnical and Geoenvironmental Engineering*, 143(9), 2017.
- [CAKL14] Mehmet B Cil, Khalid Alshibli, Peter Kenesei, and Ulrich Lienert. Combined high-energy synchrotron x-ray diffraction and computed tomography to characterize constitutive behavior of silica sand. *Nuclear Instruments and Methods in Physics Research Section B: Beam Interactions with Materials and Atoms*, 324:11–16, 2014.
- [GBY09] Michael Grant, Stephen Boyd, and Yinyu Ye. Cvx: Matlab software for disciplined convex programming, 2009.
- [HHAW16] RC Hurley, SA Hall, JE Andrade, and J Wright. Quantifying interparticle forces and heterogeneity in 3d granular materials. *Phys. Rev. Lett.*, 117(9):098005, 2016.
- [HHP18] Ryan C Hurley, Eric B Herbold, and Darren C Pagan. Characterization of the crystal structure, kinematics, stresses and rotations in angular granular quartz during compaction. *J. Appl. Crystallogr.*, 51(4):1021–1034, 2018.
- [HHW17] RC Hurley, SA Hall, and JP Wright. Multi-scale mechanics of granular solids from grain-resolved x-ray measurements. *Proc. R. Soc. A*, 473(2207):20170491, 2017.
- [HLP<sup>+</sup>17] RC Hurley, J Lind, DC Pagan, MA Homel, MC Akin, and EB Herbold. Linking initial microstructure and local response during quasistatic granular compaction. *Phys. Rev. E*, 96(1):012905, 2017.
- [HLP<sup>+</sup>18] RC Hurley, J Lind, DC Pagan, MC Akin, and EB Herbold. In situ grain fracture mechanics during uniaxial compaction of granular solids. *J. Mech. Phys. Solids*, 112:273–290, 2018.

- [HLRA16] RC Hurley, KW Lim, G Ravichandran, and JE Andrade. Dynamic inter-particle force inference in granular materials: method and application. *Exp. Mech.*, 56(2):217–229, 2016.
- [HMRA14] Ryan Hurley, Eloïse Marteau, Guruswami Ravichandran, and José E Andrade. Extracting inter-particle forces in opaque granular materials: beyond photoelasticity. *Journal of the Mechanics and Physics of Solids*, 63:154–166, 2014.
- [HP19] RC Hurley and DC Pagan. An in-situ study of stress evolution and fracture growth during compression of concrete. *International Journal of Solids and Structures*, 168:26–40, 2019.
- [Hur21] Ryan C Hurley. Stress and force measurement uncertainties in 3d granular materials. In *EPJ Web of Conferences*, volume 249, page 02009. EDP Sciences, 2021.
- [HW15] SA Hall and J Wright. Three-dimensional experimental granular mechanics. *Géotechnique Letters*, 5(4):236–242, 2015.
- [HWP<sup>+</sup>11] Stephen A Hall, Jonathan Wright, Thilo Pirling, Edward Andò, Darren J Hughes, and Gioacchino Viggiani. Can intergranular force transmission be identified in sand? *Granular Matter*, 13(3):251–254, 2011.
- [MAT<sup>+</sup>21] Amirsalar Moslehy, Khalid A Alshibli, Timothy J Truster, Peter Kenesei, Wadi H Imseeh, Zaher Jarrar, and Hemant Sharma. Evolution of texture and internal stresses within polycrystalline rock salt using in situ 3d synchrotron computed tomography and 3d x-ray diffraction. *Journal of Applied Crystallography*, 54(5), 2021.
- [OSP<sup>+</sup>10] Jette Oddershede, Søren Schmidt, Henning Friis Poulsen, Henning Osholm Sørensen, Jonathan Wright, and Walter Reimers. Determining grain resolved stresses in polycrystalline materials using three-dimensional x-ray diffraction. *Journal of Applied Crystallography*, 43(3):539–549, 2010.
- [PNL<sup>+</sup>01] Henning Friis Poulsen, Søren Fæster Nielsen, Erik M Lauridsen, Søren Schmidt, RM Suter, U Lienert, L Margulies, T Lorentzen, and D Juul Jensen. Three-dimensional maps of grain boundaries and the stress state of individual grains in polycrystals and powders. *Journal of applied crystallography*, 34(6):751–756, 2001.
- [Pou04] Henning Friis Poulsen. *Three-dimensional X-ray diffraction microscopy: mapping polycrystals and their dynamics*, volume 205. Springer Science & Business Media, 2004.
- [SAP<sup>+</sup>16] H Sharma, J Almer, JS Park, P Kenesei, M Wilde, and J Wozniak. Midas, microstructural imaging using diffraction analysis software. URL: <https://www1.aps.anl.gov/science/scientific-software/midas>, 2016.

- [SHHH22] Ghassan Shahin, Eric B Herbold, Stephen A Hall, and Ryan C Hurley. Quantifying the hierarchy of structural and mechanical length scales in granular systems. *Extreme Mechanics Letters*, 51:101590, 2022.
- [SHO12] Hemant Sharma, Richard M Huizenga, and S Erik Offerman. A fast methodology to determine the characteristics of thousands of grains using three-dimensional x-ray diffraction. i. overlapping diffraction peaks and parameters of the experimental setup. *Journal of applied crystallography*, 45(4):693–704, 2012.
- [Wri17] Jon Wright. ImageD11, 2017.
- [ZAE<sup>+</sup>22] Chongpu Zhai, Nahuel Albayrak, Jonas Engqvist, Stephen A Hall, Jonathan Wright, Marta Majkut, Eric B Herbold, and Ryan C Hurley. Quantifying local rearrangements in three-dimensional granular materials: Rearrangement measures, correlations, and relationship to stresses. *Physical Review E*, 105(1):014904, 2022.
- [ZHH20] Chongpu Zhai, Eric B Herbold, and Ryan C Hurley. The influence of packing structure and interparticle forces on ultrasound transmission in granular media. *Proceedings of the National Academy of Sciences*, 117(28):16234–16242, 2020.
- [ZHHH19] C Zhai, EB Herbold, SA Hall, and RC Hurley. Particle rotations and energy dissipation during mechanical compression of granular materials. *J. Mech. Phys. Solids*, 129:19–38, 2019.
- [ZPH20] C Zhai, DC Pagan, and RC Hurley. In situ x-ray tomography and 3d x-ray diffraction measurements of cemented granular materials. *JOM*, 72(1):18–27, 2020.



©ALERT Geomaterials  
Laboratoire 3SR / Bâtiment Galilée  
CS 40700  
38 058 Grenoble cedex 9  
France

**ISBN 978-2-9561359-9-9**

Fon: +33 (0) 456 528 621  
Fax: +33 (0) 476 827 043  
[president@alertgeomaterials.eu](mailto:president@alertgeomaterials.eu)  
<http://alertgeomaterials.eu>

---

All rights reserved. No part of this book may be reproduced in any form without written permission from the publisher or author.



# **ALERT Doctoral School 2022**

## *Advanced Experimental Geomechanics*

---

Editors: E. Andò, B. Marks, R. Hurley & J. A. Dijksmann

Andò, Marks & Hurley

Advanced Experimental Geomechanics

Marks

2D Image Analysis To Find Particles

Hurley

Photoelasticity: Stresses and Forces in 2D approaches

Andò

Introduction to 3D Imaging for Experimental Geomechanics

Dijksmann

Refractive Index Matched Scanning

Andò

3D imaging of opaque materials

Andò

3D Analysis

Hurley

Stress and Force Measurements in 3D

**ISBN 978-2-9561359-9-9**